Accelerating path integral evaluation of equilibrium and kinetic isotope effects

THÈSE N^{O} 8211 (2018)

PRÉSENTÉE LE 24 AVRIL 2018
À LA FACULTÉ DES SCIENCES DE BASE
LABORATOIRE DE CHIMIE PHYSIQUE THÉORIQUE
PROGRAMME DOCTORAL EN CHIMIE ET GÉNIE CHIMIQUE

ÉCOLE POLYTECHNIQUE FÉDÉRALE DE LAUSANNE

POUR L'OBTENTION DU GRADE DE DOCTEUR ÈS SCIENCES

PAR

Konstantin KARANDASHEV

acceptée sur proposition du jury:

Prof. L. Helm, président du jury
Prof. J. Vaníček, directeur de thèse
Prof. J. Richardson, rapporteur
Prof. O. A. von Lilienfeld, rapporteur
Prof. M. Ceriotti, rapporteur

ÉCOLE POLYTECHNIQUE
FÉDÉRALE DE LAUSANNE

Suisse
2018

Acknowledgements

There are a lot of people I would like to thank for this thesis. First of all, I would like to thank my advisor, Jiří, for giving me this very interesting project, and all the guidance on the science both related and unrelated to it.

I would also thank Eduardo, Miroslav, Tomáš, Marius, Alberto, and Aurelien, who were there when I was starting my PhD and were always ready to answer my multiple, and sometimes silly, questions. I am also thankful to my present colleagues Sergey, Julien, Tomislav, and Choi for interesting discussions and, in general, all the good time we had together.

My special thanks go to Sylvie, who has been great at handling administrative side of our work, and Daniel, who kept our computers running and was always ready to share advice on how to use them best.

I would also like to thank all the friends I met outside my lab throughout these years, as they helped a lot to make my stay in Lausanne such a memorable experience.

Last but not the least, I would like to thank my parents, who have always believed in me.

Lausanne, November 24, 2017 K. K.

Abstract

Investigating the effect of isotope substitution on equilibrium and kinetic properties of molecules has become an important tool for estimating the importance of nuclear quantum effects. In this work, we discuss calculating both equilibrium and kinetic isotope effects, i.e., the isotope effects on a system's partition function and a reaction's rate constant. With the help of Feynman's path integral formalism, both quantities can be estimated using standard Monte Carlo methods that scale favorably with system's dimensionality; improving efficiency of such approaches is the main focus of this work.

First of all, we developed a novel procedure for changing mass stochastically during an equilibrium isotope effect calculation, and evaluated the numerical benefits of combining it with two popular approaches for calculating isotope effects, using either direct estimators or thermodynamic integration. We demonstrate that the modification improves statistical convergence of both methods, and that it additionally allows to eliminate integration error of thermodynamic integration. The improved methods are tested on equilibrium isotope effects in a model harmonic system and in methane.

Then we turn our attention to kinetic isotope effect calculations with the quantum instanton approximation, a method whose path integral implementation belongs among the most accurate approaches for evaluating reaction rate constants in polyatomic systems. To accelerate quantum instanton calculations of kinetic isotope effects, we combine higher-order Boltzmann operator factorization with virial estimators, allowing us to speed up both the convergence to the quantum limit and statistical convergence of the calculation. We estimate the overall resulting acceleration using $\cdot\mathrm{H} + \mathrm{H}_2/\cdot\mathrm{D} + \mathrm{D}_2$ as a benchmark system, and then apply the accelerated method to several kinetic isotope effects associated with the $\cdot\mathrm{H} + \mathrm{CH}_4 \rightleftharpoons \mathrm{H}_2 + \cdot\mathrm{CH}_3$ exchange.

Last but not least, we explored ways to improve on the quantum instanton approximation for reaction rate constants. To that end, we review quantum instanton and Hansen-Andersen approximations, and propose a combined method, which, as the Hansen-Andersen approximation, has the correct high-temperature behavior, and at the same time, as the quantum instanton approximation, has more flexibility by allowing the dividing surface for the reaction to split into two surfaces at low temperatures. The properties of the combined method are tested on symmetric and asymmetric Eckart barrier.

Keywords: path integrals, isotope effects, chemical kinetics, quantum instanton, isotope fractionation, reaction rate constant, transition state theory, Monte Carlo, thermodynamic integration, free energy perturbation

Résumé

L'étude de l'effet de la substitution isotopique sur l'équilibre et les propriétés cinétiques des molécules est devenue un outil important pour estimer l'importance des effets quantiques nucléaires. Dans cette thèse, nous examinons les calculs des effets isotopique d'équilibre et cinétique, c'est-à-dire les effets isotopiques sur la fonction de partition d'un système et la constante de vitesse de réaction. Avec l'aide du formalisme intégral de chemin de Feynman, les deux quantités peuvent être estimées à l'aide de méthodes standard de Monte Carlo qui se dimensionnent favorablement à la dimensionnalité du système; l'objectif principal de cette thèse est d'améliorer l'efficacité de ces approches.

Tout d'abord, nous avons développé une nouvelle procédure pour changer les masses stochastiquement lors d'un calcul d'effet isotopique en équilibre et évalué les avantages numériques de la combiner avec deux approches populaires pour calculer les effets isotopiques, en utilisant soit des estimateurs directs, soit l'intégration thermodynamique. Nous démontrons que la modification améliore la convergence statistique des deux méthodes et qu'elle permet en outre d'éliminer l'erreur d'intégration de l'intégration thermodynamique. Les méthodes améliorées sont testées sur les effets isotopiques d'équilibre dans un système harmonique modèle et dans le méthane.

Ensuite, nous nous focalisons sur les calculs d'effets isotopiques cinétiques avec l'approximation de l'instanton quantique, une méthode dont l'implémentation intégrale de chemin est parmi les approches les plus précises pour évaluer les constantes de vitesse de réaction dans les systèmes polyatomiques. Pour accélérer les calculs quantiques quantitatifs d'effets isotopiques cinétiques, nous combinons la factorisation de l'opérateur de Boltzmann d'ordre supérieur avec des estimateurs viriels, ce qui nous permet d'accélérer à la fois la convergence vers la limite quantique et la convergence statistique du calcul. Nous estimons l'accélération globale résultante en utilisant $H + H_2/D + D_2$ comme système de référence, puis appliquons la méthode accélérée à plusieurs effets isotopiques cinétiques associés à l'échange $H + CH_4 \rightleftharpoons H_2 + CH_3$.

Enfin, nous explorons les moyens d'améliorer l'approximation de l'instanton quantique pour les constantes de vitesse de réaction. À cette fin, nous examinons les approximations de quantum instanton et Hansen-Andersen et proposons une méthode combinée qui, comme l'approximation de Hansen-Andersen, a le bon comportement à haute température, et en même temps, comme l'approximation de l'instanton quantique, a plus de flexibilité car il permet à la surface de séparation pour la réaction de se diviser en deux surfaces à basse température. Les propriétés de la méthode combinée sont testées sur barrière Eckart symétrique et asymétrique.

Mots-clés: intégrales du chemin, effets isotopiques, cinétique chimique, instanton quantique, fractionnement isotopique, constante de vitesse de réaction, théorie de l'état de transition, Monte Carlo, intégration thermodynamique, perturbation de l'énergie libre

Contents

Acknowledgements **iii**

Abstract **v**

Résumé **vii**

List of Figures **xiii**

List of Tables **xvii**

1 Introduction **1**

1.1 Equilibrium isotope effects and the Urey model 2
1.2 Reaction rate constant and classical transition state theory 4
1.3 Kinetic isotope effects 5
1.4 Overview of quantum and semiclassical methods of calculating rate constants 6
1.5 Feynman imaginary time path integral formalism 8
1.5.1 Basic path integral expressions 9
1.5.2 Using path integral formalism to calculate equilibrium properties . . 11
1.5.3 Path integral formalism and symmetrized correlation functions . . . 14
1.5.4 Details of numerical performance 15

2 Improving thermodynamic integration with respect to mass **17**

2.1 Introduction 17
2.2 Theory 19
2.2.1 Thermodynamic integration with respect to mass 19
2.2.2 Stochastic thermodynamic integration with respect to mass 20
2.3 Numerical examples 24
2.3.1 Computational details 24
2.3.2 Isotope effects in a harmonic model 25
2.3.3 Deuteration of methane 28
2.4 Conclusions 31

3 Improving equilibrium isotope effect calculations with direct estimators 35
3.1 Introduction . . . 35
3.2 Theory . . . 36
3.2.1 Free energy perturbation and direct estimators for equilibrium isotope effects . . . 36
3.2.2 Stepwise implementation of the direct estimators . . . 36
3.2.3 Combining direct estimators with the stochastic change of mass . . . 37
3.3 Numerical examples . . . 38
3.3.1 Computational details . . . 38
3.3.2 Isotope effects in a harmonic model . . . 39
3.3.3 Deuteration of methane . . . 40
3.4 Conclusion . . . 47

4 Combining virial estimators with higher-order Boltzmann operator splittings 49
4.1 Introduction . . . 49
4.2 Quantum instanton formalism . . . 50
4.3 General path integral implementation . . . 51
4.3.1 Estimators for constrained quantities . . . 51
4.3.2 Thermodynamic integration with respect to mass applied to the delta-delta correlation function . . . 53
4.3.3 Virial estimators . . . 55
4.4 Applications . . . 58
4.4.1 $\cdot\mathbf{H}+\mathbf{H_2}$ rearrangement . . . 59
4.4.2 $\mathbf{CH_4}+\cdot\mathbf{H}\rightleftharpoons\cdot\mathbf{CH_3}+\mathbf{H_2}$ exchange . . . 64
4.5 Conclusions . . . 69

5 Limitations of quantum instanton approximation 71
5.1 Introduction . . . 71
5.2 An alternative derivation of the quantum instanton approximation . . . 71
5.3 Drawbacks of quantum instanton formalism and possible corrections . . . 75
5.4 Hansen-Andersen formalism and its modified version . . . 76
5.5 Numerical tests . . . 77
5.5.1 Symmetric barrier performance . . . 78
5.5.2 Asymmetric barrier performance . . . 80
5.6 Conclusions . . . 81

6 Conclusions and outlook 83

A Mass-scaled normal modes of the ring polymer 85

B Dependence of the error of stochastic thermodynamic integration on the choice of umbrella biasing potential 87
B.1 Exact umbrella potential . . . 87
B.2 Piecewise constant umbrella potential . . . 88

B.3 Piecewise linear umbrella potential 89
B.4 Numerical tests 90

C Details of combining direct estimators with stochastic change of mass 93

D Estimate of the relative path integral discretization error 95

E Derivation of the fourth-order corrections for different estimators 99

F Derivation of $\mathbf{B}^{\mathbf{k}(\gamma)}$ 101

G Additional numerical results 103

H Connection of flux-flux and delta-delta correlation functions for the separable case 107

I Justification of using Hansen-Andersen ansatz for the flux-flux correlation function with split dividing surfaces 109
I.1 Imaginary time behavior of flux-flux correlation function 109
I.2 Hansen-Andersen ansatz and the split dividing surfaces' case 111

Bibliography 113

Curriculum Vitae 123

List of Figures

2.1 Temperature dependence of the relative error of the CD_4/CH_4 isotope effect (IE) obtained with the harmonic approximation (see Sec. 1.1). The result of stochastic thermodynamic integration (STI) serves as a reference; the relative error is defined as IE(harmonic)/IE(STI) - 1. 18

2.2 Isotope effect (IE) calculations in an eight-dimensional harmonic model from Subsec. 2.3.2. Unless explicitly stated in the label, all results use the centroid virial estimator (2.8) and improved mass interpolation (2.4). Results labeled “lin. interp.” use linear interpolation (2.3) and those labeled “th. est.” the thermodynamic estimator (2.7). Several versions of thermodynamic integration (TI) are compared with exact analytical values (for the same finite Trotter number P). The proposed method is “stochastic thermodynamics integration” (STI). Panels (a)-(c) show the temperature dependence of (a) the isotope effect, (b) its integration errors, and (c) its statistical root mean square errors (RMSEs). Panels (d)-(e) display the dependence of integration errors and RMSEs on the number J of integration subintervals at a temperature given by $\beta\hbar\omega_0 = 8$. 27

2.3 Calculations of the CD_4/CH_4 isotope effect (IE) from Subsec. 2.3.3. Labels are explained in the caption of Fig. 2.2. The three panels show the temperature dependence of (a) the isotope effect, (b) its integration errors, and (c) its statistical root mean square errors (RMSEs). 30

2.4 The impact of nonergodicity appearing in shorter calculations of the CD_4/CH_4 isotope effect (IE) at $T = 200$ K. Panel (a) presents the convergence of the IE as a function of the simulation length, while panel (b) shows the corresponding error of the IE (in logarithmic scale) relative to a converged STI result. Labels TI and STI are as in the caption of Fig. 2.2; “STI (no simple λ-moves)” were obtained without the simple λ-moves defined by Eqs. (2.12)-(2.16), while “STI (no mass-scaled λ-moves)” were obtained without mass-scaled λ-moves defined by Eqs. (2.17)-(2.20). The horizontal line in panel (a) labeled “STI (converged)” is the converged STI result $\ln(\mathrm{IE}_{\mathrm{STI}}) = 19.789$ from Fig. 2.3 and Table 2.1; the same value was used as a reference in panel (b). 32

3.1 Isotope effect (IE) calculations in an eight-dimensional harmonic model from Subsec. 3.3.2. Thermodynamic integration (TI), stochastic thermodynamic integration (STI), stepwise direct estimators (DE), stochastic direct estimators (SDE), and original direct estimator approach from Ref. [1] are compared with exact analytical values (for the same finite Trotter number P). The proposed method is “stochastic direct estimators” (SDE), “direct estimators” (DE) has not been used before either. Panels (a)-(c) show the temperature dependence of (a) the isotope effect, (b) its integration errors, and (c) its statistical root mean square errors (RMSEs). Panels (d)-(e) display the dependence of integration errors and RMSEs on the number J of integration subintervals at a temperature given by $\beta\hbar\omega_0 = 8$. 41

3.2 Calculations of the CD_4/CH_4 isotope effect (IE) from Subsec. 3.3.3. Labels are explained in the caption of Fig. 3.1. The three panels show the temperature dependence of (a) the isotope effect, (b) its integration errors, and (c) its statistical root mean square errors (RMSEs). For integration errors SDE values were used as the reference. 43

3.3 The impact of nonergodicity appearing in shorter calculations of the CD_4/CH_4 isotope effect (IE) at $T = 200$ K. Panel (a) presents the convergence of the IE as a function of the simulation length, while panel (b) shows the corresponding error of the IE (in logarithmic scale) relative to a converged STI result. Labels TI, STI and SDE are as in the caption of Fig. 3.1; “STI (no simple λ-moves)” and “SDE (no simple λ-moves)”were obtained without the simple λ-moves proposed in Ref. [2]; while “SDE (no mass-scaled λ-moves)” were obtained without mass-scaled λ-moves proposed in Ref. [2]. The horizontal line in panel (a) labeled “SDE (converged)” is the converged SDE result $\ln(\mathrm{IE}_{\mathrm{SDE}}) = 19.788$ from Fig. 3.2 and Table 3.1; the same value was used as a reference in panel (b). 46

4.1 Convergence of various quantities required in the quantum instanton approximation of the kinetic isotope effect to the quantum limit as a function of the Trotter number P: (a) $d\ln Q_r/d\lambda$, (b) $\partial \ln C_{\mathrm{dd}}/\partial\lambda$, (c) ΔH^2, (d) $C_{\mathrm{ff}}/C_{\mathrm{dd}}$, (e) $\partial \ln C_{\mathrm{dd}}/\partial\eta_a^{\ddagger}$. Results shown were obtained with the virial estimators and correspond to the kinetic isotope effect $\cdot\mathrm{H}+\mathrm{H}_2/\cdot\mathrm{D}+\mathrm{D}_2$ at 200 K. 61

4.2 Statistical root mean square errors (RMSE) obtained with different estimators at different values of the Trotter number P for quantities required in the quantum instanton approximation. (a) $d\ln Q_r/d\lambda$, (b) $\partial \ln C_{\mathrm{dd}}/\partial\lambda$, (c) ΔH^2, (d) $C_{\mathrm{ff}}/C_{\mathrm{dd}}$, (e) $\partial \ln C_{\mathrm{dd}}/\partial\eta_a^{\ddagger}$. Results correspond to the kinetic isotope effect $\cdot\mathrm{H}+\mathrm{H}_2/\cdot\mathrm{D}+\mathrm{D}_2$ at 200 K. “v” stands for “virial”, “th” - for “thermodynamic”. 61

5.1 Errors of symmetric Eckart barrier ($\alpha_1 = \alpha_2 = 12$) reaction rates, denoted $k_{\mathrm{calc.}}$, calculated with quantum instanton approximation [3], as well as Hansen-Andersen transition state theory [4, 5] and its modified version proposed in this work. The exact rate k_{QM} was obtained from Eq. (5.31). . 79

5.2 Errors of asymmetric Eckart barrier ($\alpha_1 = 12$, $\alpha_2 = 48$) reaction rates, denoted $k_{\mathrm{calc.}}$, calculated with quantum instanton approximation [3], as well as Hansen-Andersen transition state theory [4, 5] and its modified version proposed in this work. The exact rate k_{QM} was obtained from Eq. (5.31). . 81

B.1 Impact of the umbrella biasing potential on the numerical errors of a simulation. The figure shows the dependence of integration errors [(a) with linear, (b) with logarithmic scale] and statistical errors [panel (c)] on the number J of λ intervals used in the standard thermodynamic integration (TI) and stochastic thermodynamic integration (STI) employing various types of umbrella potentials mentioned in parentheses: “piecewise constant” uses an umbrella potential (B.4) constant over each of the J intervals, “piecewise linear” potential is given by Eqs. (2.24) or (B.16), and “exact” corresponds to the unrealistic situation when one knows the exact, ideal umbrella potential (B.2). 91

D.1 Comparison of exact analytical values of the path integral discretization error of (a) the partition function Q and (b) isotope effect with their estimates [Eqs. (D.2) and (D.8)], which were evaluated either analytically or numerically using the estimator (D.6). The figure shows the dependence of the discretization error on the Trotter number P in a one-dimensional harmonic oscillator with $\beta\hbar\omega = 8$, and the isotope effect corresponds to the doubling of the mass. 98

G.1 Absolute discretization error (DE) of different quantities as a function of P: (a) $d\ln Q_r/d\lambda$, (b) $\partial \ln C_{\mathrm{dd}}/\partial\lambda$, (c) ΔH^2, (d) $C_{\mathrm{ff}}/C_{\mathrm{dd}}$, (e) $\partial \ln C_{\mathrm{dd}}/\partial\eta_a^{\ddagger}$. Results shown were obtained with the virial estimators and correspond to the kinetic isotope effect $\cdot\mathrm{H}+\mathrm{H}_2/\cdot\mathrm{D}+\mathrm{D}_2$ at 200 K. 104

List of Tables

1.1 Summary of the notation used in this work for a system of N particles in a D-dimensional Euclidean space. m_i is the mass of particle i; $\mathbf{v}$ and $\mathbf{w}$ are vectors defined in the DN-dimensional configuration space, while v_i and w_i are their D-dimensional components corresponding to particle i; $\mathbf{A}$ is a Hermitian matrix defined over the configuration space, and A_{ij} is its $D \times D$ dimensional submatrix containing only the columns corresponding to particle i and rows corresponding to particle j. 2

1.2 Dependence of weights $\tilde{w}_s$ on the bead number s and Boltzmann factorization. 11

2.1 Values of the CD_4/CH_4 isotope effect (IE) obtained with several versions of thermodynamic integration (TI). Corresponding statistical errors are shown as well. Unless explicitly stated in the label, all results use the centroid virial estimator (2.8) and improved mass interpolation (2.4). The proposed methodology is stochastic thermodynamic integration (STI). 29

3.1 Values of the CD_4/CH_4 isotope effect (IE) obtained with thermodynamic integration (TI), stochastic thermodynamic integration (STI), direct estimators (DE), and “stochastic direct estimators” (SDE). Corresponding statistical errors are shown as well. The proposed methodology is SDE. The discretization error is defined as $(\mathrm{IE}_P/\mathrm{IE} - 1)$ and is estimated with the procedure described in Appendix D. 44

3.2 Temperature dependence of the $CH_{4-x}D_x/CH_4$ isotope effect for x = 1, 2, 3. The results were obtained with “stochastic direct estimators”. 45

4.1 Estimated speedups of the quantum instanton calculations achieved by the use of various combinations of path integral factorizations and estimators (th = thermodynamic, v = virial). Speedup “1” (i.e., no speedup) corresponds to the standard method employing a combination of the Lie-Trotter factorization and thermodynamic estimators. Results correspond to the kinetic isotope effect (KIE) $\cdot\mathrm{H} + \mathrm{H}_2/\cdot\mathrm{D} + \mathrm{D}_2$ at 200 K. 63

4.2 Kinetic isotope effect $\cdot\mathrm{H}+\mathrm{H}_2/\cdot\mathrm{D}+\mathrm{D}_2$ at different temperatures. "QI" stands for "quantum instanton." 64
4.3 Kinetic isotope effect $\mathrm{CH}_4+\cdot\mathrm{H}/\mathrm{CH}_4+\cdot\mathrm{D}$. 66
4.4 Kinetic isotope effect $\cdot\mathrm{CH}_3+\mathrm{D}_2/\cdot\mathrm{CD}_3+\mathrm{D}_2$. 66
4.5 Kinetic isotope effect $\cdot\mathrm{CH}_3+\mathrm{H}_2/\cdot\mathrm{CD}_3+\mathrm{H}_2$. 66
4.6 Kinetic isotope effect $\cdot\mathrm{CH}_3+\mathrm{HD}/\cdot\mathrm{CH}_3+\mathrm{DH}$. 66
4.7 Kinetic isotope effect $\cdot\mathrm{CD}_3+\mathrm{HD}/\cdot\mathrm{CD}_3+\mathrm{DH}$. 67
4.8 Kinetic isotope effect $\cdot\mathrm{CD}_3+\mathrm{H}_2/\cdot\mathrm{CD}_3+\mathrm{D}_2$. 67
4.9 Kinetic isotope effect $\cdot\mathrm{CH}_3+\mathrm{H}_2/\cdot\mathrm{CH}_3+\mathrm{D}_2$. 67
4.10 Influence of the potential energy surface (PES) on the kinetic isotope effect $\mathrm{CH}_4+\cdot\mathrm{H}/\mathrm{CH}_4+\cdot\mathrm{D}$. Comparison of the quantum instanton (QI) kinetic isotope effects calculated using the PES's of Refs. [6] and [7]. Note also the remarkable agreement between the kinetic isotope effects computed with ring polymer molecular dynamics (RPMD) and QI on the same PES. 69

5.1 Tunneling correction values [Eq. (5.27)] obtained for the symmetric Eckart barrier ($\alpha_1=\alpha_2=12$). "SCI" stands for "semiclassical instanton." 80
5.2 Tunneling correction values [Eq. (5.27)] obtained for the asymmetric Eckart barrier ($\alpha_1=12$, $\alpha_2=48$). 81

G.1 Values of the factors entering the quantum instanton expression (4.26) for the kinetic isotope effect $\cdot\mathrm{H}+\mathrm{H}_2/\cdot\mathrm{D}+\mathrm{D}_2$ with optimized dividing surfaces' positions, displayed in Table 4.2. All quantities as well as their statistical errors are in atomic units. 104
G.2 Optimal positions of the dividing surfaces along the reaction coordinate [see Eq. (4.51)] for transition states of several isotopic variants of the $\mathrm{CH}_4+\cdot\mathrm{H}\rightleftharpoons\cdot\mathrm{CH}_3+\mathrm{H}_2$ exchange at several temperatures. 105

1 Introduction

Influence of nuclear quantum effects on molecular properties has been observed since as early as the nineteenth century, when the equipartition theorem was found to be violated in a number of substances; the phenomenon could only be explained in the beginning of twentieth century using the notion of vibrational energy quantization and played an important role in the formulation of quantum mechanics [8]. An important experimental tool for studying nuclear quantum effects is isotope substitution [9], i.e., changing masses of some atoms in the molecular system without changing its chemical composition. In the framework of classical mechanics such a change does not affect the equilibrium constant, while reaction rate constants are only changed by a small factor which rarely exceeds square root of two. In the quantum picture, however, both quantities can change quite drastically, and the resulting deviation from the classical picture can tell a lot about quantum effects in the system. Developing computationally cheap methods for accurately predicting equilibrium and kinetic isotope effects, i.e., the effects of mass change on equilibrium and rate constants, is therefore the main focus of this work.

Calculating exact quantum equilibrium properties can be done up to an arbitrary accuracy using Monte Carlo or molecular dynamics methods combined with the Feynman imaginary-time path integral formalism [10, 11]; while the basics of the approach will be outlined in Sec. 1.5, its application to equilibrium isotope effects will be discussed thoroughly in Chapters 2 and 3. Calculating kinetic isotope effects is much more involved, as exact evaluation of a rate constant is a daunting task for higher-dimensional systems, as will be discussed in Sec. 1.4. In this work we considered quantum instanton approximation to the rate constant [3], whose path integral implementation allows to use Monte Carlo or molecular dynamics for the calculations [12]; applying the approach to kinetic isotope effects is discussed in Chapter 4. Finally, we investigated whether it is possible to improve accuracy of the quantum instanton approximation itself in Chapter 5. Some of the more special notation used throughout the work is summarized in Table 1.1.

Table 1.1: Summary of the notation used in this work for a system of N particles in a D-dimensional Euclidean space. m_i is the mass of particle i; $\mathbf{v}$ and $\mathbf{w}$ are vectors defined in the DN-dimensional configuration space, while v_i and w_i are their D-dimensional components corresponding to particle i; $\mathbf{A}$ is a Hermitian matrix defined over the configuration space, and A_{ij} is its $D \times D$ dimensional submatrix containing only the columns corresponding to particle i and rows corresponding to particle j.

Expression	Comment
∇_i	gradient with respect to coordinates of particle i
$\mathrm{v}_i \cdot \mathrm{w}_i := \sum_{j=1}^{D} \mathrm{v}_{i,j} \cdot \mathrm{w}_{i,j}$	standard dot product of v_i and w_i in the D-dimensional Euclidean space
$\langle \mathbf{v}, \mathbf{w} \rangle_s := \sum_{i=1}^{N} (m_i)^s \mathrm{v}_i \cdot \mathrm{w}_i$	mass-weighted inner product of $\mathbf{v}$ and $\mathbf{w}$ in the system's configuration space, where $s \in \{-1,\ 0,\ 1\}$ on the right-hand side, while on the left-hand side a corresponding shorthand notation $s \in \{-,\ 0,\ +\}$ is used
$\|\|\mathbf{v}\|\|_s := \sqrt{\langle \mathbf{v}, \mathbf{v} \rangle_s}$	mass-weighted norm of a configuration space vector
$\langle \mathbf{v}, \mathbf{A}, \mathbf{w} \rangle_{su} := \sum_{i=1}^{N} \sum_{j=1}^{N} m_i^s m_j^u \mathrm{v}_i \cdot \mathrm{A}_{ij} \cdot \mathrm{w}_j$	matrix product of $\mathbf{A}$ with $\mathbf{v}$ and $\mathbf{w}$; the same shorthand notation is used for s and u as in $\langle \mathbf{v}, \mathbf{w} \rangle_s$

1.1 Equilibrium isotope effects and the Urey model

The equilibrium (or thermodynamic) isotope effect [9] is defined as the effect of isotopic substitution on the equilibrium constant of a chemical reaction. More precisely, the equilibrium isotope effect is the ratio of equilibrium constants,

$$\mathrm{EIE} := \frac{K^{(B)}}{K^{(A)}}, \tag{1.1}$$

where A and B are two isotopologues of the reactive system. Since an equilibrium constant can be evaluated as the ratio of the product and reactant partition functions ($K = Q_{\mathrm{prod}}/Q_{\mathrm{react}}$), every equilibrium isotope effect can be written as a product of several "elementary" isotope effects (IEs),

$$\mathrm{IE} := \frac{Q^{(B)}}{Q^{(A)}}, \tag{1.2}$$

given by the ratio of partition functions corresponding to different isotopologues (of either the reactant or product).

This quantity is closely related to the important notion of *isotope fractionation* [9, 13], which describes the distribution of isotopes in different substances or different phases. While a large number of fractionation ratios observed in nature are caused, at least partially, by kinetic factors [9], purely thermodynamic equilibrium isotope effects can also be interesting tools, for example, for determining how a hydrogen atom is bound within a metal complex [14] or an enzyme system [15].

The classical estimate for an equilibrium isotope effect can be obtained from the classical partition function Q_{cl}

$$Q_{\mathrm{cl}} = \frac{\left(\prod_{i=1}^{N} m_i\right)^{D/2}}{\sigma(2\pi\beta\hbar^2)^{DN/2}} \int \exp[-\beta V(\mathbf{r})]d\mathbf{r}, \tag{1.3}$$

where $\beta := (k_{\mathrm{B}}T)^{-1}$, k_{B} is the Boltzmann constant, T the thermodynamic temperature, $\hbar$ the reduced Planck constant, σ the symmetry factor, N the number of atoms, m_i are masses of atom i ($i \in \{1, \ldots, N\}$), D the number of dimensions in Cartesian space (obviously $D = 3$ for practical applications), $\mathbf{r}$ a vector in the system's configuration space and $V(\mathbf{r})$ the system's potential. The resulting classical equilibrium isotope effect estimate reads

$$\mathrm{IE}_{\mathrm{cl}} = \frac{\sigma^{(A)}}{\sigma^{(B)}} \left(\prod_{i=1}^{N} \frac{m_i^{(B)}}{m_i^{(A)}} \right)^{D/2} \tag{1.4}$$

and is valid for arbitrary potential energy $V(\mathbf{r})$. The simplest and most common *quantum* approach to evaluate Eq. (1.2), usually referred to as the "harmonic approximation" or "Urey model," assumes (i) separability of rotations and vibrations, (ii) rigid rotor approximation for the rotations, and (iii) harmonic oscillator approximation for the vibrations [9, 13, 16]. Within this approximation, the partition function can be written as the product

$$Q_{\mathrm{HA}} = Q_{\mathrm{trans}} Q_{\mathrm{rot}} Q_{\mathrm{vib}}, \tag{1.5}$$

where Q_{trans}, Q_{rot} and Q_{vib} are translational, rotational and vibrational partition functions. If both the rotations and vibrations are treated classically then applying Teller–Redlich product rule [17, 18] results in an expression identical to Eq. (1.4), even though Eq. (1.4) cannot be applied directly to this problem as it takes into account rovibrational coupling, which we neglect. To treat vibrations quantum mechanically, one "corrects" the factor in Q_{HA} for each harmonic vibrational degree of freedom by multiplying it with the ratio $Q_{\mathrm{qSHO}}/Q_{\mathrm{cSHO}}$ of quantum and classical partition functions of a simple harmonic oscillator with frequency ω:

$$\begin{aligned} Q_{\mathrm{qSHO}} &= \frac{1}{2\sinh(\beta\hbar\omega/2)}, \\ Q_{\mathrm{cSHO}} &= \frac{1}{\beta\hbar\omega}, \\ \frac{Q_{\mathrm{qSHO}}}{Q_{\mathrm{cSHO}}} &= \frac{\beta\hbar\omega}{2\sinh(\beta\hbar\omega/2)}. \end{aligned}$$

Inserting such corrections for each vibrational degree of freedom in the partition functions for both isotopologues replaces Eq. (1.4) with the "harmonic approximation" expression

$$\mathrm{IE}_{\mathrm{HA}} = \frac{\sigma^{(A)}}{\sigma^{(B)}} \left(\prod_{i=1}^{N} \frac{m_i^{(B)}}{m_i^{(A)}} \right)^{D/2} \prod_{q=1}^{N_q} \frac{\omega_q^{(B)} \sinh(\beta\hbar\omega_q^{(A)}/2)}{\omega^{(A)} \sinh(\beta\hbar\omega_q^{(B)}/2)}, \tag{1.6}$$

where N_q is the number of vibrational degrees of freedom, and $\omega_q^{(A)}$ and $\omega_q^{(B)}$ ($q \in \{1, \ldots, N_q\}$) are vibrational frequencies. It is clear that this expression allows to account, at least partially, for zero-point energy effects in the system; it can also be further improved with various corrections that incorporate the leading effects of rovibrational coupling, nonrigidity of the rotor, or anharmonicity of the vibrations [19–21]. However, such a perturbative approach is not always sufficient; indeed, there are examples of systems in which these corrections can even yield worse results than the Urey model [16]. Using Feynman path integral approach allows to treat the problem exactly, as will be discussed properly in Sec. 1.5.

1.2 Reaction rate constant and classical transition state theory

Reaction rate constant is a quantity central to chemical kinetics, and its accurate evaluation is probably one of the most important goals of theoretical chemistry. To obtain a classical value of the quantity, one starts by defining a reaction coordinate $\xi(\mathbf{r})$ such that $\xi(\mathbf{r}) = 0$ sets a dividing surface separating configuration space into reactant $[\xi(\mathbf{r}) < 0]$ and product $[\xi(\mathbf{r}) > 0]$ regions. Classical transition state theory is based on two assumptions, which will often resurface during discussions of other methods for calculating reaction rates. First of all, one assumes that thermal distribution between the reactant region and the dividing surface, or “transition state,” remains roughly unperturbed during the reaction. Secondly, one assumes that there is no recrossing over the dividing surface, that is each time the system crosses through the transition state into the product region it stays there indefinitely. These approximations lead to the classical transition state theory reaction rate k_{cTST} being proportional to the probability of finding the system at the dividing surface with the momentum pointed towards the product region. Substituting the classical Boltzmann probability density and analytically evaluating the integral over momentum leads to the final expression [22, 23]

$$\begin{aligned} k_{\mathrm{cTST}} &= \frac{1}{\sqrt{2\pi\beta}} \frac{\langle \Delta(\mathbf{r}) \rangle_{\mathrm{cl}}}{\langle \{1 - h[\xi(\mathbf{r})]\} \rangle_{\mathrm{cl}}} \\ &= \frac{1}{\sqrt{2\pi\beta}} \frac{\langle \Delta(\mathbf{r}) \rangle_{\mathrm{cl}}}{Q_r}, \end{aligned} \tag{1.7}$$

where $\langle \cdots \rangle_{\mathrm{cl}}$ denotes an average over classical configuration space, h is the Heaviside function, Q_r is the reactant partition function, and the normalized delta function $\Delta(\mathbf{r})$ is defined as

$$\Delta(\mathbf{r}) := ||\nabla \xi(\mathbf{r})||_{-} \delta[\xi(\mathbf{r})], \tag{1.8}$$

$|| \cdots ||_{-}$ being the norm of a covariant vector (see Table 1.1). Since we assumed the absence of recrossing during the derivation, k_{cTST} provides an upper bound on the true classical reaction rate constant; therefore, in order to approach the true reaction rate, the dividing surface should be chosen to minimize k_{cTST}, a notion central to the variational transition state theory [24].

The simplest quantum correction to Eq. (1.7) involves evaluating it with a harmonic approximation analogous to the Urey model for the partition function and equilibrium isotope effect, allowing to account for zero-point energy effects. The main difference is that for $\langle\Delta(\mathbf{r})\rangle_{\mathrm{cl}}$ one assumes the main contribution to the average to come from the neighborhood of a saddle point of $V(\mathbf{r})$ between the reactant and product regions. The result is often written as [25]

$$k_{\mathrm{cTST}} = \sigma_k \frac{1}{2\pi\beta\hbar} \frac{Q^{\ddagger}}{Q_r} e^{-\beta V^{\ddagger}}, \tag{1.9}$$

where $Q^{\ddagger}$ is a semiclassical partition function of the transition state which is the product of translational, rotational, and vibrational partition functions, the latter being evaluated for all internal degrees of freedom but for the unstable mode corresponding to motion along the reaction coordinate, $V^{\ddagger}$ is the activation energy, that is difference in the potential between the saddle point and the reactant potential minimum, and σ_k is the symmetry factor appearing if several equivalent saddle points need to be considered. Note the change of dimensionality of the prefactor caused by, in a sense, integrating out $\Delta(\mathbf{r})$ to obtain $Q^{\ddagger}$. In order to account for tunneling effects, several corrections have been proposed, the simplest one being the Wigner correction [26]

$$\frac{k_{\mathrm{cTST,Wigner}}}{k_{\mathrm{cTST}}} = 1 + \frac{(\beta\hbar|\omega^{\ddagger}|)^2}{24}, \tag{1.10}$$

where $\omega^{\ddagger}$ is the imaginary time frequency that corresponds to unstable motion along the reaction coordinate. The more sophisticated quantum corrections [27–29] allow to achieve an accuracy which is impressive for their minimal computational cost. However, having classical transition state theory as the starting point puts an upper bound to a method's accuracy, motivating introduction of several inherently quantum and semiclassical methods for calculating reaction rates. A brief review of these approaches is given in Sec. 1.4.

1.3 Kinetic isotope effects

In order to quantify the effect of isotope substitution on reaction rate constant the *kinetic isotope effect* is introduced. If A and B are two isotopologues of the same reactive system then the kinetic isotope effect is defined as

$$\mathrm{KIE} := \frac{k^{(A)}}{k^{(B)}}, \tag{1.11}$$

where $k^{(A)}$ and $k^{(B)}$ are reaction rate constants for A and B. The quantity is widely used in chemical kinetics, for example, to obtain qualitative information on the role played by the substituted atom in the rate limiting step of a complex mechanism [30, 31]; in this work we will mainly consider its application to detecting nuclear quantum effects on reaction rates.

First of all, it is educative to write out classical transition state theory expression of the kinetic isotope effect. If the motion along the reaction coordinate can be given an effective mass $m^{\ddagger}$, then k_{cTST} (1.7) takes the form

$$k_{\mathrm{cTST}} = \frac{1}{\sqrt{2\pi\beta}} \frac{\langle \delta[\xi(\mathbf{r})] ||\nabla\xi(\mathbf{r})||_0/\sqrt{m^{\ddagger}}\rangle_{\mathrm{cl}}}{\langle\{1-h[\xi(\mathbf{r})]\}\rangle_{\mathrm{cl}}} = \frac{1}{\sqrt{m^{\ddagger}}} \frac{1}{\sqrt{2\pi\beta}} \frac{\langle \delta[\xi(\mathbf{r})] ||\nabla\xi(\mathbf{r})||_0\rangle_{\mathrm{cl}}}{\langle\{1-h[\xi(\mathbf{r})]\}\rangle_{\mathrm{cl}}}. \tag{1.12}$$

It is obvious that if kinetic isotope effect (1.11) is evaluated from Eq. (1.12), then the mass-independent classical averages will cancel out, leaving only

$$\mathrm{KIE}_{\mathrm{cTST}} = \sqrt{\frac{m^{\ddagger(B)}}{m^{\ddagger(A)}}}. \tag{1.13}$$

It is clear that in most cases the expression should be close to unity and independent of temperature, therefore an anomalously large or small kinetic isotope effect indicates that strong quantum effects are at play. Investigating temperature-dependent kinetic isotope effects has been instrumental in studying several enzymatic systems [32, 33]. One of them, namely soybean lipoxygenase, is also a good example of an anomalously large kinetic isotope effect which is ~ 80 for substitution of hydrogen with deuterium in the native protein [34, 35], with even larger values being reported for some of its mutants [36]. Several explanations for this behavior have been proposed, including tunneling [37] and change of the effective donor-acceptor distance [38]. Kinetic isotope effects that are smaller than unity are also quite common and are typically caused by zero-point energy effects. An interesting example of such a kinetic isotope effect with an anomalously small value was reported for rates of $\mathrm{Mu} + \mathrm{H}_2$ and $\mathrm{He}\mu + \mathrm{H}_2$ reactions, where Mu is the so-called muonium atom and Heμ is the muonated helium atom [39, 40]; both atoms can be considered isotopes of hydrogen with masses of 0.11 and 4.11 atomic mass units. Studies suggest that it is caused by strong zero-point energy effect in $\mathrm{Mu} + \mathrm{H}_2$, which not only increases the reaction barrier, but also widens it, leading to a counterintuitively small tunneling contribution to the reaction rate [41, 42]. There is also a number of rather exotic cases when changing the isotope of an atom influences the reaction rate not through change of mass, but rather through a change in magnetic properties, nuclear volume, or symmetry of the system; such cases often lead to puzzling correlations between isotope mass and reaction rate and are called “mass-independent kinetic isotope effects” [43]. As mentioned earlier, in this work we mainly focused on quantum instanton approximation for the rate constant, which allows to largely account for tunneling and zero-point energy effects; it should thus be sufficient to accurately predict deviation of kinetic isotope effects from their classical values in most instances.

1.4 Overview of quantum and semiclassical methods of calculating rate constants

We now discuss different methods for calculating reaction rate constants that go beyond classical transition state theory. For systems where Born-Oppenheimer approximation is valid the reaction rate can be straightforwardly expressed in terms of barrier transition probability at a given energy; for a bimolecular reaction the expression reads [44]

$$k_{\mathrm{QM}}Q_r = \frac{1}{2\pi\hbar}\sum_{J=0}^{\infty}(2J+1)\int P(E,J)\exp(-\beta E)dE, \tag{1.14}$$

where k_{QM} is the exact quantum mechanical rate constant and $P(E,J)$ is transition probability for energy E and angular momentum J. Several algorithms that evaluate Eq. (1.14) exactly are currently available [45, 46], but while they have provided invaluable benchmark values for lower dimensional systems, the calculations become too computationally demanding as the dimensionality increases. This led to several approaches that simplify the problem by separating out rotations [47, 48], reducing the number of degrees of freedom that are treated quantum mechanically [49, 50], and expressing $P(E,J)$ in terms of quasiclassical trajectories [41, 51, 52]. A possible alternative is to rewrite Eq. (1.14) in a way that avoids individual scattering states; such an expression was proposed in Ref. [53] and reads

$$kQ_r = \mathrm{Tr}[\hat{F}\hat{\mathcal{P}}e^{-\beta\hat{H}}], \tag{1.15}$$

where $\hat{H}$ is the reactive system's Hamiltonian, $\hat{\mathcal{P}}$ is the projector on scattering states that correspond to the forward reaction and $\hat{F}$ is the operator of flux through a dividing surface separating reactant and product regions. A more convenient form of this expression is the Miller-Schwartz-Tromp [54] formula given by

$$k = \frac{1}{2Q_r}\int_{-\infty}^{+\infty} C_{\mathrm{ff}}(t)dt, \tag{1.16}$$

where $C_{\mathrm{ff}}(t)$ is the symmetrized flux-flux correlation function at time t,

$$C_{\mathrm{ff}}(t) := \mathrm{Tr}[\hat{F}_a e^{-(\beta/2-\mathrm{i}t/\hbar)\hat{H}}\hat{F}_b e^{-(\beta/2+\mathrm{i}t/\hbar)\hat{H}}], \tag{1.17}$$

$\hat{F}_\gamma$ ($\gamma \in \{a,b\}$) is operator of flux through dividing surface γ. Equation (1.16) expresses the reaction rate in terms of a correlation function, which in turn can be evaluated with several standard approaches. The most accurate one is multi-configurational time-dependent Hartree [55, 56], which is an important method for obtaining benchmark values. Another notable example is linearized semiclassical initial value representation method [57], a numerically efficient approach that combines exact quantum coordinate distribution with a semiclassical approximation to the propagator. Alternatively, one can note that the form of Eq. (1.16) implies that in the limit of $t \to \pm\infty$ $C_{\mathrm{ff}}(t)$ should approach zero, posing the question whether it is possible to evaluate the integral over $C_{\mathrm{ff}}(t)$ from the function's properties around its extrema [54]. This leads to a number of methods that involve choosing dividing surfaces in such a way that $C_{\mathrm{ff}}(t)$ is a maximum at $t = 0$ and decays fast enough to allow accurate evaluation of Eq. (1.16) using properties of $C_{\mathrm{ff}}(t)$ at $t = 0$. Introducing a semiclassical approximation to the Boltzmann operator leads [58] to the semiclassical instanton [44] formula [even though the original derivation of Ref. [44] started from Eq. (1.15) rather than Eq. (1.16)]; treating the Boltzmann operator exactly leads to a family of methods including Hansen-Andersen transition state theory [4, 5], quantum instanton approximation [3] and its extended version [59]. The latter three methods were central to this work and will be given a more detailed discussion in Chapters 4 and 5.

It is educative to give a short summary of other expressions for reaction rate constant that do not fall into the two categories outlined above, as well as how they are connected to Eq. (1.16). First of all, one needs to note the application of quantum linear response theory [60] to reaction rates [61]; the result is similar to Miller-Schwartz-Tromp formula (1.16), but instead of $C_{\mathrm{ff}}(t)$ one integrates $\tilde{C}_{\mathrm{ff}}(t)$ defined as

$$\tilde{C}_{\mathrm{ff}}(t) = \frac{1}{\beta}\int_0^{\beta} d\lambda \mathrm{Tr}[\hat{F}_a e^{\mathrm{i}\hat{H}t/\hbar} e^{-\lambda\hat{H}}\hat{F}_b e^{-(\beta-\lambda)\hat{H}} e^{-\mathrm{i}\hat{H}t/\hbar}] \tag{1.18}$$

It has been shown in Ref. [54] that integrals of $\tilde{C}_{\mathrm{ff}}(t)$ and $C_{\mathrm{ff}}(t)$ are equal; however, using $C_{\mathrm{ff}}(t)$ is more convenient for practical purposes as its evaluation does not requite integration over λ [54]. Secondly, several alternative approaches to instanton rate theory have also been developed, the oldest one being the "Im F" instanton formalism based on expressing the rate as imaginary part of free energy of a metastable state [62, 63]; the "Im F" instanton approach has been shown to be equivalent to the semiclassical instanton approach mentioned earlier [58, 64]. The accuracy of instanton-based approaches at low temperatures and classical transition state theory at higher temperatures also inspired two groups of methods aiming to accurately interpolate between the two limits. The first group constitutes several relatively recent semiclassical instanton based approaches [65–67], while the second group aimed to express the reaction rate in terms of Feynman imaginary time path integrals [68–71]. Development of the latter methods eventually led to the ring polymer dynamics transition state theory, which was originally introduced as application of the more general ring polymer molecular dynamics [72] approach to calculating reaction rate constants [73, 74] via Eq. (1.16). The resulting method was later shown to be connected to semiclassical instanton approaches [75] and to be a short-time approximation of the Miller-Schwartz-Tromp formula [76]; less computationally demanding methods that estimate ring polymer molecular dynamics rate have also been developed [75].

1.5 Feynman imaginary time path integral formalism

We have already mentioned imaginary time path integral formalism [10, 11] as the basis for calculating equilibrium properties exactly; it can also be used for easily evaluating properties of symmetrized correlation functions at time zero, which we will later use to calculate reaction rate constants via quantum instanton approximation. In this section, we will demonstrate how these quantum problems can be reduced to classical ones, with details specific for calculating equilibrium and kinetic isotope effects being left for Chapters 2, 3, and 4.

1.5.1 Basic path integral expressions

We start by rewriting the coordinate matrix element of the Boltzmann operator at inverse thermodynamic temperature β as a matrix element of the product of $P \in \mathbb{N}$ Boltzmann operators at a higher temperature inversely proportional to the integer parameter $\epsilon := \beta/P$:

$$\langle \mathbf{r}^{(a)} | e^{-\beta \hat{H}} | \mathbf{r}^{(b)} \rangle = \langle \mathbf{r}^{(a)} | (e^{-\epsilon \hat{H}})^P | \mathbf{r}^{(b)} \rangle. \tag{1.19}$$

We now proceed with a high-temperature factorization of the Boltzmann operator; in this work we considered three that were most efficient:

1. The symmetrized version [77] of the Lie-Trotter factorization [78]:

$$e^{-\epsilon \hat{H}} = e^{-\epsilon \hat{V}/2} e^{-\epsilon \hat{T}} e^{-\epsilon \hat{V}/2} + O\left(\epsilon^3\right). \tag{1.20}$$

This second-order factorization, which we will for simplicity call Lie-Trotter factorization, is the one most commonly used for discretizing the imaginary-time Feynman path integral.

2. The Takahashi-Imada factorization [79]:

$$\mathrm{Tr}\left(e^{-\epsilon \hat{H}}\right) = \mathrm{Tr}\left(e^{-\epsilon \hat{V}_{\mathrm{TI}}/2} e^{-\epsilon \hat{T}} e^{-\epsilon \hat{V}_{\mathrm{TI}}/2}\right) + O\left(\epsilon^5\right), \tag{1.21}$$

where

$$\hat{V}_{\mathrm{TI}} := \hat{V} + \frac{1}{24}\epsilon^2 [\hat{V}, [\hat{T}, \hat{V}]], \tag{1.22}$$

is an effective one-particle potential. This fourth-order factorization significantly accelerates the convergence to the quantum limit of the path integral expression for the partition function. However, it only behaves as a fourth-order factorization when it is used for evaluating the trace of the Boltzmann operator. If one naively removes the Tr in Eq. (1.21), and applies the resulting factorization

$$e^{-\epsilon \hat{H}} \approx e^{-\epsilon \hat{V}_{\mathrm{TI}}/2} e^{-\epsilon \hat{T}} e^{-\epsilon \hat{V}_{\mathrm{TI}}/2} \tag{1.23}$$

to correlation functions, one obtains only second-order convergence, and no numerical advantage over the LT factorization. Since it will allow us to provide a single derivation of many quantities for different factorizations, we will abuse terminology and refer to Eq. (1.23) also as "Takahashi-Imada" factorization, keeping in mind that the original authors were aware that their splitting is of the fourth order only in the context of Eq. (1.21).

3. The fourth-order Suzuki-Chin factorization (Ref. [80], motivated by Ref. [81]):

$$e^{-\epsilon \hat{H}} = e^{-\epsilon \hat{V}_{\mathrm{e}}/6} e^{-\epsilon \hat{T}/2} e^{-2\epsilon \hat{V}_{\mathrm{m}}/3} e^{-\epsilon \hat{T}/2} e^{-\epsilon \hat{V}_{\mathrm{e}}/6} + O\left(\epsilon^5\right), \tag{1.24}$$

where

$$\hat{V}_{\mathrm{e}} := \hat{V} + \frac{\alpha}{6}\epsilon^2[\hat{V},[\hat{T},\hat{V}]] \text{ and} \tag{1.25}$$

$$\hat{V}_{\mathrm{m}} := \hat{V} + \frac{(1-\alpha)}{12}\epsilon^2[\hat{V},[\hat{T},\hat{V}]] \tag{1.26}$$

are the "endpoint" and "midpoint" effective one-particle potentials. The dimensionless parameter α can assume an arbitrary value, but evidence in the literature [82, 83] suggests that $\alpha = 0$ gives superior results in most path integral simulations, and hence it was also the value used in this work.

Now we use one of the three path integral splittings for each of the P high-temperature factors in Eq. (1.19), with the caveat that for the Suzuki-Chin factorization (only) we replace P with $P/2$ (so P must be even) and $\epsilon = \beta/P$ with $\epsilon = 2\beta/P$ in Eq. (1.19). After inserting $(P-1)$ resolutions of identity in the coordinate basis in front of every kinetic factor (except the first one), we obtain

$$\langle \mathbf{r}^{(a)}|e^{-\beta\hat{H}}|\mathbf{r}^{(b)}\rangle = \lim_{P\to\infty} C\int d\mathbf{r}^{(1)}\cdots d\mathbf{r}^{(P-1)}\exp\left[-\beta\tilde{\Phi}(\mathbf{r}^{(a)},\mathbf{r}^{(1)},...,\mathbf{r}^{(P-1)},\mathbf{r}^{(b)})\right], \tag{1.27}$$

where the effective potential $\tilde{\Phi}$ and prefactor C are defined as

$$\tilde{\Phi}(\mathbf{r}^{(a)},\mathbf{r}^{(1)},...,\mathbf{r}^{(P-1)},\mathbf{r}^{(b)}) := \frac{P}{2\beta^2\hbar^2}\sum_{s=1}^{P}||\mathbf{r}^{(s)}-\mathbf{r}^{(s-1)}||_+^2 + \frac{1}{P}\sum_{s=0}^{P}\tilde{w}_s V_{\mathrm{eff}}^{(s)}(\mathbf{r}^{(s)}), \tag{1.28}$$

$$C := \left(\frac{P}{2\pi\beta\hbar^2}\right)^{DNP/2}\left(\prod_{i=1}^{N} m_i\right)^{DP/2}. \tag{1.29}$$

In the expression for $\tilde{\Phi}$, we use the notation $\mathbf{r}^{(P)} := \mathbf{r}^{(b)}$, $\mathbf{r}^{(0)} := \mathbf{r}^{(a)}$ for the boundary points; m_i is the mass of particle i, $||\cdots||_+$ is the norm of a contravariant vector (see Table 1.1), and $V_{\mathrm{eff}}^{(s)}$ is the effective one-particle potential,

$$V_{\mathrm{eff}}^{(s)} := V + \left(\frac{\beta}{P}\right)^2 d_s V_{\mathrm{grad}}, \tag{1.30}$$

where

$$V_{\mathrm{grad}}(\mathbf{r}) = \hbar^2||\nabla V(\mathbf{r})||_-^2 \tag{1.31}$$

is the coordinate representation of the commutator term in Eqs. (1.22), (1.25), and (1.26). In the context of discretized path integrals, the integer P is often referred to as the Trotter number.

The coefficient d_s for the fourth-order correction of an effective one-particle potential

Table 1.2: Dependence of weights $\tilde{w}_s$ on the bead number s and Boltzmann factorization.

Splitting	$s = 1$ or $s = P$	s odd	s even
Lie-Trotter, Takahashi-Imada	1/2	1	1
Suzuki-Chin	1/3	4/3	2/3

depends on the splitting used:

$$d_s = \begin{cases} 0, & \text{Lie-Trotter splitting,} \\ 1/24, & \text{Takahashi-Imada splitting,} \\ \alpha/6, & \text{Suzuki-Chin splitting and } s \text{ even,} \\ (1-\alpha)/12, & \text{Suzuki-Chin splitting and } s \text{ odd.} \end{cases} \tag{1.32}$$

The weights $\tilde{w}_s$ in the sum over effective one-particle potentials also depend on the splitting, their values are summarized in Table 1.2. Expression (1.27) becomes exact as P goes to infinity.

1.5.2 Using path integral formalism to calculate equilibrium properties

Equation (1.27) allows to rewrite partition function Q as

$$\begin{aligned} Q = \mathrm{Tr}(e^{-\beta\hat{H}}) &= \int d\mathbf{r}^{(P)} \langle \mathbf{r}^{(P)} | e^{-\beta\hat{H}} | \mathbf{r}^{(P)} \rangle \\ &= \lim_{P\to\infty} Q_P, \end{aligned} \tag{1.33}$$

where Q_P path integral representation of Q which reads

$$Q_P = \int \rho(\{\mathbf{r}^{(s)}\}) d\{\mathbf{r}^{(s)}\}, \tag{1.34}$$

where $\rho(\{\mathbf{r}^{(s)}\})$ is the unnormalized probability density

$$\rho = C \exp[-\beta\Phi(\{\mathbf{r}^{(s)}\})] \tag{1.35}$$

and $\Phi(\{\mathbf{r}^{(s)}\})$ is the effective potential

$$\begin{aligned} \Phi(\{\mathbf{r}^{(s)}\}) &= \tilde{\Phi}(\mathbf{r}^{(P)}, \mathbf{r}^{(1)}, ..., \mathbf{r}^{(P-1)}, \mathbf{r}^{(P)}) \\ &= \frac{P}{2\beta^2\hbar^2} \sum_{s=1}^{P} ||\mathbf{r}^{(s)} - \mathbf{r}^{(s-1)}||_+^2 + \frac{1}{P} \sum_{s=1}^{P} w_s V(\mathbf{r}^{(s)}), \end{aligned} \tag{1.36}$$

where we use the notation $\mathbf{r}^{(0)} := \mathbf{r}^{(P)}$, $w_P = 2\tilde{w}_P$ and $w_s = \tilde{w}_s$ for $s \neq P$. From now on we will distinguish path integral representation of a quantity from its exact form by adding subscript P.

We can now see that the quantum partition function is expressed as a classical partition function of a system with an increased dimensionality. The expression makes it possible to evaluate free energy of the system [84], however, just as in classical thermodynamic calculations, it is much more convenient to express needed quantities in terms of averages that can be evaluated during a standard Monte Carlo or molecular dynamics simulation with $\Phi(\{\mathbf{r}^{(s)}\})$ as the effective potential. Note that running such a simulation results in each $\mathbf{r}^{(s)}$ having a probability density of $\langle\mathbf{r}^{(s)}|\exp(-\beta\hat{H})|\mathbf{r}^{(s)}\rangle/Q$, that is the exact quantum distribution of $\hat{\mathbf{r}}$. Consequently, the simulation allows to recover probability distributions of all coordinate dependent quantities [11, 85], one particular example being the reaction coordinate in a reactive system, which can be used to calculate equilibrium constants [16]. We note that it is possible to evaluate momentum distribution as well [85, 86] using an "open path integral" simulation; the method is based on the following equality

$$\begin{aligned}\langle\mathbf{p}|e^{-\beta\hat{H}}|\mathbf{p}\rangle =& \int\langle\mathbf{p}|\mathbf{r}^{(a)}\rangle\langle\mathbf{r}^{(a)}|e^{-\beta\hat{H}}|\mathbf{r}^{(b)}\rangle\langle\mathbf{r}^{(b)}|\mathbf{p}\rangle d\mathbf{r}^{(a)}d\mathbf{r}^{(b)}\\ =&(2\pi\hbar)^{-DN}\int\langle\mathbf{r}^{(a)}|e^{-\beta\hat{H}}|\mathbf{r}^{(b)}\rangle e^{\mathrm{i}\langle\mathbf{p},\mathbf{r}^{(b)}-\mathbf{r}^{(a)}\rangle_0/\hbar}d\mathbf{r}^{(a)}d\mathbf{r}^{(b)}\\ =&(2\pi\hbar)^{-DN}\lim_{P\to\infty}C\int d\mathbf{r}^{(1)}\cdots d\mathbf{r}^{(P-1)}d\mathbf{r}^{(a)}d\mathbf{r}^{(b)}\\ &\times\exp\left[-\beta\tilde{\Phi}(\mathbf{r}^{(a)},\mathbf{r}^{(1)},...,\mathbf{r}^{(P-1)},\mathbf{r}^{(b)})\right]e^{\mathrm{i}\langle\mathbf{p},\mathbf{r}^{(b)}-\mathbf{r}^{(a)}\rangle_0/\hbar},\end{aligned}\tag{1.37}$$

where $\mathbf{p}$ is the system's momentum vector. It is now easy to see that the system's momentum distribution can be obtained by running a simulation in $(\mathbf{r}^{(a)},\mathbf{r}^{(1)},\dots,\mathbf{r}^{(P)},\mathbf{r}^{(b)})$ with $\tilde{\Phi}(\mathbf{r}^{(a)},\mathbf{r}^{(1)},\dots,\mathbf{r}^{(P)},\mathbf{r}^{(b)})$ as the effective potential and calculating Fourier transform of the resulting distribution of $\mathbf{r}^{(b)}-\mathbf{r}^{(a)}$.

An important class of system's properties that can be calculated with path integral methods are logarithmic derivatives of Q. A derivative of $\ln Q_P$ with respect to an arbitrary parameter λ can be rewritten as

$$\begin{aligned}\frac{d\ln Q_P}{d\lambda}=&\frac{dQ_P/d\lambda}{Q_P}=\frac{\int[d\rho(\{\mathbf{r}^{(s)}\})/d\lambda]d\{\mathbf{r}^{(s)}\}}{\int\rho(\{\mathbf{r}^{(s)}\})d\{\mathbf{r}^{(s)}\}}\\ =&\frac{\int[d\ln\rho(\{\mathbf{r}^{(s)}\})/d\lambda]\rho(\{\mathbf{r}^{(s)}\})d\{\mathbf{r}^{(s)}\}}{\int\rho(\{\mathbf{r}^{(s)}\})d\{\mathbf{r}^{(s)}\}}.\end{aligned}\tag{1.38}$$

To rewrite such relations in a more compact form, notion of an *estimator* is introduced. We will denote an estimator for A as A_{est}, which is a function of $\{\mathbf{r}^{(s)}\}$ that satisfies

$$A=\frac{\int A_{\mathrm{est}}\rho(\{\mathbf{r}^{(s)}\})d\{\mathbf{r}^{(s)}\}}{\int\rho(\{\mathbf{r}^{(s)}\})d\{\mathbf{r}^{(s)}\}}.\tag{1.39}$$

In other words, A can be recovered by running a Monte Carlo or molecular dynamics simulation with $\Phi(\{\mathbf{r}^{(s)}\})$ as the effective potential and calculating the average of A_{est}. Therefore, using Eq. (1.38) we can write

$$\begin{aligned}\left(\frac{d\ln Q_P}{d\lambda}\right)_{\mathrm{est}}=&\frac{d\ln\rho(\{\mathbf{r}^{(s)}\})}{d\lambda}\\ =&\frac{d\ln C}{d\lambda}-\frac{d[\beta\Phi(\{\mathbf{r}^{(s)}\})]}{d\lambda}.\end{aligned}\tag{1.40}$$

If we, for example, consider β as the λ in question, then straightforward differentiation of Eq. (1.40) leads to the "thermodynamic" estimator for energy [87], whose statistical behavior can be improved by applying the virial theorem [88] or rewriting $\rho(\{\mathbf{r}^{(s)}\})$ in terms of β-scaled coordinates prior to the differentiation [89, 90]. (The latter approach has proven to be the most effective and was also applied to calculations of heat capacity [91]). Another problem where logarithmic derivatives are extensively used is finding free energy differences between systems of the same dimensionality but different Hamiltonians. Suppose the systems in question are A and B, while $Q^{(A)}$ and $Q^{(B)}$ are their partition functions, whose path integral representations can be written as

$$Q_P^{(A)} = \int \rho^{(A)}(\{\mathbf{r}^{(s)}\})d\{\mathbf{r}^{(s)}\}, \tag{1.41}$$

$$Q_P^{(B)} = \int \rho^{(B)}(\{\mathbf{r}^{(s)}\})d\{\mathbf{r}^{(s)}\}. \tag{1.42}$$

In this case the ratio $Q^{(A)}/Q^{(B)}$ can be found by setting dimensionless parameter $\lambda \in [0,1]$ and introducing $\rho^{(\lambda)}(\{\mathbf{r}^{(s)}\})$ such that

$$\rho^{(1)}(\{\mathbf{r}^{(s)}\}) = \rho^{(B)}(\{\mathbf{r}^{(s)}\}), \tag{1.43}$$

$$\rho^{(0)}(\{\mathbf{r}^{(s)}\}) = \rho^{(A)}(\{\mathbf{r}^{(s)}\}), \tag{1.44}$$

and $\rho^{(\lambda)}(\{\mathbf{r}^{(s)}\})$ is continuous with respect to λ. $Q_P^{(B)}/Q_P^{(A)}$ can be rewritten as

$$\frac{Q_P^{(B)}}{Q_P^{(A)}} = \exp\left(\int_0^1 \frac{d\ln Q^{(\lambda)}}{d\lambda} d\lambda\right), \tag{1.45}$$

where we introduced

$$Q_P^{(\lambda)} = \int \rho^{(\lambda)}(\{\mathbf{r}^{(s)}\})d\{\mathbf{r}^{(s)}\}. \tag{1.46}$$

Equation (1.40) allows to calculate $d\ln Q/d\lambda$ at any value of λ, making it possible to evaluate the integral in Eq. (1.45) with a numerical scheme such as Simpson's rule. Such an approach is called "thermodynamic integration" [92, 93], and in Chapter 2 we will discuss in detail how it can be applied to equilibrium isotope effects, when A and B are two isotopologues and varying λ corresponds to a change of mass. Several alternatives to thermodynamic integration have also been proposed; they are thoroughly discussed in Chapters 2 and 3 in the context of equilibrium isotope effect calculations. Probably the oldest one is the free energy perturbation method [94–96], which is based on rewriting $Q_P^{(B)}/Q_P^{(A)}$ as

$$\begin{aligned}\frac{Q_P^{(B)}}{Q_P^{(A)}} &= \frac{\int \rho^{(B)}(\{\mathbf{r}^{(s)}\})d\{\mathbf{r}^{(s)}\}}{\int \rho^{(A)}(\{\mathbf{r}^{(s)}\})d\{\mathbf{r}^{(s)}\}} \\ &= \frac{\int [\rho^{(B)}(\{\mathbf{r}^{(s)}\})/\rho^{(A)}(\{\mathbf{r}^{(s)}\})]\rho^{(A)}(\{\mathbf{r}^{(s)}\})d\{\mathbf{r}^{(s)}\}}{\int \rho^{(A)}(\{\mathbf{r}^{(s)}\})d\{\mathbf{r}^{(s)}\}},\end{aligned} \tag{1.47}$$

leading to the Zwanzig formula [94]

$$\left(\frac{Q_P^{(B)}}{Q_P^{(A)}}\right)_{\text{est}} = \frac{\rho^{(B)}(\{\mathbf{r}^{(s)}\})}{\rho^{(A)}(\{\mathbf{r}^{(s)}\})}, \tag{1.48}$$

with the averaging taken over $\rho^{(A)}(\{\mathbf{r}^{(s)}\})$. The approach works best if $\rho^{(A)}(\{\mathbf{r}^{(s)}\})$ and $\rho^{(B)}(\{\mathbf{r}^{(s)}\})$ do not differ much, as will also be discussed in Chapter 3.

It is necessary to note that all methods for computing isotope effects discussed in this work are variations of either thermodynamic integration or free energy perturbation methods. For the more general problem of calculating free energy differences, however, it is possible to have a system where neither of these two approaches is suitable for the calculation. In this case, a third option is to run a simulation which samples the distribution $\rho^{(\lambda)}(\{\mathbf{r}^{(s)}\})$ with respect to both $\{\mathbf{r}^{(s)}\}$ and $\lambda \in [0, 1]$ (for example, with an adiabatic free energy dynamics simulation [97]), and then calculate $Q_P^{(B)}/Q_P^{(A)}$ from the ratio of probability densities at $\lambda = 0$ and $\lambda = 1$ [98, 99]. Unfortunately, approaches based on calculating probability density ratios tend to suffer from inherent convergence problems [100], and are therefore not considered here.

1.5.3 Path integral formalism and symmetrized correlation functions

While so far we have only considered applications of path integral formalism to equilibrium properties, it can facilitate calculating dynamic properties as well. "Im F" instanton theory and ring polymer molecular dynamics are two such examples and were already mentioned in Sec. 1.4. In this work, we will use path integral formalism to estimate properties of symmetrized correlation functions at time zero which, in turn, will be used to calculate reaction rate constants via Miller-Schwartz-Tromp formula (1.16). The details of the method will be discussed in greater detail in Chapters 4 and 5; here as an example we will present path integral expression of a symmetrized correlation function $C_{AB}(t)$ of two coordinate-dependent quantities $A(\mathbf{r})$ and $B(\mathbf{r})$

$$C_{AB}(t) := \mathrm{Tr}[A(\hat{\mathbf{r}})e^{-(\beta/2-\mathrm{i}t/\hbar)\hat{H}}B(\hat{\mathbf{r}})e^{-(\beta/2+\mathrm{i}t/\hbar)\hat{H}}]. \tag{1.49}$$

At $t = 0$ the function can be written as

$$\begin{aligned} C_{AB}(0) &= \mathrm{Tr}[A(\hat{\mathbf{r}})e^{-\beta\hat{H}/2}B(\hat{\mathbf{r}})e^{-\beta\hat{H}/2}] \\ &= \int A(\mathbf{r}^{(P/2)})B(\mathbf{r}^{(P)})\langle\mathbf{r}^{(P)}|e^{-\beta\hat{H}/2}|\mathbf{r}^{(P/2)}\rangle\langle\mathbf{r}^{(P/2)}|e^{-\beta\hat{H}/2}|\mathbf{r}^{(P)}\rangle d\mathbf{r}^{(P/2)}d\mathbf{r}^{(P)}. \end{aligned} \tag{1.50}$$

Rewriting the off-diagonal Boltzmann operator elements analogously to Eq. (1.27) while discretizing each $\beta/2$ into $P/2$ slices leads to

$$C_{AB}(0) = \lim_{P\to\infty} C_{AB,P}(0), \tag{1.51}$$

where $C_{AB,P}(0)$ is the path integral representation of $C_{AB}(0)$ given by

$$C_{AB,P}(0) = \int A(\mathbf{r}^{(P/2)})B(\mathbf{r}^{(P)})\rho(\{\mathbf{r}^{(s)}\})d\{\mathbf{r}^{(s)}\}. \tag{1.52}$$

Let us now choose $A = \Delta_a$ and $B = \Delta_b$, where a and b are two dividing surfaces defined by $\xi_a(\mathbf{r}) = 0$ and $\xi_b(\mathbf{r}) = 0$, while Δ_a and Δ_b are normalized delta functions for dividing surfaces a and b defined analogously to Eq. (1.8). The resulting C_{AB} is known as delta-delta correlation function C_{dd} and its path integral representation at $t = 0$ reads

$$C_{\mathrm{dd},P}(0) = \int \rho^{\ddagger}(\{\mathbf{r}^{(s)}\})d\{\mathbf{r}^{(s)}\}, \tag{1.53}$$

where $\rho^{\ddagger}$ is the "constrained" version of ρ

$$\rho^{\ddagger}(\{\mathbf{r}^{(s)}\}) = \rho(\{\mathbf{r}^{(s)}\}) \prod_{\gamma=a,b} \Delta_{\gamma}(\mathbf{r}_{\gamma}), \tag{1.54}$$

with $\mathbf{r}_a := \mathbf{r}^{(P/2)}$ and $\mathbf{r}_b := \mathbf{r}^{(P)}$. $C_{\mathrm{dd},P}(0)$ and $\rho^{\ddagger}(\{\mathbf{r}^{(s)}\})$ will be often encountered in Chapter 4, where we will discuss properly how the quantum instanton approximation allows to rewrite the Miller-Schwartz-Tromp formula (1.16) in terms of $C_{\mathrm{dd}}(0)/Q_r$ and averages over $\rho^{\ddagger}(\{\mathbf{r}^{(s)}\})$.

1.5.4 Details of numerical performance

All the formulas presented in this section were written in a manner general for three different Boltzmann operator splittings most commonly used in path integral calculations. The error terms in Eqs. (1.20), (1.21), and (1.24) show that using fourth-order splittings instead of Lie-Trotter splitting accelerates convergence of path integral expressions to their quantum limit with increasing P. Unfortunately, this improvement comes with an additional computational cost, because if Lie-Trotter splitting is used then $V_{\mathrm{eff}}^{(s)}$ simply equals the classical system's potential V, but for a fourth-order splitting $V_{\mathrm{eff}}^{(s)}$ also includes a gradient-dependent correction. If force is not needed during the simulation (which is most often the case for Monte Carlo calculations), then the need to additionally calculate it in order to evaluate the gradient correction can constitute a significant additional cost; whether numerical benefits of using fourth-order splittings are worth the extra computational effort depends on the system. If the gradient of the potential is calculated during the simulation, as in the case of molecular dynamics, then an elegant numerical scheme [101] allows to use fourth-order splittings at a cost comparable to the one of Lie-Trotter splitting. The idea is to note that even though ∇V_{grad} formally depends on the Hessian, it can be expressed in terms of a finite difference containing just the gradient; the philosophy is similar to the way we will avoid calculating the Hessian for Hessian-dependent quantities in Chapter 4.

Throughout this section, we have assumed that the Born-Oppenheimer approximation is valid and that one needs to consider only one potential energy surface. Although situations when this is not the case were beyond the scope of this work, let us mention that the partition function of a nonadiabatic system can be expressed in terms of a path integral over continuous variables, some of which correspond to the change of electronic state [102]. This idea is also used in several ring polymer molecular dynamics methods that have been proposed for treating nonadiabatic processes [103–105]. We have not discussed how to evaluate $V(\mathbf{r})$ in an optimal manner as the problem is mostly analogous to the case of a classical simulation. However, one interesting trick which *is* specific to path integral calculations is the *ring polymer contraction* method, which involves decomposing $V(\mathbf{r})$ into slowly- and rapidly-varying contributions and effectively using different values of P for the two parts [106, 107]. While the idea was initially introduced for force field potentials, it has been recently extended to *ab initio* calculations as well [108].

2 Improving thermodynamic integration with respect to mass

2.1 Introduction

The results presented in this chapter have also been published in Ref. [2].

In the previous chapter, we mentioned two popular approaches for calculating isotope effects: the relatively cheap harmonic approximation (1.6) and using the formally exact Feynman path integral formalism to express isotope effect in terms of classical averages over $\Phi(\{\mathbf{r}^{(s)}\})$, which can then be calculated with molecular dynamics or Monte Carlo methods. To illustrate the benefits of the latter approach, in Figure 2.1 we plot the relative error of CD_4/CH_4 IE calculated with the harmonic approximation (1.6) (the values which are considered exact will be calculated in this chapter). In this example, the harmonic approximation works rather well at higher temperatures, where the isotope effect is small, but its error reaches as much as 60% at the low temperature of 200 K, where the isotope effect becomes very large. Feynman path integral formalism avoids introducing these systematic errors altogether, and in this chapter we focus on its combination with thermodynamic integration [92, 109, 110] with respect to mass [93, 111–114]. Even though the method is formally exact, a practical calculation contains errors that come from three sources. The first is the path integral discretization error, which comes from using a finite number P to obtain path integral representation of the partition function Q_P (1.33); this problem can be made less pressing by employing higher-order Boltzmann operator factorizations [83, 115–117], as was mentioned in Sec. 1.5. The second error is the statistical error which is inherent to evaluating $d\ln Q_P^{(\lambda)}/d\lambda$ using a Monte Carlo method; this error depends on the estimator used for the calculation, as will be discussed in Sec. 2.2.1. The last type of error, which is the focus of this chapter, is the integration error, which appears when the integral of logarithmic derivative of the partition function (1.45) is evaluated with a numerical scheme; even though several elegant tricks reduce this integration error

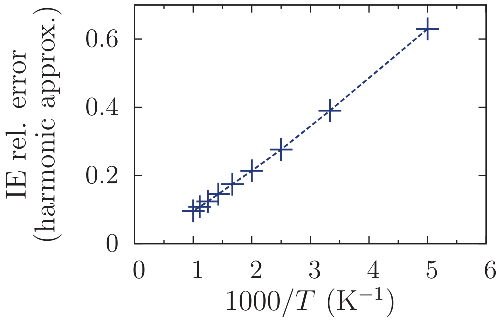

Figure 2.1: Temperature dependence of the relative error of the CD_4/CH_4 isotope effect (IE) obtained with the harmonic approximation (see Sec. 1.1). The result of stochastic thermodynamic integration (STI) serves as a reference; the relative error is defined as IE(harmonic)/IE(STI) - 1.

significantly [96, 116], it can never be removed completely if the integral is evaluated deterministically.

One way to bypass the problem is to use the free energy perturbation approach (1.48), a possibility that will be thoroughly discussed in Chapter 3. In this chapter we focus on eliminating integration error by allowing the mass to take a continuous range of values during the simulation, which allows to avoid discretizing the mass integral [93]; this approach is an example of a more general λ-dynamics method [118–120] for calculating free energy differences. Not only do these techniques eliminate the integration error, but they also tend to show faster statistical convergence than standard thermodynamic integration [121]; this property is similar to the improvement achieved by parallel tempering [122–124]. In this chapter, we present an approach that follows this philosophy, but introduces two additional modifications. First, we introduce a Monte Carlo procedure which is applicable for the specific case of the change of mass and enables a faster exploration of the λ dimension. Second, we show that the integration error can be reduced to zero exactly by using a piecewise linear umbrella biasing potential; the only remaining error of the calculated isotope effect is due to statistical factors and discretization error of the Boltzmann operator.

To assess the numerical performance of the proposed methodology, we apply it to the isotope effects in an eight-dimensional harmonic model and in a full-dimensional CH_4 molecule. Methane was chosen because the $CH_4 + D_2$ exchange is an important benchmark reaction for studying catalysis of hydrogen exchange over metals [125] and metal oxides [126], and because the polydeuterated species $CH_{4-x}D_x$ are formed in abundance during the catalyzed reaction.

2.2 Theory

2.2.1 Thermodynamic integration with respect to mass

Our ultimate goal is evaluating the isotope effect (1.2), i.e., a ratio of partition functions corresponding to two isotopologues. Although it is possible to evaluate partition functions $Q_P^{(A)}$ and $Q_P^{(B)}$ themselves with a Monte Carlo procedure [84], it is more convenient to calculate the ratio $Q_P^{(B)}/Q_P^{(A)}$ directly. We now review the most common of such direct approaches, based on thermodynamic integration [92] with respect to mass [111].

The basic expression for thermodynamic integration (1.45) has already been presented in Sec. 1.5 for a general case of a free energy change; to apply this method to isotope effects we need to introduce a continuous change of mass. Therefore we define, for each atom i, a continuous function $m_i^{(\lambda)}$ of λ such that

$$m_i^{(0)} = m_i^{(A)}, \tag{2.1}$$

$$m_i^{(1)} = m_i^{(B)}. \tag{2.2}$$

The simplest possible choice for the interpolating function is the linear interpolation

$$m_i^{(\lambda)} = (1-\lambda)\, m_i^{(A)} + \lambda m_i^{(B)}, \tag{2.3}$$

used in Refs. [111–113], but Ceriotti and Markland [96] showed that a faster convergence, especially in the deep quantum regime, is often achieved by interpolating the inverse square roots of the masses,

$$\frac{1}{\sqrt{m_i^{(\lambda)}}} = (1-\lambda)\,\frac{1}{\sqrt{m_i^{(A)}}} + \lambda\frac{1}{\sqrt{m_i^{(B)}}}, \tag{2.4}$$

which is therefore the interpolation used in the numerical examples in this chapter, unless explicitly mentioned otherwise.

Letting $Q^{(\lambda)}$ denote the partition function of a fictitious system with interpolated masses $m_i^{(\lambda)}$ allows us to use the general thermodynamic integration expression (1.45), which is often rewritten as

$$\frac{Q^{(B)}}{Q^{(A)}} = \exp\left[\int_0^1 \frac{d\ln Q^{(\lambda)}}{d\lambda} d\lambda\right] \tag{2.5}$$

$$= \exp\left[-\beta\int_0^1 \frac{dF(\lambda)}{d\lambda} d\lambda\right], \tag{2.6}$$

where $F(\lambda)$ is the free energy corresponding to the isotope change. As mentioned in Sec. 1.5, for each λ one can calculate $dF_P(\lambda)/d\lambda$ by calculating thermodynamic average of the corresponding estimator. Straightforwardly using the general expression for an estimator of a logarithmic derivative of the partition function (1.40) leads to the so-called thermodynamic estimator

$$[dF(\lambda)/d\lambda]_{\mathrm{th}} = -\frac{1}{\beta}\sum_{i=1}^{N}\frac{dm_i}{d\lambda}\left[\frac{DP}{2m_i} - \frac{P}{2\beta\hbar^2}\sum_{s=1}^{P}|\mathrm{r}_i^{(s)} - \mathrm{r}_i^{(s-1)}|^2\right]. \tag{2.7}$$

However, since it is a difference of two terms proportional to P, this estimator has a statistical error that grows with the Trotter number P, further increasing the computational cost. This drawback motivated the introduction [112] of the centroid virial estimator $[dF(\lambda)/d\lambda]_{\mathrm{cv}}$ whose statistical error is independent of P, a property mirroring the property of an analogous centroid virial estimator for kinetic energy [89, 90, 127]. The centroid virial estimator, derived in Appendix A, is given by

$$[dF(\lambda)/d\lambda]_{\mathrm{cv}} = -\sum_{i=1}^{N}\frac{1}{2m_i}\frac{dm_i}{d\lambda}\left\{\frac{D}{\beta} + \frac{1}{P}\sum_{s=1}^{P}\left[(\mathrm{r}_i^{(s)} - \mathrm{r}_i^{(C)})\cdot\nabla_i V(\mathbf{r}^{(s)})\right]\right\}, \tag{2.8}$$

where

$$\mathbf{r}^{(C)} := \frac{1}{P}\sum_{s=1}^{P}\mathbf{r}^{(s)} \tag{2.9}$$

is the centroid coordinate of the polymer ring. All numerical examples in this chapter use the centroid virial estimators, unless explicitly mentioned otherwise.

To summarize, using thermodynamic integration, the isotope effect (1.2) is evaluated as

$$\frac{Q_P^{(B)}}{Q_P^{(A)}} = \exp\left\{-\beta\int_0^1 \langle[dF(\lambda)/d\lambda]_{\mathrm{cv}}\rangle^{(\lambda)}\, d\lambda\right\}. \tag{2.10}$$

The calculation of the isotope effect requires running simulations at different values of λ and then numerically evaluating the integral in Eq. (2.10) using, for example, the trapezoidal, midpoint, or Simpson rule.

2.2.2 Stochastic thermodynamic integration with respect to mass

It is evident that the method of thermodynamic integration introduces an integration error, and therefore several approaches have been proposed to decrease it: While Ceriotti and Markland [96] optimized the interpolation functions $m_i^{(\lambda)}$ in order to make $dF_P(\lambda)/d\lambda$ as flat as possible over the integration interval, and thus obtained Eq. (2.4), Maršálek and Tuckerman [116] introduced higher-order derivatives of $Q_P^{(\lambda)}$ with respect to λ. Both modifications decrease the integration error, but do not eliminate it completely. In this subsection we show that including the λ variable as an additional dimension in the Monte Carlo simulation allows to make the integration error exactly zero if an appropriate sampling procedure is used.

To illustrate why it makes sense to evaluate the λ integral stochastically, let us consider a "standard" thermodynamic integration protocol from the previous subsection, where the integral in Eq. (2.5) is evaluated deterministically by discretizing the λ interval $[0, 1]$

into J subintervals of the form $I_j = [\lambda_{j-1}, \lambda_j]$, typically with $\lambda_j = j/J$ $(j = 0, \ldots, J)$. For example, employing the midpoint rule for the integral, one would run a separate Monte Carlo simulation for each $\bar{\lambda}_j := (\lambda_{j-1} + \lambda_j)/2 = (j - 1/2)/J \in I_j$ $(j = 1, \ldots, J)$ in order to calculate $dF_P(\lambda)/d\lambda|_{\lambda=\bar{\lambda}_j}$. Suppose we increase J while keeping the length of each simulation inversely proportional to J. Then the total number of Monte Carlo steps used will remain constant, the integration error will decrease, and the statistical error of the evaluated isotope effect will be close to a limiting value as long as each individual simulation is statistically converged. Unfortunately, for a fixed overall cost one cannot use arbitrarily large values of J, since that would render the individual simulations so short that their ergodicity would no longer be guaranteed. If ergodicity of an individual simulation requires at least M_{erg} Monte Carlo steps, the cost of the calculation will grow as $\mathcal{O}(J\, M_{\text{erg}})$, making the limit $J \to \infty$ unattainable in practice.

If, instead of J separate simulations for each $\bar{\lambda}_j$, one performs a single Monte Carlo simulation in a configuration space with an extra dimension corresponding to λ, the average of estimator $[dF(\lambda)/d\lambda]_{\text{cv}}$ over each subinterval I_j will give an estimate for $dF(\lambda)/d\lambda|_{\lambda=\bar{\lambda}_j}$, and one can use much higher values of J (and therefore obtain smaller integration errors) without sacrificing ergodicity of the simulation. This trick bears some resemblance to umbrella integration [100, 128, 129] and adaptive biasing force [130–132] approaches used to find the dependence of free energy on a reaction coordinate, but here the role of reaction coordinate is taken by isotope masses. As in umbrella integration, decreasing the widths of the λ intervals I_j decreases the integration error without affecting the statistical error of the computed isotope effect.

Running a Monte Carlo simulation in a configuration space augmented by λ requires, first of all, a correct sampling weight, $\rho^{(\lambda)}(\{\mathbf{r}^{(s)}\})$, which is nothing but $\rho(\{\mathbf{r}^{(s)}\})$ with masses $m_i^{(\lambda)}$ evaluated at a given value λ. The second most important thing is a corresponding Monte Carlo trial move together with an acceptance rule. The simplest possible trial move with respect to λ changes the initial λ' to any other $\lambda'' \in [0, 1]$ with equal probability, and keeps the Cartesian coordinates $\{\mathbf{r}^{(s)}\}$ of the ring polymer fixed. The resulting ratio of probability densities corresponding to λ'' and λ' is

$$\frac{\rho^{(\lambda'')}(\{\mathbf{r}^{(s)}\})}{\rho^{(\lambda')}(\{\mathbf{r}^{(s)}\})} = \left(\prod_{i=1}^{N} \frac{m_i^{(\lambda'')}}{m_i^{(\lambda')}}\right)^{PD/2} \exp\left[\frac{P}{2\beta\hbar^2} \sum_{i=1}^{N} (m_i^{(\lambda')} - m_i^{(\lambda'')}) \sum_{s=1}^{P} |\mathrm{r}_i^{(s)} - \mathrm{r}_i^{(s-1)}|^2\right], \tag{2.11}$$

which, as a function of λ'', has a maximum that unfortunately becomes sharper with larger P. A simple way to keep acceptance probability high even for large values of P is to generate trial λ'' such that $|\lambda'' - \lambda'| \leq \Delta\lambda_{\max}$. The following Monte Carlo procedure satisfies this condition and also preserves the acceptance ratio given by Eq. (2.11):

Simple λ-move:

1. Trial move:

$$\lambda' \mapsto \lambda'' = \lambda' + \Delta\lambda, \text{ where} \tag{2.12}$$

$$\Delta\lambda \in [-\Delta\lambda_{\max}, \Delta\lambda_{\max}] \text{ and distributed uniformly.} \tag{2.13}$$

2. Readjust the trial move to satisfy $\lambda'' \in [0, 1]$:

$$\text{if } (\lambda'' < 0) \text{ then } \lambda'' \mapsto -\lambda'', \tag{2.14}$$

$$\text{if } (\lambda'' > 1) \text{ then } \lambda'' \mapsto 2 - \lambda''. \tag{2.15}$$

3. Accept the final trial move with a probability

$$\min\left\{1, \left(\prod_{i=1}^{N} \frac{m_i^{(\lambda'')}}{m_i^{(\lambda')}}\right)^{PD/2} \exp\left[\frac{P}{2\beta\hbar^2} \sum_{i=1}^{N} (m_i^{(\lambda')} - m_i^{(\lambda'')}) \sum_{s=1}^{P} |\mathrm{r}_i^{(s)} - \mathrm{r}_i^{(s-1)}|^2\right]\right\}. \tag{2.16}$$

The procedure defined by Eqs. (2.12)-(2.16) is almost free in terms of computational time, but at very large values of P, even with the restriction (2.13), it becomes ineffective at sampling λ values far from the maximum of the probability ratio (2.11). This problem can be bypassed if the trial move with respect to λ preserves the mass-scaled normal modes of the ring polymer instead of the Cartesian coordinates, resulting in the following Monte Carlo procedure derived in Appendix A:

Mass-scaled λ-move:

1. Trial move:

$$\lambda' \mapsto \lambda'' \in [0, 1] \text{ and distributed uniformly,} \tag{2.17}$$

$$\mathbf{r}^{(s)} \mapsto \mathbf{r}^{(s)}_{\lambda',\lambda''}, \tag{2.18}$$

where

$$\mathrm{r}^{(s)}_{\lambda',\lambda'',i} := \mathrm{r}_i^{(C)} + \sqrt{\frac{m_i^{(\lambda')}}{m_i^{(\lambda'')}}} (\mathrm{r}_i^{(s)} - \mathrm{r}_i^{(C)}). \tag{2.19}$$

2. Accept the trial move with a probability

$$\min\left[1, \left(\prod_{i=1}^{N} \frac{m_i^{(\lambda'')}}{m_i^{(\lambda')}}\right)^{D/2} \exp\left\{\frac{\beta}{P} \sum_{s=1}^{P} [V(\mathbf{r}^{(s)}) - V(\mathbf{r}^{(s)}_{\lambda',\lambda''})]\right\}\right]. \tag{2.20}$$

When discussing Monte Carlo moves with respect to λ, we shall refer the procedure defined by Eqs. (2.12)-(2.16) as the "simple λ-move", and to that of Eqs. (2.17)-(2.20) as the "mass-scaled λ-move". If the centroid probability distribution starts to vary too much over $\lambda \in [0, 1]$, the acceptance probability for the mass-scaled λ-move can become too low; this is solved easily by restricting the trial λ'' value to a smaller interval $[\lambda' - \Delta\lambda_{\max}, \lambda' + \Delta\lambda_{\max}]$ using the procedure of Eqs. (2.12)-(2.15). [Yet, for all systems considered in this work, Eqs. (2.17)-(2.20) led to sufficiently high acceptance probability without this modification.] The main advantage of the mass-scaled λ-move is that its acceptance probability does not depend on P. Its disadvantage is its requirement of P evaluations of V, which makes it much more expensive than the simple λ-move. Nonetheless, as will be demonstrated in Sec. 2.3, an occasional use of mass-scaled λ-moves can, in fact, accelerate convergence with respect to λ.

The Monte Carlo procedure has one last shortcoming: Since the probability of finding the system with $\lambda = \lambda'$ is proportional to $Q^{(\lambda')}$, for very large isotope effects (the largest isotope effect computed in this work was $\sim 10^8$) most of the samples would be taken in the region close to $\lambda = 0$, which would introduce a huge statistical error. This problem can be solved by adding a biasing umbrella potential $U_b(\lambda)$, resulting in a biased probability density

$$\rho_b^{(\lambda)}(\{\mathbf{r}^{(s)}\}) = \rho^{(\lambda)}(\{\mathbf{r}^{(s)}\}) \exp[-\beta U_b(\lambda)]. \tag{2.21}$$

In the case of a free particle, all trial moves defined by Eqs. (2.17)-(2.19) will be accepted provided that the optimal biasing potential

$$U_{b,\text{free}}(\lambda) = \frac{D}{2\beta} \sum_{i=1}^{N} \ln[m_i^{(\lambda)}/m_i^{(0)}] \tag{2.22}$$

is chosen; in other words, if $V \equiv 0$, then including $U_{b,\text{free}}(\lambda)$ in the acceptance probability (2.20) will make it unity.

With this final modification in place, the proposed method can be summarized as running a Monte Carlo simulation in the augmented configuration space and then evaluating the isotope effect with the formula

$$\frac{Q_P^{(B)}}{Q_P^{(A)}} = \lim_{J\to\infty} \exp\left\{-\frac{\beta}{J}\sum_{j=1}^{J} \langle [dF(\lambda)/d\lambda]_{\text{cv}}\rangle^{I_j}\right\}, \tag{2.23}$$

where $\langle \cdots \rangle^{I_j}$ is an average over all $\lambda \in I_j$. The integration error associated with having a finite number J of λ intervals depends strongly on the choice of the umbrella potential $U_b(\lambda)$. As we prove in Appendix B, this error is exactly zero for a piecewise linear umbrella potential satisfying

$$\frac{dU_b(\lambda)}{d\lambda} = -\langle [dF(\lambda)/d\lambda]_{\text{cv}}\rangle^{I_j} \text{ for all } \lambda \in I_j. \tag{2.24}$$

It is also clear that the resulting $U_b(\lambda)$ will follow fairly closely the ideal biasing potential $\beta^{-1} \ln Q^{(\lambda)}$, and therefore the estimator samples will be distributed more or less equally among different intervals I_j, which, in turn, will minimize the statistical error of Eq. (2.23).

It is obvious that in general systems, $U_b(\lambda)$ from Eq. (2.24) cannot be known *a priori*. As this is typical for biased simulations, numerous methods, including adaptive umbrella sampling [133–135], metadynamics [136, 137], and adaptive biasing force method [130, 131], have been introduced to solve this problem. In our calculations, the biasing potential $U_b(\lambda)$ was obtained from a short simulation employing the adaptive biasing force method. The resulting $U_b(\lambda)$ was then used in a longer simulation in which the isotope effect itself was evaluated.

2.3 Numerical examples

In this section the proposed stochastic procedure for evaluating isotope effects is tested on a model harmonic system and on deuteration of methane. The results of the new approach are compared with results of the usual thermodynamic integration and with the analytical result for the harmonic system. From now on, for brevity we will refer to the traditional thermodynamic integration with respect to mass (Subsec. 2.2.1) simply as "thermodynamic integration" (TI), and to the thermodynamic integration with stochastic change of mass (Subsec. 2.2.2) as "stochastic thermodynamic integration" (STI). In all cases, we compare STI with TI both for the linear [Eq. (2.3)] and the more efficient [Eq. (2.4)] interpolation of mass.

2.3.1 Computational details

As mentioned in Sec. 2.2, the λ interval $[0,1]$ was divided into J subintervals $I_j = [\lambda_{j-1}, \lambda_j]$ $(j = 1, \ldots, J)$ with $\lambda_j = j/J$ $(j = 0, \ldots, J)$. The TI used, in addition, a reference point $\bar{\lambda}_j$ from each interval, which was always taken to be the midpoint $\bar{\lambda}_j = (j - 1/2)/J \in I_j$. This midpoint was used for evaluating the thermodynamic integral with the midpoint rule as

$$\int_0^1 \frac{d \ln Q^{(\lambda)}}{d\lambda} d\lambda = \frac{1}{J} \sum_{j=1}^{J} \left. \frac{d \ln Q^{(\lambda)}}{d\lambda} \right|_{\lambda=\bar{\lambda}_j} + \mathcal{O}\left(J^{-2}\right). \tag{2.25}$$

(Assuming that each logarithmic derivative is obtained with the same statistical error, this choice of $\bar{\lambda}_j$'s and integration scheme minimizes the statistical error of the logarithm of the calculated isotope effect.) To estimate the integration error of TI and to verify that the integration error of STI is zero, we compared the calculated isotope effects with the exact analytical [138] values for the harmonic system with a finite Trotter number P and with the result of STI using a high value of $J = 8192$ for the deuteration of methane.

The second type of error is the statistical error inherent to all Monte Carlo methods; this error was evaluated with the "block-averaging" method [139] for correlated samples, which was applied directly to the computed isotope effects instead of, e.g., the free energy derivatives, thus avoiding the tedious error propagation. Since the average isotope effect depends on the block size, one has to make sure not only that the statistical error reaches a plateau, but also that the average reaches an asymptotic value as a function of the block size.

The third type of error is the Boltzmann operator discretization error due to a finite value of P; for harmonic systems it is available analytically [138], while for the CD_4/CH_4 isotope effect we made sure that it was below 1% by repeating the calculations for the lowest and highest temperatures with twice larger P.

2.3.2 Isotope effects in a harmonic model

A harmonic system was used as the first, benchmark test of the different approaches to compute the isotope effects, since most properties of a harmonic system can be computed exactly analytically. To simulate a realistic system with a range of vibrational frequencies, we used an eight-dimensional harmonic system with frequencies

$$\omega_q = \omega_0 \times 2^{-q/2} \quad (q = 0, \ldots, 7). \tag{2.26}$$

The computed isotope effect corresponded to doubling masses of all normal modes, and therefore to reducing each ω_q by a factor of $\sqrt{2}$.

Computational details

To analyze the dependence of the computed isotope effect on the number J of λ intervals used in different methods, we first ran several calculations with $\beta\hbar\omega_0 = 8$. Then we investigated the behavior of the different methods at several temperatures and hence for dramatically different isotope effects, by taking $\beta\hbar\omega_0 \in \{1, 2, 4, 8, 16, 32\}$ (here we used $J = 8$ for TI and $J = 4096$ for STI). For each ω_0 the Trotter number P was taken to be $12 \times \beta\hbar\omega_0$, the resulting discretization error of the isotope effect (i.e., not of its logarithm) was always below 1%.

To explore the ring polymer coordinates $\{\mathbf{r}^{(s)}\}$, we used the normal mode path integral Monte Carlo method [88, 140], which in a harmonic model allows to generate uncorrelated samples with no rejected Monte Carlo steps. This method involves rewriting $\Phi(\{\mathbf{r}^{(s)}\})$ in terms of normal modes of the ring polymer (see Appendix A), thus transforming $\rho(\{\mathbf{r}^{(s)}\})$ into a product of Gaussians that can be sampled exactly. In all TI calculations the total number of Monte Carlo steps was $2^{25} \approx 3.4 \times 10^7$. In all STI calculations we used a mixture of $9 \times 2^{22} \approx 3.7 \times 10^7$ Monte Carlo moves with respect to $\{\mathbf{r}^{(s)}\}$, $2^{22} \approx 4.2 \times 10^6$ mass-scaled λ-moves, and $5 \times 2^{23} \approx 4.2 \times 10^7$ simple λ-moves with $\Delta\lambda_{\max} = 0.1$; first 20% of a STI calculation were used only to obtain the biasing potential $U_b(\lambda)$, but not for evaluating the isotope effect. Note that the unequal numbers of Monte Carlo steps used in TI and STI result in a fair comparison of the two methods; the simple λ-moves are almost free in terms of computational effort, and, due to warmup, the total number of the other Monte Carlo moves for STI is 20% larger than for TI, which is not an issue, since generally (i.e., in anharmonic systems in which the sampling procedure would generate correlated samples) one would need to discard a certain warmup period also in TI calculations.

Results and discussion

The numerical results are presented in Fig. 2.2. Panel (a) of the figure shows that analytical values of the isotope effect (at a finite value of P) are reproduced accurately by STI for several values of $\beta\hbar\omega_0$, confirming that the proposed Monte Carlo procedure, which changes stochastically not only coordinates but also masses of the atoms, is correct.

Panel (b) displays the integration error dependence on temperature, and confirms that this error is decreased both by linearly interpolating the inverse square roots of the masses instead of the masses themselves, and by performing the thermodynamic integration stochastically. The fact that the stochastic change of mass can eliminate the thermodynamic integration error is the main result of this paper. As the figure shows, this happens regardless of the type of interpolation used. Note that at high temperatures, the improved interpolation does not prevent TI from exhibiting a certain integration error, an issue that does not occur for STI. The statistical error dependence on temperature, depicted in panel (c), is a reminder of the well-known importance of using the centroid virial instead of the thermodynamic estimator in efficient calculations. In the harmonic system, which can be sampled exactly, the statistical errors of STI and TI are comparable.

Panels (d) and (e) of Fig. 2.2 display the dependence of integration and statistical errors of different methods on the number J of integration subintervals for $\beta\hbar\omega_0 = 8$. For TI one can clearly see the $J \to \infty$ limit where integration error becomes zero and statistical error approaches a plateau. Note that the integration error [panels (b) and (d)] does not depend on the estimator, which provides an additional check of the implementation. The centroid virial estimator significantly lowers the statistical error and using the square root of mass interpolation given by Eq. (2.4) instead of linear interpolation [Eq. (2.3)] significantly decreases the integration error. As expected, STI exhibits an error which is only due to statistical factors. Here the TI and STI exhibit similar behavior in the $J \to \infty$ limit, namely the integration error is zero and the statistical error approaches a limit which is comparable for both methods. However, in this system the limit $J \to \infty$ was achievable for TI because the normal mode path integral Monte Carlo procedure used for exploring $\{\mathbf{r}^{(s)}\}$ generated uncorrelated samples; reaching $J \to \infty$ would be more difficult in more realistic, anharmonic systems, where even the TI procedure requires correlated sampling. Yet, as will be shown below on methane, large values of J can be used easily in STI calculations. Also note that the statistical error of STI decreases with J and approaches its limit faster when the square root of mass interpolation [Eq. (2.4)] is used. This behavior is expected as the statistical error of $\langle [dF(\lambda)/d\lambda]_{\mathrm{cv}} \rangle^{I_j}$ from Eq. (2.23) is partly due to a variation of the average $\langle [dF(\lambda)/d\lambda]_{\mathrm{cv}} \rangle^{(\lambda)}$ over $\lambda \in I_j$; the resulting contribution to the statistical error of the isotope effect is reduced by increasing J or using an improved mass interpolation function that makes $\langle [dF(\lambda)/d\lambda]_{\mathrm{cv}} \rangle^{(\lambda)}$ flatter over each I_j.

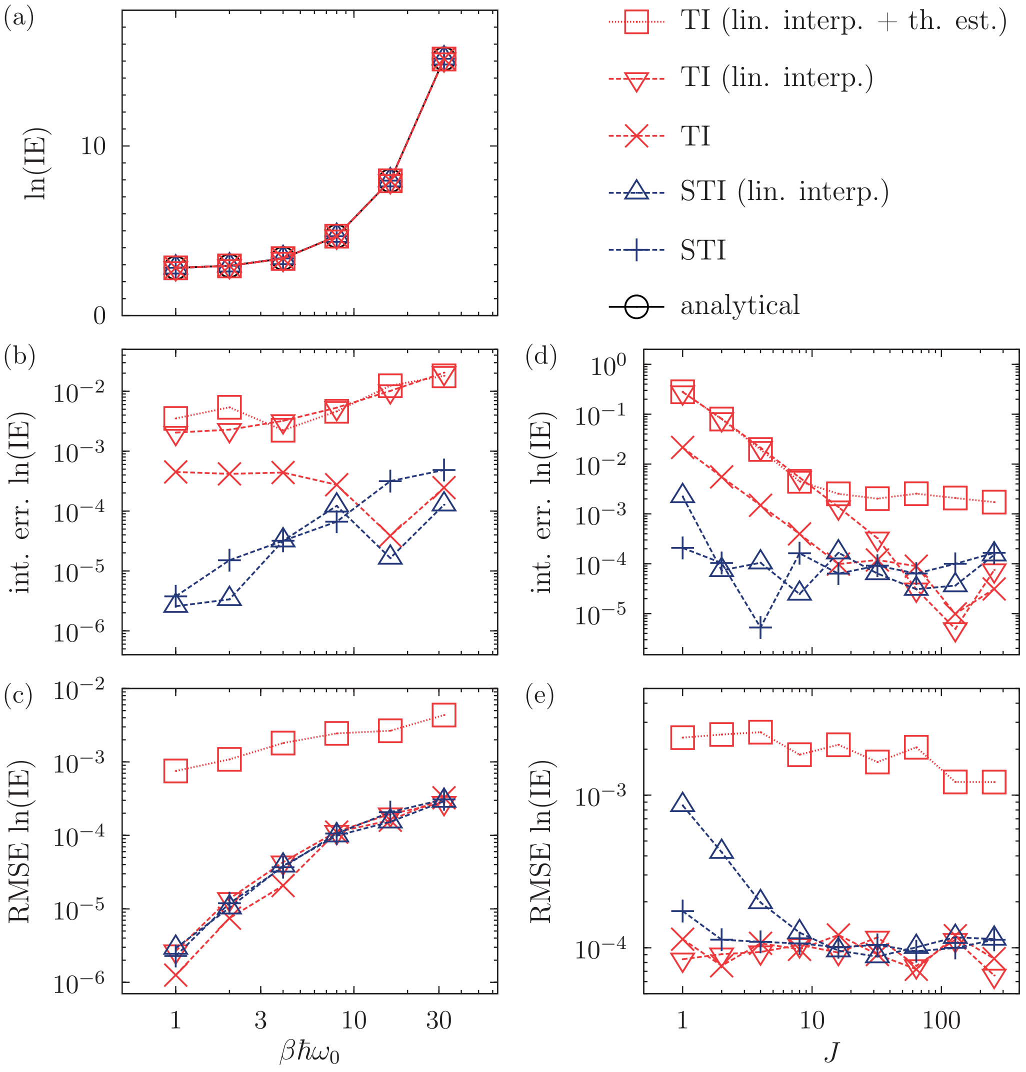

Figure 2.2: Isotope effect (IE) calculations in an eight-dimensional harmonic model from Subsec. 2.3.2. Unless explicitly stated in the label, all results use the centroid virial estimator (2.8) and improved mass interpolation (2.4). Results labeled “lin. interp.” use linear interpolation (2.3) and those labeled “th. est.” the thermodynamic estimator (2.7). Several versions of thermodynamic integration (TI) are compared with exact analytical values (for the same finite Trotter number P). The proposed method is “stochastic thermodynamics integration” (STI). Panels (a)-(c) show the temperature dependence of (a) the isotope effect, (b) its integration errors, and (c) its statistical root mean square errors (RMSEs). Panels (d)-(e) display the dependence of integration errors and RMSEs on the number J of integration subintervals at a temperature given by $\beta\hbar\omega_0 = 8$.

2.3.3 Deuteration of methane

Computational details

The methane calculations used the potential energy surface from Ref. [141] and available in the POTLIB library [142]. The force field is the product of least square fitting of an ansatz to *ab initio* data; the ansatz was written in terms of coordinates based on five-atom Radau coordinates [143], guaranteeing its invariance with respect to hydrogen atom permutations. The number of λ integration intervals was $J = 4$ for TI and $J = 4096$ for STI.

TI calculations used a total of 2×10^8 Monte Carlo steps which sampled $\{\mathbf{r}^{(s)}\}$, for STI the number of $\{\mathbf{r}^{(s)}\}$ Monte Carlo steps was 1.8×10^8; in both cases 14% were whole-chain moves and 86% were multi-slice moves performed on one sixth of the chain with the staging algorithm [144, 145] (this guaranteed that approximately the same computer time was spent on either of the two types of moves). For STI we additionally used 0.2×10^8 mass-scaled λ-moves and 2×10^8 simple λ-moves with $\Delta\lambda_{\max} = 0.1$. As the simple λ-moves are almost free in terms of computational time, the cost of both calculations was still roughly the same. To avoid the unnecessary cost of evaluating correlated samples, all virial estimators were evaluated only after every ten Monte Carlo steps for TI and after every twenty Monte Carlo steps for STI (since STI calculations had twice as many Monte Carlo steps the number of virial estimator samples was still the same), while thermodynamic estimators were evaluated after each step since the computational time required for their calculation is negligible. The first 20% Monte Carlo steps of each calculation were discarded as “warmup”; as discussed in Subsec. 2.3.1, in the simulations employing the stochastic change of mass, the same warmup period was also used to generate the biasing potential $U_b(\lambda)$ needed for the rest of the calculation. The path integral discretization error, estimated by running simulations with a twice larger P at the highest and lowest temperatures ($T = 1000\,\mathrm{K}$ and $T = 200\,\mathrm{K}$), was below 1%; for other temperatures P was obtained by linear interpolation with respect to $1/T$.

Of course, in practice much shorter simulations would be sufficient, but we used over-converged calculations in order to analyze the behavior of different types of errors in detail.

Results and discussion

The results of the calculations of the CD_4/CH_4 isotope effect are presented in Fig. 2.3. Panel (a) shows that the isotope effects calculated with the different methods agree. Yet, a more detailed inspection reveals the improvement provided by the STI compared with the TI. This is done in panel (b), showing the integration errors of the different methods; the STI result with a twice larger value of J (i.e., $J = 8192$) is considered as an exact benchmark. In the case of TI the integration error depends strongly on the type of mass interpolation: If the linear interpolation is used, the integration error is even much larger than the statistical error [see panel (c)], while, for this particular system, the improved

Table 2.1: Values of the CD_4/CH_4 isotope effect (IE) obtained with several versions of thermodynamic integration (TI). Corresponding statistical errors are shown as well. Unless explicitly stated in the label, all results use the centroid virial estimator (2.8) and improved mass interpolation (2.4). The proposed methodology is stochastic thermodynamic integration (STI).

T	P	ln(IE) (CD_4/CH_4) with statistical error				
		TI (lin. interp. + thermod. est.)	TI (lin. interp.)	TI	STI (lin. interp.)	STI
200	360	19.67 ± 0.02	19.683 ± 0.002	19.785 ± 0.002	19.783 ± 0.002	19.789 ± 0.002
300	226	13.61 ± 0.01	13.602 ± 0.001	13.671 ± 0.002	13.676 ± 0.001	13.673 ± 0.002
400	158	10.61 ± 0.01	10.612 ± 0.001	10.665 ± 0.001	10.666 ± 0.001	10.667 ± 0.001
500	118	8.876 ± 0.005	8.866 ± 0.001	8.908 ± 0.001	8.910 ± 0.001	8.910 ± 0.001
600	90	7.740 ± 0.003	7.743 ± 0.001	7.778 ± 0.001	7.779 ± 0.001	7.779 ± 0.001
700	72	6.977 ± 0.003	6.974 ± 0.001	7.004 ± 0.001	7.006 ± 0.001	7.006 ± 0.001
800	58	6.413 ± 0.003	6.423 ± 0.001	6.449 ± 0.001	6.451 ± 0.001	6.451 ± 0.001
900	46	6.020 ± 0.003	6.013 ± 0.001	6.037 ± 0.001	6.039 ± 0.001	6.039 ± 0.001
1000	36	5.703 ± 0.003	5.702 ± 0.001	5.723 ± 0.001	5.725 ± 0.001	5.726 ± 0.001

interpolation (2.4) of the inverse square root of mass allows to obtain quite accurate results, even though a small integration error remains visible above the statistical noise at higher temperatures. In the case of the STI, on the other hand, no integration error is observed, which was one of the main goals of this work. Finally, panel (c) shows that if the same estimator is used the STI exhibits comparable statistical errors to those of TI, which confirms that employing the STI can easily lower the integration errors without increasing the computational cost.

For reference, the plotted values together with their statistical errors are listed in Table 2.1. From this table it is clear that STI calculations with both types of mass interpolation agree within their statistical errors, while TI, particularly with linear interpolation, retains a significant integration error.

To better understand the benefit of the STI, recall that stopping a Monte Carlo simulation after obtaining only a finite number of samples introduces two types of errors. The first is the statistical error, which has been analyzed in all calculations so far; the second type is a systematic error, and appears if the sampling procedure yields correlated samples and Monte Carlo trajectories are too short to guarantee ergodicity. This systematic error has not appeared yet since all our calculations were too well converged; however, it becomes important when computational resources are limited, and therefore deserves additional consideration. Indeed, one of the main motivations behind this work was the expectation that equilibrating a single STI simulation should consume fewer computational resources than equilibrating J simulations required in a standard TI calculation. To illustrate this point we ran several much less converged calculations of the CD_4/CH_4 isotope effect at $T = 200$ K. The number of Monte Carlo steps used during the simulations was doubled from one calculation to the next; for example, for TI there were $1280, 2560, ..., 1310720$ Monte Carlo steps partitioned in the same way as for the more converged calculations.

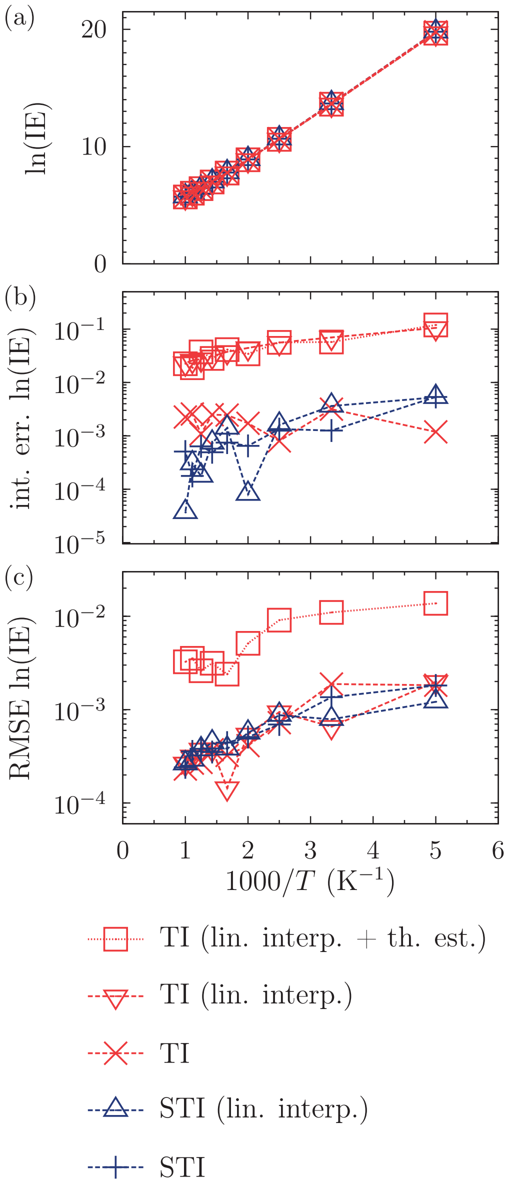

Figure 2.3: Calculations of the CD_4/CH_4 isotope effect (IE) from Subsec. 2.3.3. Labels are explained in the caption of Fig. 2.2. The three panels show the temperature dependence of (a) the isotope effect, (b) its integration errors, and (c) its statistical root mean square errors (RMSEs).

The only difference was that this time no part of the simulation was discarded as warmup. Moreover, to be sure that the error observed for smaller numbers of Monte Carlo steps is the systematic error due to non-ergodicity and not the “true” statistical error, the value obtained with 1280 Monte Carlo steps was averaged over 4096 independent calculations, 2560 - over 2048 calculations, etc.; this averaging ensured that each result had roughly the same statistical error. The STI calculations were performed with or without the mass-scaled λ-moves and with or without the simple λ-moves to compare the efficiency of the resulting methods.

Isotope effects obtained with these much cheaper calculations are compared in Fig. 2.4, where the converged STI result $\ln \mathrm{IE} = 19.789$ from Fig. 2.3 and Table 2.1 serves as the exact reference; for a completely fair comparison the results are plotted as a function of the number of potential energy evaluations required to obtain them. As expected, the results of shorter simulations exhibit a significant error due to non-ergodicity of underlying simulations, yet this nonergodicity error is much smaller for the proposed STI than for the TI, making the STI more practical in situations where computational resources are limited. Even though the mass-scaled λ-moves are quite expensive, their addition accelerates the convergence of the integral. The much cheaper simple λ-moves appear to also contribute to convergence, as the results obtained without them are not as well converged as results with both types of λ-moves.

2.4 Conclusions

We have introduced a new Monte Carlo procedure that involves changing atomic masses stochastically during the simulation and allows to eliminate the integration error of thermodynamic integration, thus significantly speeding up isotope effect calculations. The proposed methodology relies on a set of new tools: One of these tools is the introduction of mass-scaled λ-moves that permit drastic changes of λ in a single Monte Carlo step; as shown in Subsec. 2.3.3 their addition can significantly contribute to the convergence of the thermodynamic integral. Another tool is the piecewise linear umbrella biasing potential $U_b(\lambda)$ that guarantees a zero integration error of the thermodynamic integral for any number J of integration subintervals; this trick is general and can be used regardless of the type of free energy change one may want to evaluate.

It is possible, as in metadynamics, to facilitate convergence with respect to λ by additionally biasing the simulation with a history-dependent potential that pushes the system into less explored regions of configuration space; this addition can become important if the change of isotope masses $m_i^{(\lambda)}$ is so drastic that one has to impose an upper bound $\Delta\lambda_{\max}$ for the change of λ in a single step even for the mass-scaled λ-moves. However, this did not occur in systems considered in this work, where mass-scaled λ-moves yielded acceptance probabilities above 70% in all calculations. As a result, the mass-scaled λ-moves allowed large changes of λ in a single step, leading to a fast convergence over the λ dimension without additional modifications of the Monte Carlo procedure.

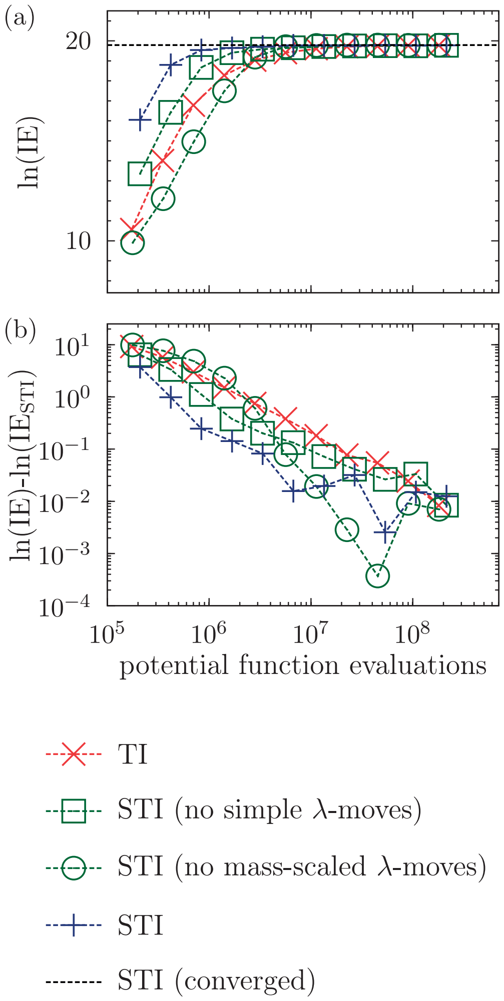

Figure 2.4: The impact of nonergodicity appearing in shorter calculations of the CD_4/CH_4 isotope effect (IE) at $T = 200$ K. Panel (a) presents the convergence of the IE as a function of the simulation length, while panel (b) shows the corresponding error of the IE (in logarithmic scale) relative to a converged STI result. Labels TI and STI are as in the caption of Fig. 2.2; "STI (no simple λ-moves)" were obtained without the simple λ-moves defined by Eqs. (2.12)-(2.16), while "STI (no mass-scaled λ-moves)" were obtained without mass-scaled λ-moves defined by Eqs. (2.17)-(2.20). The horizontal line in panel (a) labeled "STI (converged)" is the converged STI result $\ln(\mathrm{IE}_{\mathrm{STI}}) = 19.789$ from Fig. 2.3 and Table 2.1; the same value was used as a reference in panel (b).

In this work we relied heavily on the fact that λ values can be sampled without repercussions even if they are placed far away from the endpoints $\lambda = 0$ and $\lambda = 1$ that correspond to physically meaningful systems. This is true for isotope effects, as also found in Ref. [93], but may not be so for other calculations of free energy differences. As a result, several variants of λ-dynamics bias the sampling of λ towards the endpoints, and then calculate the free energy difference from the ratio of probability densities at $\lambda = 0$ and $\lambda = 1$ [98, 99]. Indeed, our STI approach would also allow obtaining a well converged result by sampling mainly in the regions of λ close to the endpoints $\lambda = 0$ and $\lambda = 1$ if one used a modified partition function

$$\tilde{Q}^{(\lambda)} = Q^{(\lambda)} e^{-\beta V_{\mathrm{barr}}(\lambda)}, \tag{2.27}$$

where $V_{\mathrm{barr}}(\lambda)$ is a potential that biases the Monte Carlo chain towards the end points. Running an STI calculation with $J = 1$ will lead to an exact partition function ratio and at the same time use mainly samples from values of λ close to the endpoints. Although such an approach would avoid the problem of choosing an optimal bin width for the weighted histogram analysis method (WHAM), an issue discussed in Ref. [100], it would, just as WHAM, require equilibration over the entire λ interval $[0, 1]$ instead of only over each subinterval I_j, which would make it less convenient than the simple STI presented.

We conclude this chapter by noting that the stochastic thermodynamic integration can be combined with Takahashi-Imada or Suzuki fourth-order factorizations [79–82] of the Boltzmann operator, which would allow lowering the path integral discretization error of the computed isotope effect for a given Trotter number P, and hence a faster convergence to the quantum limit. The combination of higher-order path integral splittings with standard thermodynamic integration has been discussed elsewhere [83, 115–117]; as for the extension to stochastic thermodynamic integration, the main additional change consists in replacing the potential V in the acceptance probability in Eq. (2.20) with an effective potential depending on mass and, in the case of the fourth-order Suzuki splitting, in an additional factor depending on the imaginary time-slice index s.

3 Improving equilibrium isotope effect calculations with direct estimators

3.1 Introduction

The results of this work are contained in Ref. [146].

In the previous chapter, we discussed integration error of thermodynamic integration and how it can be eliminated by changing particles' masses during the simulation and choosing an appropriate biasing potential. This goal, however, can be achieved with another method that avoids introducing an integration error altogether by using the so-called "direct estimators" for equilibrium isotope effects [1], this approach can be regarded as a free energy perturbation technique [94–96, 147] optimized for equilibrium isotope effect calculations. Unfortunately, as mentioned in Subsec. 1.5.2, free energy perturbation methods work best for smaller changes of the free energy, causing the original approach of Ref. [1] to exhibit a statistical error which grows with the magnitude of the equilibrium isotope effect. Obviously, the problem can be bypassed if the isotope effect (1.2) is partitioned into several smaller "intermediate" isotope effects which can be easily calculated with direct estimators; the resulting "stepwise" approach will be similar to thermodynamic integration as it will also involve a certain discretization with respect to mass. The method can be further improved after recalling that changing λ during the simulation improves statistical convergence of thermodynamic integration, as was already discussed in the previous chapter; it is therefore natural to investigate whether a "stepwise" implementation of direct estimators would benefit from changing mass during the simulation as well. It is necessary to note that such a combination with direct estimators is only possible for a mass sampling procedure that allows finite steps with respect to mass; this makes the Monte Carlo procedure described in the previous chapter suitable for the task, but disqualifies the more common λ-dynamics algorithms based on molecular dynamics.

As in the previous chapter, we will test numerical performance of the proposed methodology on an eight-dimensional harmonic model and in a full-dimensional $\mathrm{CH_4}$ molecule. This time, however, for $\mathrm{CH_4}$ we will calculate not only the large $\mathrm{CD_4/CH_4}$ isotope effect, but also all $\mathrm{CH_{4-x}D_x/CH_4}$ isotope effects ($x = 1, \ldots, 4$).

3.2 Theory

3.2.1 Free energy perturbation and direct estimators for equilibrium isotope effects

Free energy perturbation method for calculating free energy differences was already mentioned in Subsec. 1.5.2 and for the case of change of mass will take the form

$$\frac{Q_P^{(1)}}{Q_P^{(0)}} = \frac{\int \rho^{(1)}(\{\mathbf{r}^{(s)}\})d\{\mathbf{r}^{(s)}\}}{\int \rho^{(0)}(\{\mathbf{r}^{(s)}\})d\{\mathbf{r}^{(s)}\}} = \frac{\int \mathcal{Z}^{0,1}\rho^{(0)}(\{\mathbf{r}^{(s)}\})d\{\mathbf{r}^{(s)}\}}{\int \rho^{(0)}(\{\mathbf{r}^{(s)}\})d\{\mathbf{r}^{(s)}\}} = \left\langle \mathcal{Z}^{0,1} \right\rangle^{(0)}, \tag{3.1}$$

where we introduced a direct estimator for the isotope effect $\mathcal{Z}^{0,1} := \rho^{(1)}(\{\mathbf{r}^{(s)}\})/\rho^{(0)}(\{\mathbf{r}^{(s)}\})$. Straightforward substitution of $\rho(\{\mathbf{r}^{(s)}\})$ (1.35) leads to the so-called "thermodynamic direct estimator" for an isotope effect [1, 93]

$$\mathcal{Z}_{\text{th}}^{0,1} = \left[\prod_{i=1}^{N} \frac{m_i^{(1)}}{m_i^{(0)}}\right]^{DP/2} \exp\left(\frac{P}{2\beta\hbar^2}\sum_{i=1}^{N}\left\{[m_i^{(0)} - m_i^{(1)}]\sum_{s=1}^{P}|\mathrm{r}_i^{(s)} - \mathrm{r}_i^{(s-1)}|^2\right\}\right). \tag{3.2}$$

Statistical error of this estimator grows with P due to reasons similar to the ones discussed for the thermodynamic estimator for the logarithmic derivative $[dF(\lambda)/d\lambda]_{\text{th}}$. The issue is avoided if the so-called mass-scaled direct estimator [1] is used

$$\mathcal{Z}_{\text{sc}}^{0,1} = \left[\prod_{i=1}^{N} \frac{m_i^{(1)}}{m_i^{(0)}}\right]^{D/2} \exp\left\{\frac{\beta}{P}\sum_{s=1}^{P}\left[V(\mathbf{r}^{(s)}) - V(\mathbf{r}_{0,1}^{(s)})\right]\right\}. \tag{3.3}$$

This estimator can be easily derived using the mass-scaled normal mode coordinates $\{\mathbf{u}^{(s)}\}$ which were discussed in Appendix A; namely one has to rewrite $Q^{(0)}$ and $Q^{(1)}$ in Eq. (3.1) in terms of $\{\mathbf{u}^{(s)}\}$. This leads to a direct estimator which equals $\tilde{\rho}^{(1)}(\{\mathbf{u}^{(s)}\})/\tilde{\rho}^{(0)}(\{\mathbf{u}^{(s)}\})$, leading to Eq. (3.3) once one goes back to standard Cartesian coordinates $\{\mathbf{r}^{(s)}\}$.

3.2.2 Stepwise implementation of the direct estimators

We mentioned in Sec. 1.5 that free energy perturbation methods work best if $\rho^{(0)}(\{\mathbf{r}^{(s)}\})$ and $\rho^{(1)}(\{\mathbf{r}^{(s)}\})$ are close to each other; as a result for isotope effects of greater magnitude both $\mathcal{Z}_{\text{th}}^{0,1}$ and $\mathcal{Z}_{\text{sc}}^{0,1}$ yield larger statistical errors. A straightforward way to bypass the issue is performing the calculation stepwise by factoring the large isotope effect into several smaller isotope effects between virtual isotopologues. For that purpose, one can, analogously to thermodynamic integration, introduce a set of $J + 1$ intermediate values λ_j ($j = 0, \ldots, J$)

such that $\lambda_0 = 0$, $\lambda_J = 1$, and write [93, 148]

$$\frac{Q^{(1)}}{Q^{(0)}} = \prod_{j=1}^{J} \frac{Q^{(\lambda_j)}}{Q^{(\lambda_{j-1})}}. \tag{3.4}$$

For J large enough, $Q^{(\lambda_j)}/Q^{(\lambda_{j-1})}$ will be sufficiently close to unity, and hence can be evaluated with direct estimators. It will prove useful to write Eq. (3.4), expressed in terms of direct estimator averages, in a more general manner as

$$\frac{Q_P^{(1)}}{Q_P^{(0)}} = \prod_{j=1}^{J} \frac{\langle \mathcal{Z}_{\mathrm{sc}}^{\overline{\lambda}_j,\lambda_j} \rangle^{(\overline{\lambda}_j)}}{\langle \mathcal{Z}_{\mathrm{sc}}^{\overline{\lambda}_j,\lambda_{j-1}} \rangle^{(\overline{\lambda}_j)}}, \tag{3.5}$$

by using an arbitrary $\overline{\lambda}_j$ from the interval $I_j = [\lambda_{j-1}, \lambda_j]$ as the λ-value of the sampling weight used in the jth factor of the isotope effect. In numerical calculations, however, we always used intervals of equal size (i.e., $\lambda_j = j/J$ for $j = 0, \ldots, J$) and midpoints $\overline{\lambda}_j = (j - 1/2)/J$ ($j = 1, \ldots, J$) of those intervals, in agreement with the notation introduced above for thermodynamic integration.

In what follows, we will sometimes refer to the just described stepwise application of direct estimators, which is only a slight generalization of the original method [1] of direct estimators, simply as “direct estimators.”

3.2.3 Combining direct estimators with the stochastic change of mass

There are several reasons it seems advantageous to combine the stepwise direct estimators approach with the stochastic change procedure discussed in the previous chapter. The first argument is completely analogous to the one presented in Subsec. 2.2.2, namely that it takes less computational resources to converge one Monte Carlo simulation rather than J simulations; therefore it is computationally cheaper to obtain a converged result from Eq. (3.5) if all the factors in the right hand side are obtained from one simulation rather than J separate simulations. The second argument is that the original implementation of direct estimators made it possible to calculate several equilibrium isotope effects with one simulation by calculating the average of several direct estimators at once; this would be no longer possible if each factor of Eq. (3.5) is obtained with a separate simulation. Last but not the least, the stochastic change of λ can lead to a decrease of statistical error of the calculated equilibrium isotope effect. Consider J sets of correlated samples obtained from J independent simulations using the method of direct estimators and run at different values of $\overline{\lambda}_j$; reshuffling the samples between simulations should make samples inside each simulation less correlated between each other, thus lowering statistical error of averages obtained from them. The proposed method can be regarded as such a “shuffling,” and in this respect it resembles the parallel tempering or replica exchange Markov chain Monte Carlo techniques [122–124], but for the latter approaches the value of J that can be used in practice will depend on the number of simulation replicas one can run simultaneously.

With this motivation in mind, it is easy to see that to change λ value between different $\overline{\lambda}_j$ values one can use the same procedure as that described in Subsec. 2.2.2, the only difference being that the trial λ value should be restricted to a discrete set of values $\{\overline{\lambda}_j\}$, $j = 1, \ldots, J$; some more tedious details are found in Appendix C. The overall isotope effect is again obtained from Eq. (3.5).

3.3 Numerical examples

To test the two proposed procedures (i.e., stepwise and stochastic implementation of the direct estimators) for evaluating isotope effects, we applied them to a model harmonic system and to several isotopologues of methane. In addition we compared the results of the new approaches with results of the thermodynamic integration with either deterministic or stochastic change of mass, and with the original method of direct estimators [1]. From now on, for brevity we will refer to the five methods as follows: thermodynamic integration with respect to mass (Subsec. 2.2.1) will be simply referred to as "thermodynamic integration" (TI), thermodynamic integration with stochastic change of mass (Subsec. 2.2.2) as "stochastic thermodynamic integration" (STI), Cheng and Ceriotti's method of direct estimators (Subsec. 3.2.1) as "original direct estimators" (ODE), stepwise application of direct estimators (Subsec. 3.2.2) as "direct estimators" (DE), and stepwise application of direct estimators with stochastic change of mass (Subsec. 3.2.3) as "stochastic direct estimators" (SDE).

3.3.1 Computational details

The calculations presented in this Section were done with parameters mostly identical to the ones already described in the previous chapter, namely Sec. 2.3. For TI and STI calculations the only difference is that for CD_4/CH_4 a different mass switching function $m_i^{(\lambda)}$ was used to allow calculating all isotope effects of the form $CH_{3-x}D_{x+1}/CH_{4-x}D_x$ with $x = 0, 1, 2, 3$, it is described in detail in Subsubsec. 3.3.3. DE and SDE calculations were done with the same number of steps and frequency of estimators' evaluation as TI and STI respectively; for SDE we additionally modified simple λ-moves used in STI calculations in a way described in Appendix C. For ODE, the total number of different Monte Carlo steps was again the same as for TI, as was the frequency of estimators' evaluation; for methane we calculated direct estimators corresponding to all ratios of the form $CH_{3-x}D_{x+1}/CH_4$ with $x = 0, 1, 2, 3$, while for the harmonic system we only calculated the direct estimator corresponding to the total equilibrium isotope effect. Path integral simulations used in ODE always corresponded to the isotopologue with the smallest atom masses. The way the λ interval was divided into subintervals was also the same as in Sec. 2.3.

As discussed in Sec. 2.2, results obtained with TI contain integration error; it was estimated by comparing the calculated isotope effects with the exact analytical [138] values for a harmonic system with a finite Trotter number P and with the result of SDE for methane. (Recall that ODE, DE, and SDE have no integration error by definition, while for STI the absence of integration error for a proper choice of biasing potential was proven in Appendix B; in any case the integration error is basically transformed into a statistical error.) Statistical errors were evaluated with the "block-averaging" method [139] for correlated samples the same way as in Sec. 2.3. Last but not the least, Boltzmann operator discretization error was estimated from relative analytic expressions for harmonic systems [138], while for the CD_4/CH_4 isotope effect we estimated it using a novel procedure presented in Appendix D.

3.3.2 Isotope effects in a harmonic model

The numerical results are presented in Fig. 3.1 and correspond to a harmonic system completely identical to the one used in Subsec. 2.3.2. Panel (a) of Fig. 3.1 shows that analytical values of the isotope effect (at a finite value of P) are reproduced accurately by all five methods for several values of $\beta\hbar\omega_0$, confirming, in particular, that the proposed stepwise and stochastic implementation of the direct estimators are correct.

Panel (b) of Fig. 3.1 displays dependence of thermodynamic integration error on temperature. (Remember that the integration error is zero for STI, ODE, DE, and SDE by construction). The figure is a reminder of the fact that, despite the improved mass interpolation scheme (2.4), TI is the only of the five presented methods that exhibits a significant integration error, especially noticeable at higher temperatures since the mass interpolating function Eq. (2.4) was designed to be most effective in the deep quantum regime.

Panel (c) of Fig. 3.1 compares statistical errors of the five methods considered. The first evident trend is that ODE exhibits a larger statistical error compared to the other methods, especially at lower temperatures; it illustrates the need to use DE or SDE instead in such cases. Secondly, similar statistical errors are exhibited by TI and DE, as well as STI and SDE. Here it is necessary to note that in the limit of large J TI becomes equivalent to DE and STI becomes equivalent to SDE; to see this one can recall that $[dF(\lambda)/d\lambda]_{\mathrm{est}}$ is related to the derivative of $\mathcal{Z}_{\mathrm{sc}}^{\lambda',\lambda''}$ with respect to λ'' and compare Eq. (3.5), Eq. (2.25) and Eq. (2.23). It is therefore reasonable to expect that for large values of J or small isotope effects statistical errors of TI and DE or STI and SDE will be quite close; in this case $J = 8$ is apparently enough to enforce this tendency over a wide temperature range.

Panel (d) of Fig. 3.1 displays integration error of TI as a function of the number J of λ intervals. Clearly, for TI, the integration error approaches zero only in the $J \to \infty$ limit, which can be approached in this particular case since the Monte Carlo procedure produces uncorrelated samples. Note, however, that in most practical calculations, this is impossible and the limit is unattainable.

Finally, panel (e) of Fig. 3.1 shows the dependence of statistical errors on J, demonstrating that the statistical errors of the four methods approach their limiting values for $J \to \infty$. As already mentioned earlier, similar statistical errors for TI and DE or STI and SDE in the $J \to \infty$ limit are expected. We can see that in this case, however, the tendency is already observed at surprisingly small values of J, namely $J = 1$ for TI and DE and $J = 2$ for STI and SDE.

3.3.3 Deuteration of methane

Computational details

As mentioned above, most calculation parameters used in this Subsection are identical to the ones described in Sec. 2.3.3, with appropriate modifications for DE, SDE, and ODE described in the beginning of this section; here it is sufficient to mention that the computational time spent on TI, STI, SDE, DE, and ODE calculations was approximately the same. The main difference is that the mass interpolation formula (2.4) was slightly modified in order to calculate in one simulation not only the CD_4/CH_4 isotope effect, but also all intermediate isotope effects of the form $CH_{3-x}D_{x+1}/CH_{4-x}D_x$ with $x = 0, 1, 2, 3$; this was achieved by changing, one by one, the masses of the four hydrogens to deuteriums. The inverse of the square root of the mass of the first atom was changed over the interval $\lambda \in [0, 1/4]$, of the second atom over $\lambda \in [1/4, 2/4]$, etc.

For each temperature we also ran calculations at $\lambda = 0$ and $\lambda = 1$ to estimate discretization error with the method explained in Appendix D which uses estimators $\mathcal{W}_{1/2}$ and $\mathcal{W}_2$ for $Q_{P/2}/Q_P$ and Q_{2P}/Q_P. These simulations were 10^7 Monte Carlo steps long, 14% were whole-chain moves and 86% were multi-slice moves performed on one sixth of the chain with the staging algorithm [144, 145] (this guaranteed that approximately the same computer time was spent on either of the two types of moves).

Results and discussion

The results of the calculations of the CD_4/CH_4 isotope effect are presented in Fig. 3.2. Panel (a) shows that the isotope effects calculated with the five different methods described in Sec. 3.2 agree, again confirming that the proposed methods based on stochastically changing masses during the simulation are implemented correctly. However, a more detailed inspection reveals the improvement provided by the stepwise and stochastic implementation of the direct estimators. The integration error of TI is plotted in panel (b), where the SDE result is considered exact; note that the TI exhibits a significant integration error at higher temperatures. (Recall again that the integration errors for STI, ODE, DE, and SDE are zero by construction.) It may seem surprising that the integration error is larger for smaller isotope effects, but one should remember that the interpolation (2.4) was derived with the goal of lowering the integration error in harmonic systems in the low temperature regime.

Finally, panel (c) of Fig. 3.2 shows that the STI and SDE exhibit smaller statistical errors than the TI and DE. For SDE, this was predicted in Subsec. 3.2.3 and justified by the decrease of the effective correlation length of samples corresponding to a particular value

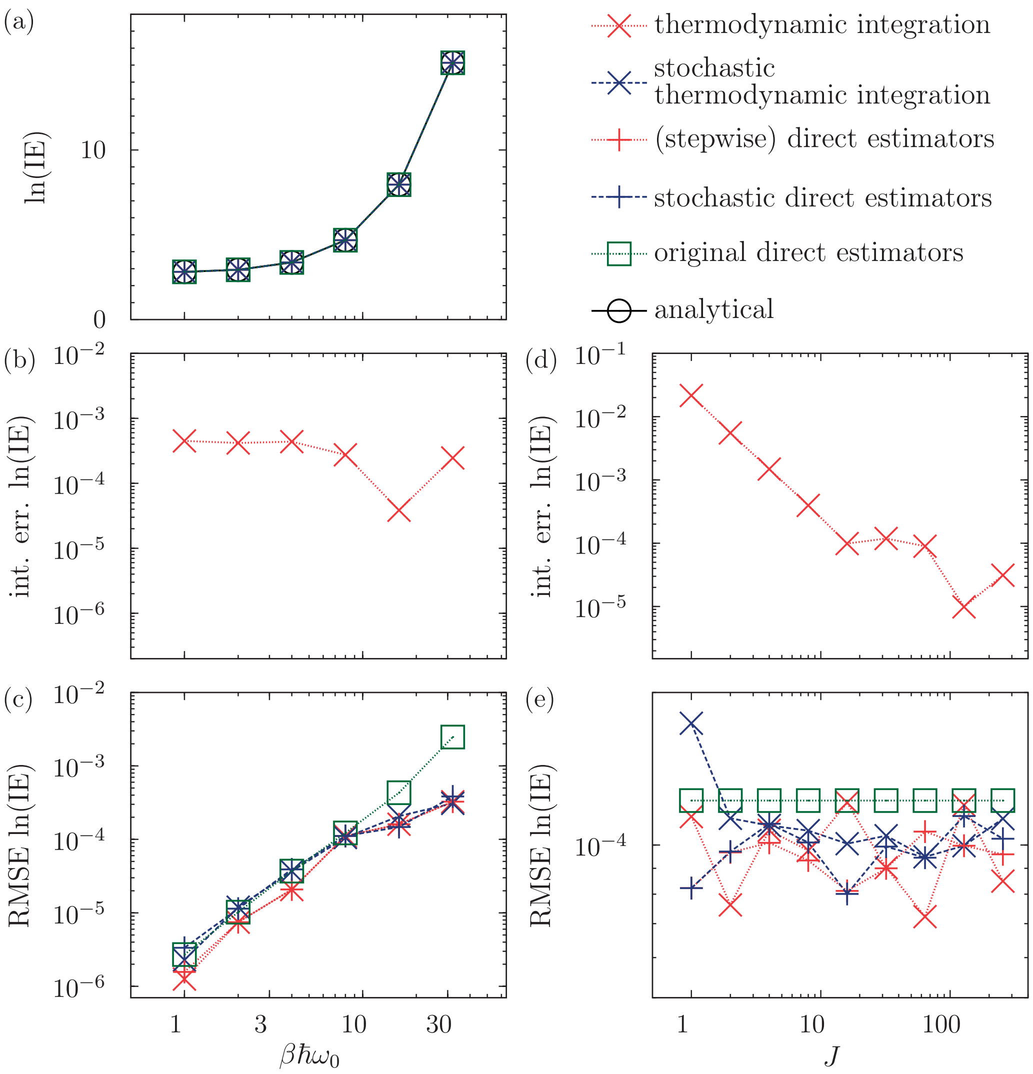

Figure 3.1: Isotope effect (IE) calculations in an eight-dimensional harmonic model from Subsec. 3.3.2. Thermodynamic integration (TI), stochastic thermodynamic integration (STI), stepwise direct estimators (DE), stochastic direct estimators (SDE), and original direct estimator approach from Ref. [1] are compared with exact analytical values (for the same finite Trotter number P). The proposed method is “stochastic direct estimators” (SDE), “direct estimators” (DE) has not been used before either. Panels (a)-(c) show the temperature dependence of (a) the isotope effect, (b) its integration errors, and (c) its statistical root mean square errors (RMSEs). Panels (d)-(e) display the dependence of integration errors and RMSEs on the number J of integration subintervals at a temperature given by $\beta\hbar\omega_0 = 8$.

of λ (or rather, a particular λ interval); the explanation for the case of STI is completely analogous. It is important to note that such an effect was not observed for TI and STI in Chapter 2, where we used a mass interpolating function that changed masses of all atoms at once. A likely reason is that this mass interpolating function resulted in a $\rho^{(\lambda)}(\{\mathbf{r}^{(s)}\})$ which was invariant to hydrogen atom permutations for each $\overline{\lambda}_j$; it is evident that this property was not shared by the mass interpolating function used in this chapter. Also note that at lower temperatures ODE demonstrates the highest statistical error of the five methods considered in this chapter, which is consistent with our discussion in Sec. 3.2; surprisingly, at higher temperatures it yields smaller statistical errors than TI and DE, which seems to be caused by the estimator being invariant to hydrogen permutations. The last interesting trend is similarity of statistical errors exhibited by TI and DE, as well as STI and SDE, which was also observed for the model harmonic system in Subsec. 3.3.2.

For reference, the plotted values together with statistical and discretization errors are listed in Table 3.1. From this table it is clear that DE, SDE, STI, and ODE agree within their statistical errors, while TI exhibits a significant integration error at high temperatures. Table 3.1 also contains estimates of the discretization error of the isotope effect obtained with the method described in Appendix D. Note that the discretization error only depends on P and not on the method used for the isotope effect calculation, and that our method for estimating this discretization error exhibits favorable statistical behavior.

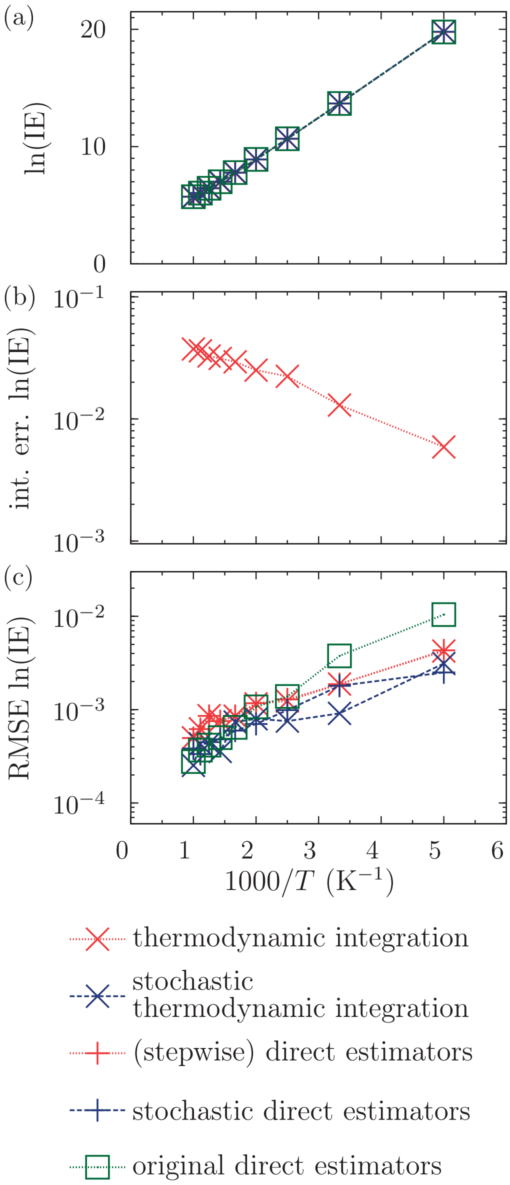

Figure 3.2: Calculations of the CD_4/CH_4 isotope effect (IE) from Subsec. 3.3.3. Labels are explained in the caption of Fig. 3.1. The three panels show the temperature dependence of (a) the isotope effect, (b) its integration errors, and (c) its statistical root mean square errors (RMSEs). For integration errors SDE values were used as the reference.

Table 3.1: Values of the CD_4/CH_4 isotope effect (IE) obtained with thermodynamic integration (TI), stochastic thermodynamic integration (STI), direct estimators (DE), and "stochastic direct estimators" (SDE). Corresponding statistical errors are shown as well. The proposed methodology is SDE. The discretization error is defined as $(\mathrm{IE}_P/\mathrm{IE} - 1)$ and is estimated with the procedure described in Appendix D.

T	P	ln(IE) (CD_4/CH_4) with statistical error					Estimate of discretization error (10^{-3})
		TI	STI	DE	SDE	ODE	
200	360	19.782 ± 0.005	19.784 ± 0.004	19.784 ± 0.005	19.788 ± 0.003	19.77 ± 0.02	-5.1 ± 0.3
300	226	13.661 ± 0.002	13.673 ± 0.001	13.676 ± 0.002	13.674 ± 0.002	13.673 ± 0.004	-3.7 ± 0.2
400	158	10.644 ± 0.002	10.665 ± 0.001	10.666 ± 0.002	10.666 ± 0.001	10.665 ± 0.002	-3.2 ± 0.2
500	118	8.883 ± 0.002	8.909 ± 0.002	8.910 ± 0.002	8.908 ± 0.001	8.911 ± 0.002	-3.0 ± 0.2
600	90	7.750 ± 0.001	7.781 ± 0.001	7.780 ± 0.002	7.779 ± 0.001	7.780 ± 0.001	-3.0 ± 0.2
700	72	6.974 ± 0.001	7.006 ± 0.001	7.006 ± 0.001	7.005 ± 0.001	7.006 ± 0.001	-2.8 ± 0.2
800	58	6.417 ± 0.001	6.451 ± 0.001	6.451 ± 0.001	6.450 ± 0.001	6.450 ± 0.001	-2.8 ± 0.2
900	46	6.003 ± 0.001	6.039 ± 0.001	6.039 ± 0.001	6.039 ± 0.001	6.038 ± 0.001	-3.4 ± 0.2
1000	36	5.689 ± 0.001	5.725 ± 0.001	5.725 ± 0.001	5.726 ± 0.001	5.726 ± 0.001	-3.9 ± 0.2

Table 3.2: Temperature dependence of the $CH_{4-x}D_x/CH_4$ isotope effect for x = 1, 2, 3. The results were obtained with “stochastic direct estimators”.

T	ln(IE) ($CH_{4-x}D_x/CH_4$)		
	x=1	x=2	x=3
200	4.882 ± 0.002	9.810 ± 0.002	14.778 ± 0.003
300	3.389 ± 0.001	6.800 ± 0.002	10.227 ± 0.002
400	2.652 ± 0.001	5.314 ± 0.001	7.985 ± 0.001
500	2.220 ± 0.001	4.445 ± 0.001	6.673 ± 0.001
600	1.940 ± 0.001	3.884 ± 0.001	5.830 ± 0.001
700	1.748 ± 0.001	3.499 ± 0.001	5.251 ± 0.001
800	1.611 ± 0.001	3.222 ± 0.001	4.835 ± 0.001
900	1.509 ± 0.001	3.018 ± 0.001	4.529 ± 0.001
1000	1.431 ± 0.001	2.862 ± 0.001	4.294 ± 0.001

Finally, as mentioned in the beginning of this section, modifying the interpolation formula for $m_i^{(\lambda)}$ allowed us to calculate the relative free energies of all deuterated methane species in a single STI or SDE simulation, just as in the case of an ODE calculation. For future reference the values of all the intermediate IEs are presented in Table 3.2.

As mentioned in the previous chapter, benefits of stochastically changing mass become most apparent when computational resources to run a simulation are limited. We therefore compared isotope effects obtained with TI, STI, and SDE using simulations of different length, starting with very short and nonergodic simulations. The results of these calculations, performed according to a prescription detailed in the previous chapter, are plotted in Fig. 3.3. The first observation is that calculations using only simple λ-moves cannot obtain a converged result of a SDE calculation. In Appendix C we explain why simple λ-moves are inefficient in making large changes of λ at lower temperatures, and in the converged CD_4/CH_4 isotope effect calculations the acceptance probability of a simple λ-move is of the order of only 10^{-7}. (This is because in SDE, the number J of λ intervals is only $J = 4$, making each interval rather large, unlike in STI, where J is typically much larger and simple λ-moves are much more likely.) On the other hand, adding some simple λ-moves appears to accelerate convergence in comparison to simulations using only mass-scaled λ-moves. This is probably because at initial times, the simple λ-moves turn out to be much more likely than when convergence is being approached and also because the cost of a simple λ-move is negligible (since it does not require potential energy evaluation and since we measure the cost in terms of number of potential energy evaluations). A similar acceleration of STI calculations by adding simple λ-moves is also clearly visible in Fig. 3.3 and was already observed in Ref. [2]. If no simple λ-moves are used then STI and SDE exhibit approximately equal rates of convergence. However, if simple λ-moves are used then at some point STI becomes more efficient than SDE.

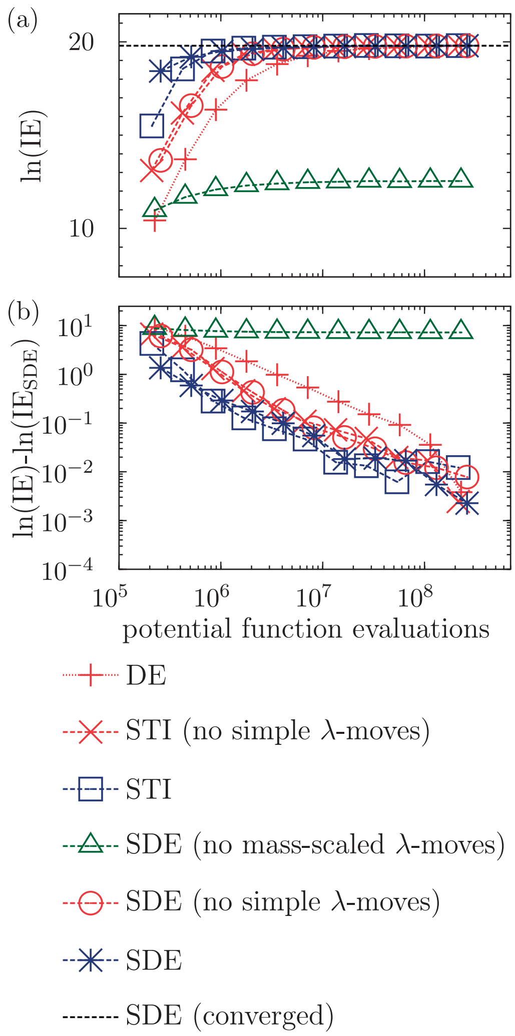

Figure 3.3: The impact of nonergodicity appearing in shorter calculations of the CD$_4$/CH$_4$ isotope effect (IE) at $T = 200$ K. Panel (a) presents the convergence of the IE as a function of the simulation length, while panel (b) shows the corresponding error of the IE (in logarithmic scale) relative to a converged STI result. Labels TI, STI and SDE are as in the caption of Fig. 3.1; "STI (no simple λ-moves)" and "SDE (no simple λ-moves)"were obtained without the simple λ-moves proposed in Ref. [2]; while "SDE (no mass-scaled λ-moves)" were obtained without mass-scaled λ-moves proposed in Ref. [2]. The horizontal line in panel (a) labeled "SDE (converged)" is the converged SDE result $\ln(\mathrm{IE}_{\mathrm{SDE}}) = 19.788$ from Fig. 3.2 and Table 3.1; the same value was used as a reference in panel (b).

3.4 Conclusion

We have investigated a stepwise implementation of direct estimators approach [1] and how it can be combined with a Monte Carlo procedure which was proposed in Chapter 3 for changing λ during the simulation. We found that stepwise implementation of the direct estimators exhibits an error which is very close to the one exhibited by thermodynamic integration in a wide range of conditions, however, unlike the latter approach, it does not introduce an integration error. It was already discussed in the previous chapter that changing λ during the simulation allows to decrease computational time required to obtain a converged result; in this work we observed a decrease of statistical error due to reduced effective correlation length of samples used to calculate the isotope effect.

As the original method of direct estimators [1], our Monte Carlo procedure allows to calculate several different isotope effects from a single simulation, with the advantage that larger isotope effects are determined with a smaller statistical error; this was demonstrated on the deuteration of methane in Subsec. 3.3.3.

It also appears that SDE and STI both exhibit quite similar numerical behavior in a wide range of situations. While SDE has a zero integration error by construction, it can exhibit large statistical errors if J is too small and the “intermediate” isotope effects are poorly suited for evaluation with direct estimators. Since the latter situation cannot be encountered in STI by definition, either of the methods can become the method of choice depending on the system.

We would like to note that the large magnitude of the isotope effects considered in numerical examples of this work lead to SDE and STI being more effective than the original direct estimators approach proposed in Ref. [1]. However we need to note that for smaller isotope effects original direct estimators approach can be more effective, for example if the isotope effect is associated with changing mass of one of a large number of interchangeable particles.

Finally, let us mention that the proposed methodology can be combined with Takahashi-Imada or Suzuki-Chin fourth-order factorizations [79–82] of the Boltzmann operator, which would allow lowering the path integral discretization error of the computed isotope effect for a given Trotter number P, and hence a faster convergence to the quantum limit [83, 115–117].

4 Combining virial estimators with higher-order Boltzmann operator splittings

4.1 Introduction

The results presented in this chapter have been published in Ref. [117].

In Sec. 1.4 we already mentioned quantum instanton approximation [3] to the rate constant. This approach is motivated by the semiclassical instanton theory [53, 54, 149, 150] and, as the name suggests, takes into account only the zero-time properties of the reactive flux-flux correlation function; however, in contrast to the semiclassical instanton, the quantum instanton approximation treats the Boltzmann operator exactly quantum mechanically. This improvement makes quantum instanton quite accurate as verified in many previous applications of the method [151–156]. Quantum instanton theory expresses the reaction rate in terms of imaginary-time correlation functions, which, in turn, can be evaluated by path integral Monte Carlo methods [12]; as for kinetic isotope effects, the problem can be simplified further by using thermodynamic integration with respect to mass [111]. The resulting approach exhibited errors that were already discussed in Chapter 2 for path integral equilibrium isotope effect calculations: statistical error, Boltzmann operator discretization error, and integration error of thermodynamic integration. The goal of this work is to accelerate quantum instanton kinetic isotope effect calculations by decreasing their statistical and discretization errors; to that end, we combined the following two approaches. The first approach employs Boltzmann operator factorizations of higher order of accuracy, which were briefly mentioned in Sec. 1.5. The resulting path integral representations of relevant quantities exhibit faster convergence to the quantum limit, allowing to reduce the value of P used in the calculation [82, 83, 115, 116, 127, 157]. The second approach uses improved estimators with lower statistical errors, which permit shortening the Monte Carlo simulation [112, 158]. In addition to combining these two strategies, we also propose several new estimators. We then test the resulting method on two systems: the model

$\cdot\mathrm{H}_\alpha + \mathrm{H}_\beta\mathrm{H}_\gamma \to \mathrm{H}_\alpha\mathrm{H}_\beta + \cdot\mathrm{H}_\gamma$ rearrangement, for which we also evaluate the resulting gain in computational efficiency, and the reaction $\mathrm{CH}_4 + \cdot\mathrm{H} \rightleftharpoons \cdot\mathrm{CH}_3 + \mathrm{H}_2$, a process whose kinetic isotope effects have been studied in detail both experimentally [159–162] and theoretically, with classical transition state theory, several of its corrected versions [163, 164], reduced dimensionality quantum dynamics [165], and ring polymer molecular dynamics [166].

4.2 Quantum instanton formalism

Quantum instanton approximation is derived by applying steepest descent approximation to the exact [54] Miller-Schwartz-Tromp formula (1.16). The derivation which was first proposed in Ref. [111] assumes that $C_{\mathrm{ff}}(t)$ is a fast decaying function and the main contribution to the integral in the right hand side of Eq. (1.16) comes from the neighborhood of $t = 0$; it also assumes that $C_{\mathrm{ff}}(t)/C_{\mathrm{dd}}(t)$ does not change much over the time interval relevant to integration. This allows one to write

$$\begin{aligned}\int_{-\infty}^{\infty} C_{\mathrm{ff}}(t)\,dt &= \int_{-\infty}^{\infty} \frac{C_{\mathrm{ff}}(t)}{C_{\mathrm{dd}}(t)} C_{\mathrm{dd}}(t)\,dt \\ &\approx \frac{C_{\mathrm{ff}}(0)}{C_{\mathrm{dd}}(0)} \int_{-\infty}^{\infty} C_{\mathrm{dd}}(t)\,dt \\ &\approx \frac{C_{\mathrm{ff}}(0)}{C_{\mathrm{dd}}(0)} \frac{\hbar\sqrt{\pi}}{2} \frac{C_{\mathrm{dd}}(0)}{\Delta H},\end{aligned} \tag{4.1}$$

obtaining the quantum instanton expression for the rate constant

$$k_{\mathrm{QI}} = \frac{\hbar\sqrt{\pi}}{2} \frac{C_{\mathrm{dd}}(0)}{Q_r} \frac{C_{\mathrm{ff}}(0)/C_{\mathrm{dd}}(0)}{\Delta H}, \tag{4.2}$$

where

$$\Delta H = \hbar\sqrt{-\frac{\ddot{C}_{\mathrm{dd}}(0)}{2C_{\mathrm{dd}}(0)}} \tag{4.3}$$

is a certain energy variance. For reasons that will become clear below, we keep $C_{\mathrm{dd}}(0)$ in Eq. (4.2), even though it may seem to cancel out. While this derivation will suffice for now, we note in advance that in Chapter 5 we will demonstrate that for some one-dimensional systems quantum instanton approximation can stay remarkably accurate even when stationarity of $C_{\mathrm{ff}}(t)/C_{\mathrm{dd}}(t)$ is violated.

The last question to be addressed is how to choose positions of the optimal dividing surfaces. From semiclassical considerations it follows that the best choice is to require that $C_{\mathrm{dd}}(0)$ be a saddle point with respect to ξ_a and ξ_b [3]; if ξ_γ are controlled by a set of parameters $\{\eta_k^{(\gamma)}\}$, the stationarity condition becomes

$$\frac{\partial C_{\mathrm{dd}}}{\partial \eta_k^{(\gamma)}} = 0. \tag{4.4}$$

4.3 General path integral implementation

In this section we will discuss how path integral formalism and Eq. (4.2) allows to calculate kinetic isotope effect using only classical Metropolis algorithm. Path integral expressions for Q_r and C_{dd} have already been presented in Sec. 1.5, and have been shown to be classical partition functions that correspond to ensembles defined by $\rho(\{\mathbf{r}^{(s)}\})$ and $\rho^{\ddagger}(\{\mathbf{r}^{(s)}\})$, and we will show how all the other quantities appearing in quantum instanton expression of kinetic isotope effect can be expressed in terms of thermodynamic averages over $\rho(\{\mathbf{r}^{(s)}\})$ and $\rho^{\ddagger}(\{\mathbf{r}^{(s)}\})$. Expressions for the corresponding estimators will be presented in a general way valid for all Boltzmann operator splittings considered in this work and as such will contain the main part common for all splittings and a part which corresponds to the fourth-order corrections and is only non-zero if a splitting other than LT is used; since this additional part depends on the gradient of the potential energy we will denote it by adding "grad" subscript to the name of the estimator. Although it is one of the main results of this work, for clarity the derivation of the parts associated with the fourth-order factorizations will be left for Appendix E.

4.3.1 Estimators for constrained quantities

We start with the path integral representation of $\ddot{C}_{\mathrm{dd}}(0)$ and ΔH^2, and to this end it is convenient to perform the Wick rotation and define a new function

$$\overline{C}_{\mathrm{dd}}(\zeta) := C_{\mathrm{dd}}\left(-\frac{\mathrm{i}\zeta\hbar}{2}\right) \tag{4.5}$$

of a complex argument ζ. Supposing that $C_{\mathrm{dd}}(t)$ is analytic,

$$\ddot{C}_{\mathrm{dd}}(t) = -\frac{4}{\hbar^2}\frac{\partial^2}{\partial\zeta^2}\overline{C}_{\mathrm{dd}}(\zeta)\bigg|_{\zeta=2\mathrm{i}t/\hbar}. \tag{4.6}$$

The path integral representation of $\overline{C}_{\mathrm{dd}}(\zeta)$ is obtained analogously to the one of $C_{\mathrm{dd}}(0)$ and reads

$$\overline{C}_{\mathrm{dd},P}(\zeta) = \overline{C}\int d\{\mathbf{r}^{(s)}\}\Delta_a(\mathbf{r}^{(P/2)})\Delta_b(\mathbf{r}^{(P)})\exp\left(-\beta^{+}\tilde{\Phi}^{+} - \beta^{-}\tilde{\Phi}^{-}\right), \tag{4.7}$$

with

$$\beta^{+} = \beta + \zeta, \tag{4.8}$$

$$\beta^{-} = \beta - \zeta, \tag{4.9}$$

prefactor

$$\overline{C} = \left(\frac{P}{2\hbar^2\pi\sqrt{\beta^2-\zeta^2}}\right)^{NDP/2}\left(\prod_{i=1}^{N} m_i\right)^{DP/2}, \tag{4.10}$$

and two "partial" effective potentials

$$\tilde{\Phi}^{+} = \frac{P}{2\hbar^2(\beta^+)^2}\sum_{s=1}^{P/2}||\mathbf{r}^{(s)}-\mathbf{r}^{(s-1)}||_{+}^{2}+\frac{1}{P}\sum_{s=0}^{P/2}\tilde{\tilde{w}}_s V_{\mathrm{eff}}^{(s)}(\mathbf{r}^{(s)}), \tag{4.11}$$

$$\tilde{\Phi}^{-} = \frac{P}{2\hbar^2(\beta^-)^2}\sum_{s=P/2+1}^{P}||\mathbf{r}^{(s)}-\mathbf{r}^{(s-1)}||_{+}^{2}+\frac{1}{P}\sum_{s=P/2}^{P}\tilde{\tilde{w}}_s V_{\mathrm{eff}}^{(s)}(\mathbf{r}^{(s)}), \tag{4.12}$$

where $\tilde{\tilde{w}}_s = \tilde{w}_s$ for all s except for $s = P/2$, for which $\tilde{\tilde{w}}_{P/2} = \tilde{w}_P = \tilde{w}_0$. The effective potentials $\tilde{\Phi}^+$ and $\tilde{\Phi}^-$ in Eq. (4.7) are obtained in a similar manner as $\tilde{\Phi}$ was obtained in Eq. (1.27). The difference is that instead of the matrix element of the Boltzmann operator $\exp(-\beta\hat{H})$ one considers an element of $\exp(-\beta^+\hat{H}/2)$ or $\exp(-\beta^-\hat{H}/2)$, and the exponential operators are discretized into $P/2$ rather than P parts. As a result, expressions (4.11)-(4.12) for $\tilde{\Phi}^+$ and $\tilde{\Phi}^-$ can be obtained from the one for $\tilde{\Phi}$ [Eq. (1.28)] if β is replaced with $\beta^+/2$ and $\beta^-/2$, respectively, and P is replaced with $P/2$. After differentiating expression (4.7) with respect to ζ, using Eq. (4.6) to go from $\overline{C}''_{\mathrm{dd},P}(\zeta)$ back to $\ddot{C}_{\mathrm{dd}}(t)$, and noting that $d\zeta = d\beta^+ = -d\beta^-$, one obtains

$$\ddot{C}_{\mathrm{dd},P}(0) = -\frac{1}{\hbar^2}C\int d\{\mathbf{r}^{(s)}\}\left(G+F^2\right)\rho^{\ddagger}(\{\mathbf{r}^{(s)}\}), \tag{4.13}$$

with

$$G = 4\left[\frac{d^2\ln C}{d\beta^2}-\frac{d^2(\beta^+\tilde{\Phi}^+)}{d(\beta^+)^2}-\frac{d^2(\beta^-\tilde{\Phi}^-)}{d(\beta^-)^2}\right], \tag{4.14}$$

$$F = 2\left[\frac{d(\beta^+\tilde{\Phi}^+)}{d\beta^+}-\frac{d(\beta^-\tilde{\Phi}^-)}{d\beta^-}\right]. \tag{4.15}$$

After the substitution of expressions (1.53) and (4.13) for $C_{\mathrm{dd},P}$ and $\ddot{C}_{\mathrm{dd},P}$ into the definition (4.3) of ΔH^2, the estimator for ΔH^2 takes the form

$$(\Delta H^2)_{P,\mathrm{est}} = \frac{G+F^2}{2} \tag{4.16}$$

if $\rho^{\ddagger}(\{\mathbf{r}^{(s)}\})$ is used as the weight function. From now on, we will denote estimators that are used with $\rho^{\ddagger}(\{\mathbf{r}^{(s)}\})$ the same way we denoted the ones used with $\rho(\{\mathbf{r}^{(s)}\})$; we shall not denote explicitly the probability density used as it will be clear from the context.

Explicit differentiation in Eqs. (4.14) and (4.15) leads to the so-called thermodynamic estimator [12],

$$G_{\mathrm{th}} = \frac{2NDP}{\beta^2}-\frac{4P}{\hbar^2\beta^3}\sum_{s=1}^{P}||\mathbf{r}^{(s)}-\mathbf{r}^{(s-1)}||_{+}^{2}+G_{\mathrm{th,grad}}, \tag{4.17}$$

$$F_{\mathrm{th}} = \frac{2}{P}\left(\sum_{s=1}^{P/2-1}-\sum_{s=P/2+1}^{P-1}\right)w_s V_{\mathrm{eff}}^{(s)}(\mathbf{r}^{(s)})-\frac{P}{\hbar^2\beta^2}\left(\sum_{s=1}^{P/2}-\sum_{s=P/2+1}^{P}\right)||\mathbf{r}^{(s)}-\mathbf{r}^{(s-1)}||_{+}^{2}+F_{\mathrm{grad}}. \tag{4.18}$$

The ratio $C_{\text{ff}}/C_{\text{dd}}$ can be computed by the Metropolis algorithm as well (from now on we will omit the argument of C_{dd} and C_{ff} if it equals 0). To obtain the corresponding estimator we first note that the flux operator can be expressed as

$$\hat{F}_\gamma = \frac{1}{2}\left\{\delta[\xi_\gamma(\hat{\mathbf{r}})]\langle\nabla\xi_\gamma(\hat{\mathbf{r}}),\hat{\mathbf{p}}\rangle_- + \langle\nabla\xi_\gamma(\hat{\mathbf{r}}),\hat{\mathbf{p}}\rangle_-\delta[\xi_\gamma(\hat{\mathbf{r}})]\right\}. \tag{4.19}$$

Combining $\hat{F}_\gamma$ with the path integral representation of the Boltzmann operator, one obtains [12]

$$C_{\text{ff},P} = C\int d\{\mathbf{r}^{(s)}\} f_{\text{v}}\rho^\ddagger(\{\mathbf{r}^{(s)}\}), \tag{4.20}$$

where f_{v} is the so-called velocity factor,

$$\begin{aligned} f_{\text{v}} =& \frac{\hbar^2}{4}\left\{\beta^2\prod_{\gamma=a,b}\left\langle\nabla\xi_\gamma(\mathbf{r}_\gamma),\left(\frac{\partial\tilde{\Phi}^+}{\partial\mathbf{r}_\gamma}-\frac{\partial\tilde{\Phi}^-}{\partial\mathbf{r}_\gamma}\right)\right\rangle_-\right.\\ &\left. -\beta\left\langle\nabla\xi_a(\mathbf{r}^{(P/2)}),\frac{\partial^2(\tilde{\Phi}^+ + \tilde{\Phi}^-)}{\partial\mathbf{r}^{(P/2)}\partial\mathbf{r}^{(P)}},\nabla\xi_b(\mathbf{r}^{(P)})\right\rangle_{--}\right\}\\ &/\{\prod_{\gamma=a,b}||\nabla\xi_\gamma(\mathbf{r}_\gamma)||_-\}, \end{aligned} \tag{4.21}$$

$\mathbf{r}_a = \mathbf{r}^{(P/2)}$, $\mathbf{r}_b = \mathbf{r}^{(P)}$, $\langle\cdot,\cdot\rangle_-$ is the inner product of two covariant vectors, and $\langle\cdot,\cdot,\cdot\rangle_{--}$ the matrix product of a covariant matrix with two covariant vectors (see Table 1.1). Taking the ratio of path integral representations (4.20) and (1.53) of C_{ff} and C_{dd} immediately yields the estimator for the ratio $C_{\text{ff}}/C_{\text{dd}}$:

$$\left(\frac{C_{\text{ff}}}{C_{\text{dd}}}\right)_{P,\text{est}} = f_{\text{v}}. \tag{4.22}$$

The thermodynamic estimator takes the form [12]

$$f_{\text{v,th}} = -\left(\frac{P}{2\hbar\beta}\right)^2\prod_{\gamma=a,b}\left\{\left\langle\nabla\xi_\gamma(\mathbf{r}_\gamma),(\mathbf{r}_\gamma^{(+1)}-\mathbf{r}_\gamma^{(-1)})\right\rangle_0/||\nabla\xi_\gamma(\mathbf{r}_\gamma)||_-\right\}, \tag{4.23}$$

where $\langle\cdot,\cdot\rangle_0$ is the inner product of a covariant and contravariant vectors (see Table 1.1), and we defined

$$\mathbf{r}_\gamma^{(+1)} := \begin{cases}\mathbf{r}^{(P/2+1)}, & \gamma = a,\\ \mathbf{r}^{(1)}, & \gamma = b,\end{cases} \tag{4.24}$$

$$\mathbf{r}_\gamma^{(-1)} := \begin{cases}\mathbf{r}^{(P/2-1)}, & \gamma = a,\\ \mathbf{r}^{(P-1)}, & \gamma = b.\end{cases} \tag{4.25}$$

4.3.2 Thermodynamic integration with respect to mass applied to the delta-delta correlation function

The last ingredient needed for evaluating the quantum instanton rate constant (4.2) is the ratio C_{dd}/Q_r, which, unfortunately, cannot be calculated by the standard Metropolis algorithm. However, in the case of kinetic isotope effect, one can circumvent this problem by employing the so-called thermodynamic integration with respect to mass [111], which is easy to understand from the explicit quantum instanton expression for the kinetic isotope effect,

$$\mathrm{KIE}_{\mathrm{QI}} = \frac{k_{\mathrm{QI}}^{(A)}}{k_{\mathrm{QI}}^{(B)}} = \frac{Q_r^{(B)}}{Q_r^{(A)}} \frac{C_{\mathrm{dd}}^{(A)}}{C_{\mathrm{dd}}^{(B)}} \frac{\Delta H^{(B)}}{\Delta H^{(A)}} \frac{C_{\mathrm{ff}}^{(A)}/C_{\mathrm{dd}}^{(A)}}{C_{\mathrm{ff}}^{(B)}/C_{\mathrm{dd}}^{(B)}}, \tag{4.26}$$

where A and B are different isotopologues of otherwise the same system. Application of thermodynamic integration to $Q_r^{(B)}/Q_r^{(A)}$ has already been discussed in Subsec. 2.2.1; we use the same $m_i^{(\lambda)}$ ($\lambda \in [0, 1]$) that were used for thermodynamic integration of Q_r and define $C_{\mathrm{dd}}^{(\lambda)}$ as the C_{dd} corresponding to masses $m_i^{(\lambda)}$, allowing us to write

$$\frac{C_{\mathrm{dd}}^{(B)}}{C_{\mathrm{dd}}^{(A)}} = \exp\left(\int_0^1 \frac{d\ln C_{\mathrm{dd}}^{(\lambda)}}{d\lambda} d\lambda\right). \tag{4.27}$$

The difference from $Q_r^{(B)}/Q_r^{(A)}$ is that one needs to keep track of the possible change of ξ_γ during the course of the integration,

$$\frac{d\ln C_{\mathrm{dd}}^{(\lambda)}}{d\lambda} = \frac{\partial \ln C_{\mathrm{dd}}^{(\lambda)}}{\partial\lambda} + \sum_{\gamma=a,b} \sum_k \frac{d\eta_k^{(\gamma)}}{d\lambda} \frac{\partial \ln C_{\mathrm{dd}}}{\partial \eta_k^{(\gamma)}}. \tag{4.28}$$

In Ref. [111] the authors proposed to choose $\{\eta_k^{(\gamma)}(\lambda)\}$ that satisfy Eq. (4.4) at each λ integration step, making the second term in Eq. (4.28) exactly zero and leaving only $\partial \ln C_{\mathrm{dd}}/\partial\lambda$ to be considered. Here we take an alternative and more numerically stable approach: By introducing new accurate estimators for $\partial \ln C_{\mathrm{dd}}/\partial\eta_k^{(\gamma)}$, we can avoid having to find the optimal values of $\eta_k^{(\gamma)}(\lambda)$ for all λ. Instead, we only find optimal $\eta_k^{(\gamma)}(\lambda)$ at the boundary points $\lambda \in \{0, 1\}$, obtain other, not necessarily optimal, $\eta_k^{(\gamma)}(\lambda)$ by linear interpolation, and evaluate both terms of Eq. (4.28) for each λ.

The estimator for $d\ln Q_r/d\lambda/\beta$ was already introduced in Subsec. (2.2.1) for the Lie-Trotter splitting and will be denoted as F_r to simplify the following discussion; for $\partial \ln C_{\mathrm{dd}}/\partial\lambda/\beta$ the estimator reads

$$\left(\frac{1}{\beta}\frac{\partial \ln C_{\mathrm{dd}}^{(\lambda)}}{\partial\lambda}\right)_{P,\mathrm{est}} = F^{\ddagger} = F_r + F_{\mathrm{ds}}, \tag{4.29}$$

where F_{ds} is the contribution that comes from differentiating the mass-dependent normalization factor in the normalized delta function (1.8):

$$F_{\mathrm{ds}} = -\frac{1}{\beta} \sum_{i=1}^{N} \frac{dm_i}{d\lambda} \sum_{\gamma=a,b} \frac{|\nabla_i \xi_\gamma(\mathbf{r}_\gamma)|^2}{2m_i^2 ||\nabla\xi_\gamma(\mathbf{r}_\gamma)||_-^2}. \tag{4.30}$$

Here ∇_i is the gradient with respect to coordinates of particle i (see Table 1.1).

Direct evaluation of Eq (4.29) yields [111] the thermodynamic estimator for $\partial \ln C_{\mathrm{dd}}/\partial\lambda$

$$F_{\mathrm{th}}^{\ddagger} = F_{r,\mathrm{th}} + F_{\mathrm{ds}}, \tag{4.31}$$

where $F_{r,\mathrm{th}}$ is thermodynamic estimator for $d\ln Q_r/d\lambda/\beta$ given by Eq. (2.7). Note that Eq. (2.7) was derived for the case of Lie-Trotter splitting (1.20), so for the fourth-order splittings considered in this work one needs to add the gradient correction $F_{r,\mathrm{grad}}$ presented in Appendix E. Derivation of the estimator for $\partial \mathrm{ln} C_{\mathrm{dd}}/\partial\eta_k^{(\gamma)}$ involves a rather tedious algebra and is therefore presented in Appendix F; the result is

$$\left(\frac{\partial \mathrm{ln} C_{\mathrm{dd}}}{\partial \eta_k^{(\gamma)}}\right)_{P,\mathrm{est}} = B^{k(\gamma)} = \frac{\partial \xi_\gamma(\mathbf{r}_\gamma)}{\partial \eta_k^{(\gamma)}} \left\{\beta \left\langle \nabla\xi_\gamma(\mathbf{r}_\gamma), \nabla^{(\gamma)}\Phi(\{\mathbf{r}^{(s)}\})\right\rangle_- - B_{\mathrm{ds}}^{k(\gamma)}\right\} /||\nabla\xi_\gamma(\mathbf{r}_\gamma)||_-^2, \tag{4.32}$$

where $\nabla^{(\gamma)}$ is the gradient with respect to $\mathbf{r}_\gamma$ and

$$B_{\mathrm{ds}}^{k(\gamma)} = \langle \nabla, \nabla\xi\rangle_- - \frac{1}{||\nabla\xi||_-^2}\left\langle \nabla\xi, \frac{\partial^2\xi}{(\partial\mathbf{r}_\gamma)^2}, \nabla\xi\right\rangle_{--} \tag{4.33}$$

is the term associated with the change of configuration space volume satisfying the constraint. Obtaining the thermodynamic estimator for $B^{k(\gamma)}$ is straightforward and yields

$$\begin{aligned} B_{\mathrm{th}}^{k(\gamma)} =& \frac{\partial \xi_\gamma(\mathbf{r}_\gamma)}{\partial \eta_k^{(\gamma)}} \left\{\frac{P}{\hbar^2\beta}\left\langle \nabla\xi_\gamma(\mathbf{r}_\gamma), (2\mathbf{r}_\gamma - \mathbf{r}_\gamma^{(-1)} - \mathbf{r}_\gamma^{(+1)})\right\rangle_0 + w_\gamma\left\langle \nabla\xi_\gamma(\mathbf{r}_\gamma), \nabla V_{\mathrm{eff}}^{(s)}(\mathbf{r}_\gamma)\right\rangle_- - B_{\mathrm{ds}}^{k(\gamma)}\right\} \\ & /||\nabla\xi_\gamma(\mathbf{r}_\gamma)||_-^2. \end{aligned} \tag{4.34}$$

4.3.3 Virial estimators

So far we have only considered thermodynamic estimators, which are obtained via direct differentiation of the Boltzmann operator matrix elements. However, as was already seen for $d\ln Q^{(\lambda)}/d\lambda$ in Subsec. 2.2.1, an estimator for a given quantity is not unique; it is often possible to obtain an estimator with smaller statistical error. Two of the five virial estimators used in this work, namely the estimators for ΔH^2 and $d\mathrm{ln}Q_r/d\lambda$ had been proposed previously [112, 158]; however, neither had been used in combination with the Suzuki-Chin factorization. To derive an expression for centroid virial estimator for $d\mathrm{ln}Q_r/d\lambda/\beta$ that would be valid not only for Lie-Trotter, but also for fourth-order Suzuki-Chin and Takahashi-Imada splittings, one takes steps analogous to the ones described in Chapter 2 to obtain

$$F_{r,\mathrm{cv}} = \sum_{i=1}^{N} \frac{1}{2m_i}\frac{dm_i}{d\lambda}\left\{\frac{D}{\beta} + \frac{1}{P}\sum_{s=1}^{P} w_s\left[(\mathrm{r}_i^{(s)} - \mathrm{r}_i^{(C)})\cdot\nabla_i V_{\mathrm{eff}}^{(s)}(\mathbf{r}^{(s)})\right]\right\} + F_{r,\mathrm{grad}}. \tag{4.35}$$

From now on we will refer to this estimator as “virial” for short.

For ΔH^2, one starts [158] by rewriting Eq. (4.7) using the coordinates

$$\mathbf{x}^{(s)} = \begin{cases} \check{\mathbf{r}}^{(s)} + \sqrt{\frac{\beta}{\beta^+}}(\mathbf{r}^{(s)} - \check{\mathbf{r}}^{(s)}), & 0 < s < P/2, \\ \check{\mathbf{r}}^{(s)} + \sqrt{\frac{\beta}{\beta^-}}(\mathbf{r}^{(s)} - \check{\mathbf{r}}^{(s)}), & P/2 < s < P, \\ \mathbf{r}^{(s)}, & s = 0, P/2, P, \end{cases} \tag{4.36}$$

where $\check{\mathbf{r}}^{(s)}$ is the reference point given by

$$\check{\mathbf{r}}^{(s)} = \check{\mathbf{r}}^{(P-s)} = \mathbf{r}^{(P)} + (\mathbf{r}^{(P/2)} - \mathbf{r}^{(P)})\frac{s}{P/2} \quad (0 < s < P/2). \tag{4.37}$$

The kinetic parts of $\tilde{\Phi}^{\pm}$ are rewritten in the new coordinates; e.g., for $\tilde{\Phi}^{+}$, one uses the relation

$$\frac{1}{\beta^{+}}\sum_{s=1}^{P/2} ||\mathbf{r}^{(s)} - \mathbf{r}^{(s-1)}||_{+}^{2} = \frac{1}{\beta}\sum_{s=1}^{P/2} ||\mathbf{x}^{(s)} - \mathbf{x}^{(s-1)}||_{+}^{2} + \left(\frac{1}{\beta^{+}} - \frac{1}{\beta}\right)\frac{||\mathbf{x}^{(P/2)} - \mathbf{x}^{(P)}||_{+}^{2}}{P/2}. \tag{4.38}$$

By substituting transformed $\tilde{\Phi}^{\pm}$ and $\overline{C}$ into Eqs. (4.14) and (4.15), one obtains the desired G and F terms of the virial estimator:

$$\begin{aligned} G_{\mathrm{v}} =& \frac{4ND}{\beta^{2}} - \frac{16}{\hbar^{2}\beta^{3}}||\mathbf{r}^{(P/2)} - \mathbf{r}^{(P)}||_{+}^{2} \\ & - \frac{1}{\beta P}\sum_{s=1}^{P} w_{s}\left[3\left\langle(\mathbf{r}^{(s)} - \check{\mathbf{r}}^{(s)}), \nabla V_{\mathrm{eff}}^{(s)}(\mathbf{r}^{(s)})\right\rangle_{0}\right. \\ & \left. + \left\langle(\mathbf{r}^{(s)} - \check{\mathbf{r}}^{(s)}), \frac{\partial^{2} V_{\mathrm{eff}}^{(s)}(\mathbf{r}^{(s)})}{(\partial \mathbf{r}^{(s)})^{2}}, (\mathbf{r}^{(s)} - \check{\mathbf{r}}^{(s)})\right\rangle_{00}\right] \\ & + G_{\mathrm{v,grad}}, \end{aligned} \tag{4.39}$$

$$F_{\mathrm{v}} = \frac{2}{P}\left(\sum_{s=1}^{P/2-1} - \sum_{s=P/2+1}^{P-1}\right) w_{s}\left[V_{\mathrm{eff}}^{(s)}(\mathbf{r}^{(s)}) + \frac{1}{2}\left\langle(\mathbf{r}^{(s)} - \check{\mathbf{r}}^{(s)}), \nabla V_{\mathrm{eff}}^{(s)}(\mathbf{r}^{(s)})\right\rangle_{0}\right] + F_{\mathrm{grad}}, \tag{4.40}$$

where $\langle \cdot, \cdot, \cdot \rangle_{00}$ is the matrix product of a covariant matrix with two contravariant vectors (see Table 1.1).

Now let us turn to the derivation of the new estimators promised in the Introduction. In particular, we propose new virial estimators for $\partial \ln C_{\mathrm{dd}}/\partial\lambda/\beta$, $C_{\mathrm{ff}}/C_{\mathrm{dd}}$, and $\partial \ln C_{\mathrm{dd}}/\partial\eta_{k}^{(\gamma)}$. For $\partial \ln C_{\mathrm{dd}}/\partial\lambda/\beta$ we use a coordinate rescaling

$$\mathrm{x}_{i}^{(s)} = \check{\mathrm{r}}_{i}^{(s)} + \sqrt{m_{i}/m_{i}'}(\mathrm{r}_{i}^{(s)} - \check{\mathrm{r}}_{i}^{(s)}), \tag{4.41}$$

which is similar to Eq. (4.36) and yields the virial estimator

$$\begin{aligned} F_{\mathrm{cv}}^{\ddagger} =& \sum_{i=1}^{N}\frac{dm_{i}}{d\lambda}\left\{\frac{D}{\beta m_{i}} - \frac{2}{(\beta\hbar)^{2}}(\mathrm{r}_{i}^{(P/2)} - \mathrm{r}_{i}^{(P)})^{2} + \frac{1}{2Pm_{i}}\sum_{s=1}^{P} w_{s}\left[(\mathrm{r}_{i}^{(s)} - \check{\mathrm{r}}_{i}^{(s)}) \cdot \nabla_{i} V_{\mathrm{eff}}^{(s)}(\mathbf{r}^{(s)})\right]\right\} \\ & + F_{\mathrm{ds}} + F_{r,\mathrm{grad}}. \end{aligned} \tag{4.42}$$

For $C_{\mathrm{ff}}/C_{\mathrm{dd}}$, we introduce new coordinates

$$\mathbf{x}^{(s)} = \mathbf{r}^{(s)} - \check{\mathbf{r}}^{(s)} \tag{4.43}$$

and employ the identity

$$\sum_{s=1}^{P/2} ||\mathbf{r}^{(s)} - \mathbf{r}^{(s-1)}||_{+}^{2} = \sum_{s=1}^{P/2} ||\mathbf{x}^{(s)} - \mathbf{x}^{(s-1)}||_{+}^{2} + \frac{||\mathbf{r}^{(P/2)} - \mathbf{r}^{(P)}||_{+}^{2}}{P/2}. \tag{4.44}$$

Rewriting $\tilde{\Phi}^{\pm}$ in terms of $\{\mathbf{x}^{(1)}, ..., \mathbf{x}^{(P/2-1)}, \mathbf{r}^{(P/2)}, \mathbf{x}^{(P/2+1)}, ..., \mathbf{x}^{(P-1)}, \mathbf{r}^{(P)}\}$ and inserting them into Eq. (4.21) leads to the virial estimator

$$f_{\mathrm{v,v}} = (\beta^2 v_a v_b - g_{ab})/\{\prod_{\gamma=a,b} ||\nabla\xi_\gamma(\mathbf{r}_\gamma)||_{-}\}, \tag{4.45}$$

$$v_\gamma = \frac{\hbar}{P^2}\left(\sum_{s=1}^{P/2-1} - \sum_{s=P/2+1}^{P-1}\right) e_\gamma^{(s)} w_s \left\langle \nabla\xi_\gamma(\mathbf{r}_\gamma), \nabla V_{\mathrm{eff}}^{(s)}(\mathbf{r}^{(s)})\right\rangle_{-}, \tag{4.46}$$

$$g_{ab} = \frac{\hbar^2\beta}{P^3}\sum_{s=1}^{P} e_a^{(s)} e_b^{(s)} w_s \left\langle \nabla\xi_a(\mathbf{r}^{(P/2)}), \frac{\partial^2 V_{\mathrm{eff}}^{(s)}(\mathbf{r}^{(s)})}{(\partial\mathbf{r}^{(s)})^2}, \nabla\xi_b(\mathbf{r}^{(P)})\right\rangle_{--} - \frac{\left\langle \nabla\xi_a(\mathbf{r}^{(P/2)}), \nabla\xi_b(\mathbf{r}^{(P)})\right\rangle_{-}}{\beta}, \tag{4.47}$$

where we introduced coefficients

$$e_\gamma^{(s)} = \begin{cases} \min(s, P-s), & \gamma = a, \\ |s - P/2|, & \gamma = b. \end{cases} \tag{4.48}$$

Using the same rescaling as for $f_{\mathrm{v,v}}$, we can also derive the virial estimator for $\partial \ln C_{\mathrm{dd}}/\partial\eta_k^{(\gamma)}$,

$$\begin{aligned} B_{\mathrm{v}}^{k(\gamma)} =& \frac{\partial\xi_\gamma}{\partial\eta_k^{(\gamma)}} \left\{ \frac{4}{\hbar^2\beta}\left\langle \nabla\xi_\gamma(\mathbf{r}_\gamma), (\mathbf{r}_\gamma - \mathbf{r}_\gamma^{(P/2)})\right\rangle_0 \right. \\ & \left. + \frac{2\beta}{P^2}\sum_{s=1}^{P} e_\gamma^{(s)} \left\langle \nabla\xi_\gamma(\mathbf{r}_\gamma), \nabla V_{\mathrm{eff}}^{(s)}(\mathbf{r}^{(s)})\right\rangle_{-} - B_{\mathrm{ds}}^{k(\gamma)} \right\} \\ & /||\nabla\xi_\gamma||_{-}^{2}, \end{aligned} \tag{4.49}$$

where $\mathbf{r}_\gamma^{(P/2)}$ stands for $\mathbf{r}^{(P)}$ if $\gamma = a$ and for $\mathbf{r}^{(P/2)}$ if $\gamma = b$.

We would like to comment on the cost of using the estimators described in this subsection. While thermodynamic estimators require little numerical effort, their virial counterparts depend on the gradient and Hessian of the effective potential. (Note that although $B_{\mathrm{th}}^{k(\gamma)}$ also depends on the force, it depends only on the force acting on a single bead, and hence its cost is negligible for large P.) It should be emphasized, however, that gradient- and Hessian-dependent parts of virial estimators can be calculated by finite difference, without the need to evaluate the gradient or Hessian explicitly. For example, $\langle \mathbf{w}, \nabla V\rangle_0$ and $\langle \mathbf{w}, \partial^2 V/\partial\mathbf{r}^2, \mathbf{w}\rangle_{00}$ are first and second derivatives of V in the direction of $\mathbf{w}$, and therefore can be evaluated by finite difference using just one and two additional evaluations of V, respectively. As a result, the effective cost is only one extra potential evaluation per bead for $F_{r,\mathrm{cv}}$, one per unconstrained bead for $F_{\mathrm{cv}}^{\ddagger}$, two per unconstrained bead for $(G_{\mathrm{v}} + F_{\mathrm{v}}^2)/2$, and three for $f_{\mathrm{v,v}}$. Calculating $B_{\mathrm{th}}^{k(\gamma)}$ will require exactly one potential evaluation and calculating $B_{\mathrm{v}}^{k(\gamma)}$ will require $P-1$ evaluations unless it is computed at the same time as $f_{\mathrm{v,v}}$ (in this case it would require just one extra potential evaluation, other numerical ingredients being shared with $f_{\mathrm{v,v}}$).

It should be emphasized that it is not necessary to evaluate these estimators after each Monte Carlo step due to finite correlation lengths inherent to Monte Carlo simulations. This realization frequently allows one to make the additional cost of evaluating even the more expensive estimators small compared with the cost of the random walk itself.

Finally, we would like to point out that, while authors of Refs. [112] and [127] used finite differences with respect to mass and β, respectively, to calculate virial estimators of interest, we found this approach less convenient since it requires introducing two parameters (finite difference steps) that must be adjusted for each new isotopologue and for each temperature. We therefore only used finite differences with respect to coordinates in the system's configuration space, with a single finite difference step which is the same for all isotopologues and all temperatures.

4.4 Applications

In summary, to compute the kinetic isotope effect on a reaction one must:

1. Estimate the Trotter number P that is sufficient to adequately describe the system. For this purpose we made several preliminary calculations to estimate the P necessary for the lowest and highest temperature; for other temperatures we used the empirical rule that $1/P$ stays approximately linear with respect to T.

2. Choose the two dividing surfaces. We chose $\xi_\gamma(\mathbf{r})$ of the form

$$\xi_\gamma(\mathbf{r}) = \xi(\mathbf{r}) - \eta_\gamma^\ddagger. \tag{4.50}$$

For reactions where atom X breaks its bond with atom Y and forms a bond with atom Z, we used as a reaction coordinate the difference of the "bond" lengths, i.e.,

$$\xi(\mathbf{r}) = R_{XY} - R_{XZ}, \tag{4.51}$$

where R_{XY} is the distance between X and Y. Optimal values of $\eta_\gamma^\ddagger$ were found by running test simulations to find the sign of $\partial \ln C_{\mathrm{dd}}/\partial \eta_\gamma^\ddagger$ at different values of $(\eta_a^\ddagger, \eta_b^\ddagger)$.

3. Run simulations at different values of λ in order to obtain the corresponding logarithmic derivatives of Q_r and C_{dd}, as well as $C_{\mathrm{ff}}/C_{\mathrm{dd}}$ and ΔH for $\lambda = 0$ and $\lambda = 1$, then evaluate Eqs. (2.5) and (4.27) using, e.g., Simpson's rule. For many systems $d\ln C_{\mathrm{dd}}/d\lambda$ and $d\ln Q_r/d\lambda$ are quite smooth functions and nine intermediate points were sufficient to accurately evaluate the thermodynamic integrals (i.e., the discretization error of the λ integral was smaller than the already small statistical error). We used linear mass

interpolation for this work, because we were not aware about the inverse square root interpolation (2.4) at that point and were also mainly focused on decreasing errors other than integration error. After this, evaluating the kinetic isotope effect using Eq. (4.26) is straightforward.

For each value of λ one has to run two Monte Carlo simulations in $\{\mathbf{r}^{(s)}\}$: a "constrained simulation" with two slices constrained to their respective dividing surfaces and a standard ("unconstrained") simulation. Since treating exact constraints is not straightforward in Monte Carlo methods, we approximated the delta constraint with a "smeared" delta function δ_{sm},

$$\delta[\xi_\gamma(\mathbf{r})] \approx \delta_{\mathrm{sm}}[\xi_\gamma(\mathbf{r})] = \frac{1}{\sqrt{2\pi}\sigma} \frac{1}{|\nabla\xi_\gamma(\mathbf{r})|} \exp\left\{ -\frac{1}{2\sigma^2} \left[\frac{\xi_\gamma(\mathbf{r})}{|\nabla\xi_\gamma(\mathbf{r})|} \right]^2 \right\}. \tag{4.52}$$

In contrast with the approximation used in Ref. [12], the width σ of our Gaussian δ_m does not depend on temperature or mass. The approximate constraint converges to the exact delta function as $\sigma \to 0$. Presence of $\delta_{\mathrm{sm}}[\xi_\gamma(\mathbf{r})]$ can be easily simulated by adding an extra constraining potential to two of the slices. For Monte Carlo sampling, we employed the staging algorithm [144, 145, 167] with multislice moves in combination with whole-chain moves. For constrained simulations, we also made extra single-slice moves of slices $P/2$ and P, since these slices are more rigid than others due to the presence of the constraining potential.

4.4.1 $\cdot\mathrm{H} + \mathrm{H}_2$ rearrangement

Recall that the errors of path integral Monte Carlo calculations come mostly from two sources: the path integral discretization error (due to P being finite) and the statistical error inherent to Monte Carlo methods. (As for quantities evaluated with thermodynamic integration, there is an additional discretization error of the thermodynamic integral due to taking a finite number of λ steps.) To verify the improvements outlined in Sec. 4.3 we studied their influence on the behavior of the two main types of errors when applied to the model $\cdot\mathrm{H}_\alpha + \mathrm{H}_\beta\mathrm{H}_\gamma \to \mathrm{H}_\alpha\mathrm{H}_\beta + \cdot\mathrm{H}_\gamma$ rearrangement using the BKMP2 potential energy surface [168] at the temperature of 200 K. The BKMP2 potential used in this work was designed to be accurate for a wide range of geometries, including both the reactant and transition state regions. The behavior of the logarithmic derivatives was studied on the kinetic isotope effect $\cdot\mathrm{H} + \mathrm{H}_2 / \cdot \mathrm{D} + \mathrm{D}_2$.

Computational details

Statistically converged simulations (paralleled over 64 trajectories, 4×10^7 Monte Carlo steps each) were run with different values of the Trotter number (from $P = 8$ to 64 with step 4 and from 64 to 352 with step 16) and different Boltzmann operator factorizations. Virial estimators were evaluated only after every 25 Monte Carlo steps, whereas the thermodynamic - after every step, because the additional cost was negligible. To estimate statistical errors of the results we calculated root mean square deviations of averages over different trajectories. [Having a relatively high number (64) of uncorrelated trajectories, we could thus avoid a more tedious block-averaging procedure [139], but we did check in several cases that the two approaches gave very similar statistical error estimates.] As for the positions of the dividing surfaces, for calculating the kinetic isotope effect choosing $\eta_a^\ddagger = \eta_b^\ddagger = 0$ was quite satisfactory even at $T = 200$ K (in this case C_{dd} is stationary from symmetry considerations) for analyzing numerical behavior of $\partial \mathrm{ln} C_{\mathrm{dd}}/\partial\lambda$, ΔH^2 and $C_{\mathrm{ff}}/C_{\mathrm{dd}}$. For $\partial \mathrm{ln} C_{\mathrm{dd}}/\partial\eta_a^\ddagger$, however, we used $\eta_a^\ddagger = -0.5$ and $\eta_b^\ddagger = 0.5$ in order to make the logarithmic derivative statistically relevant.

For this particular setup the increase of central processing unit (CPU) time associated with evaluating all virial estimators at once was about 15% for constrained and 3.5% for unconstrained simulations. The increase of CPU time associated with the use of higher-order splittings was negligible for constrained simulations; for unconstrained simulations it was 2.5% and 5% for Suzuki-Chin and Takahashi-Imada splittings, respectively.

Results

Convergence of different quantities to their quantum limits as a function of the Trotter number P is shown in Fig. 4.1. As expected, the Suzuki-Chin factorization allows to lower the Trotter number significantly in comparison with the Lie-Trotter factorization. In the case of $d\mathrm{ln}Q_r/d\lambda$ the Suzuki-Chin splitting is slightly outperformed by the Takahashi-Imada factorization, which has a smaller prefactor of the error term, possibly because the Takahashi-Imada splitting leads to an expression invariant under cyclic bead permutations.

Statistical errors of different estimators are presented in Fig. 4.2. Note that they do not depend much on the factorization used. In contrast, the decrease of statistical errors associated with using virial estimators is remarkable for all quantities.

To compare the speedups achieved by different combinations of splittings and estimators we estimated the relative CPU times needed to converge the quantities ΔH, $C_{\mathrm{ff}}/C_{\mathrm{dd}}$, $Q_r^{(B)}/Q_r^{(A)}$, and $C_{\mathrm{dd}}^{(B)}/C_{\mathrm{dd}}^{(A)}$ to 1% discretization and statistical errors.[1] To estimate the speedup associated with calculating the overall kinetic isotope effect with 1% statistical and discretization errors we ran a separate set of simulations with $\lambda = 1$ in addition to those for $\lambda = 0$; the statistical and discretization errors of the kinetic isotope effect calculated with different combinations of estimators and factorizations were then approximated with the corresponding errors obtained if thermodynamic integration of Q_r and C_{dd} had been performed using a single step trapezoidal rule (i.e., based just on the two boundary points $\lambda = 0$ and $\lambda = 1$).

---

[1] Note that the 1% error for ΔH translates into a 2% error for ΔH^2 and that 1% relative error for Q_r and C_{dd} ratios translate into 0.01 absolute error for $\partial \ln Q_r/\partial\lambda$ and $\partial \ln C_{\mathrm{dd}}/\partial\lambda$. As for $\partial \ln C_{\mathrm{dd}}/\partial\eta_a^\ddagger$, as will be shown later, when we calculate the kinetic isotope effect $\cdot\mathrm{H} + \mathrm{H}_2/\cdot\mathrm{D} + \mathrm{D}_2$ at $T = 200\,\mathrm{K}$ with properly optimized dividing surfaces, $\partial \ln C_{\mathrm{dd}}/\partial\eta_a^\ddagger$ is integrated over an interval of the length 0.59 a. u., implying that the target error should be $0.01/0.59(\mathrm{a.\,u.})^{-1}$.

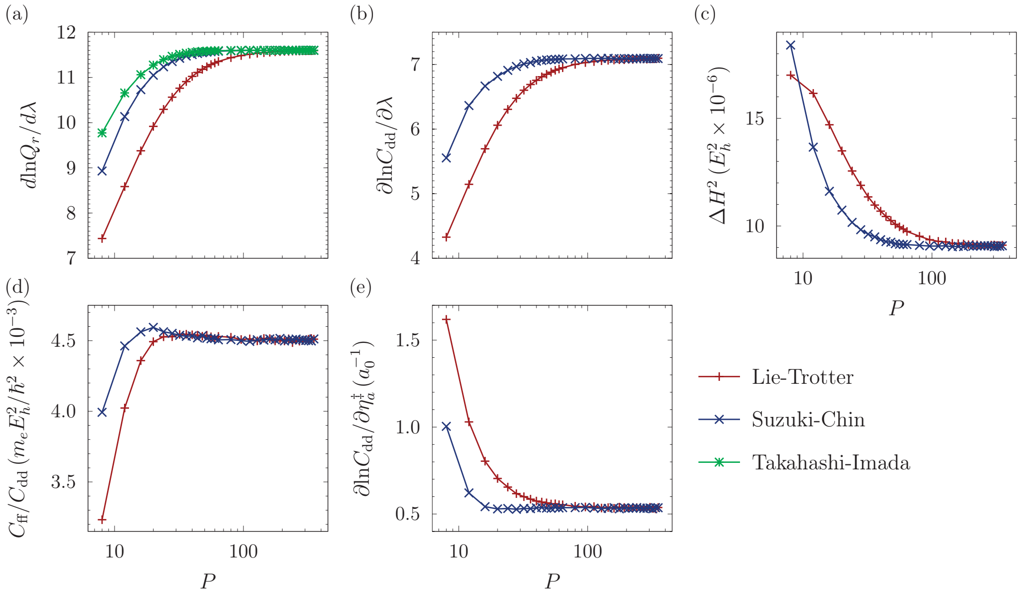

Figure 4.1: Convergence of various quantities required in the quantum instanton approximation of the kinetic isotope effect to the quantum limit as a function of the Trotter number P: (a) $d\ln Q_r/d\lambda$, (b) $\partial\ln C_{\rm dd}/\partial\lambda$, (c) ΔH^2, (d) $C_{\rm ff}/C_{\rm dd}$, (e) $\partial\ln C_{\rm dd}/\partial\eta_a^\ddagger$. Results shown were obtained with the virial estimators and correspond to the kinetic isotope effect $\cdot\mathrm{H}+\mathrm{H}_2/\cdot\mathrm{D}+\mathrm{D}_2$ at 200 K.

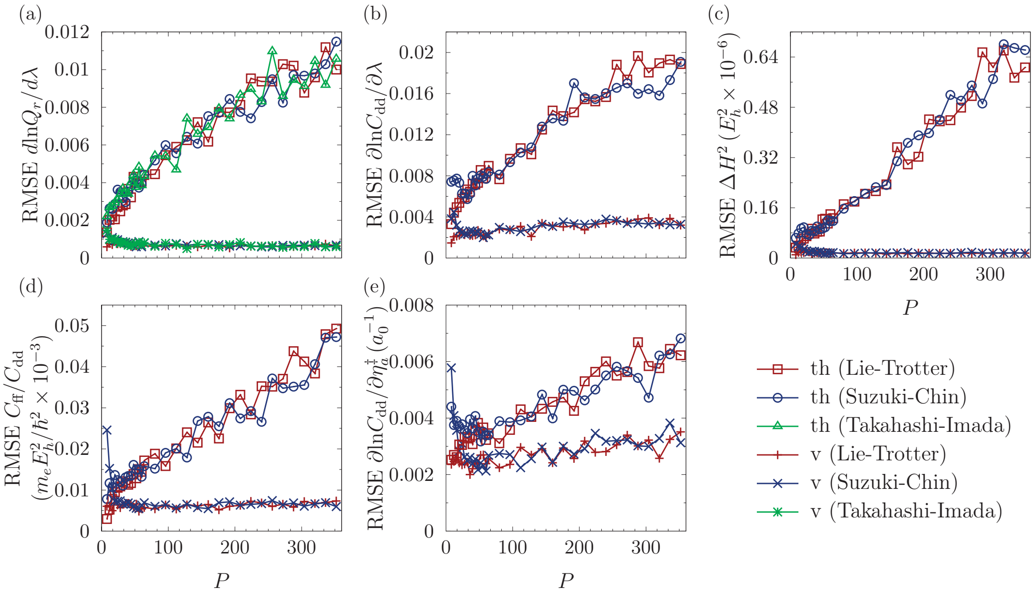

Figure 4.2: Statistical root mean square errors (RMSE) obtained with different estimators at different values of the Trotter number P for quantities required in the quantum instanton approximation. (a) $d\ln Q_r/d\lambda$, (b) $\partial\ln C_{\rm dd}/\partial\lambda$, (c) ΔH^2, (d) $C_{\rm ff}/C_{\rm dd}$, (e) $\partial\ln C_{\rm dd}/\partial\eta_a^\ddagger$. Results correspond to the kinetic isotope effect $\cdot\mathrm{H}+\mathrm{H}_2/\cdot\mathrm{D}+\mathrm{D}_2$ at 200 K. "v" stands for "virial", "th" - for "thermodynamic".

Let us assume the CPU time of a simulation to be approximately proportional to P and the number of Monte Carlo steps. Then for a given combination of factorization and estimator the cost of achieving the target discretization and statistical errors is proportional to the product $\tilde{P}\sigma_{\tilde{P}}^2$, where $\tilde{P}$ is the value of the Trotter number that yields the target discretization error and $\sigma_{\tilde{P}}$ is the statistical error exhibited by the estimator at this value of P. These estimates of CPU cost are then corrected by the increase in CPU time associated with using the fourth-order splittings and virial estimators. The final results are presented in Tab. 4.1, which confirms that the combination of virial estimators and fourth-order splittings leads to a significant speedup of the calculation.

One may be surprised that the value of P necessary to achieve 1% convergence of $C_{\mathrm{ff}}/C_{\mathrm{dd}}$ appears to be roughly independent of the splitting used; this is probably because the discretization errors of C_{dd} and C_{ff} cancel to a larger extent for the Lie-Trotter than the Suzuki-Chin splitting. Taking the discretization error to be 0.5% rather than 1% makes the difference in the required value of P even more pronounced: $P = 40$ for the Lie-Trotter and $P = 80$ for the Suzuki-Chin splitting.

Note that even though the values of P required to converge individual quantities are quite large (up to $P = 336$ for $d\ln Q_r/d\lambda$ if Lie-Trotter splitting is used), the Trotter number P necessary to converge the final kinetic isotope effect result is significantly lower due to the cancellation of discretization errors between individual quantities and especially between the two isotopologues. However, our P value required for the kinetic isotope effect computed with the Lie-Trotter splitting is still larger than, for instance, those used in Ref. [12], where the authors obtained the final result by extrapolating to the $P \to \infty$ limit.[2]

It is also interesting to relate our results to those of Ref. [157], where the authors compared efficiencies of the Lie-Trotter, Takahashi-Imada, and fourth-order Chin [169, 170] factorizations for finding different quantities associated with the ring polymer molecular dynamics expression for the reaction rate. The authors found that for dynamical properties the Takahashi-Imada splitting gives little improvement over the standard Lie-Trotter factorization, which is consistent with our explanation presented in Subsec. 1.5; both factorizations are outperformed by the fourth-order Chin factorization, which is in agreement with the Suzuki-Chin outperforming Lie-Trotter splitting in Tab. 4.1. For equilibrium properties, the authors found that the efficiencies of the Chin and Takahashi-Imada factorizations are similar, and that both fourth-order factorizations significantly outperform the standard Lie-Trotter splitting, again in agreement with our results and explanation.

We mentioned earlier that we had calculated virial estimators by finite difference, making the computational cost of their evaluation independent of dimensionality. To employ fourth-order splittings, however, one must know the potential gradient for all P replicas

---

[2] Since thermodynamic estimators were used in Ref. [12], reducing the discretization error directly using very large P was not feasible—increasing P not only decreased discretization error, but also increased the statistical error. Introducing virial estimators for each relevant quantity allows avoiding this issue because it permits improving convergence with respect to P without encountering problems with statistical error.

Table 4.1: Estimated speedups of the quantum instanton calculations achieved by the use of various combinations of path integral factorizations and estimators (th = thermodynamic, v = virial). Speedup "1" (i.e., no speedup) corresponds to the standard method employing a combination of the Lie-Trotter factorization and thermodynamic estimators. Results correspond to the kinetic isotope effect (KIE) $\cdot\mathrm{H}+\mathrm{H}_2/\cdot\mathrm{D}+\mathrm{D}_2$ at 200 K.

Factorization	Lie-Trotter (LT)			Suzuki-Chin (SC)			Takahashi-Imada (TI)		
Estimator	P	th	v	P	th	v	P	th	v
$d\mathrm{ln}Q_r/d\lambda$	336	1	220	96	10	850	64	44	1200
$\partial\mathrm{ln}C_{\mathrm{dd}}/\partial\lambda$	240	1	19	64	13	160	_	_	_
ΔH^2	128	1	170	48	14	380	_	_	_
$C_{\mathrm{ff}}/C_{\mathrm{dd}}$	36	1	2.7	32	1.3	3.0	_	_	_
$\partial\mathrm{ln}C_{\mathrm{dd}}/\partial\eta_a^{\ddagger}$	80	1	1.7	16	3.6	3.8	_	_	_
KIE	128	1	34	40	12	97[1]	_	_	_

[1] All quantities except for $d\ln Q_r/d\lambda$ are calculated with the SC factorization. For $d\ln Q_r/d\lambda$ TI factorization is used.

(for the Takahashi-Imada splitting) or at least for $P/2$ replicas (for the Suzuki-Chin splitting if $\alpha = 0$ or $\alpha = 1$). In general, if evaluating the gradient becomes too expensive compared to the potential energy itself, it may be advantageous to use the Lie-Trotter instead of the fourth-order splittings. For example, as shown in Tab. 4.1, using the fourth-order splittings decreased the necessary P approximately four times; therefore, for this particular system it is reasonable to use the Takahashi-Imada factorization if the cost of evaluating the gradient is smaller than three times the cost of evaluating the potential alone. For the Suzuki-Chin factorization the corresponding factor is around six, since one needs only $P/2$ force evaluations. This upper bound for efficiency may be pushed further using the reweighting-based techniques [82, 83, 127]; this approach, however, is known to increase the statistical errors of the final result in high-dimensional systems [171].

Lastly, we verified the modified methodology by comparing our result for the kinetic isotope effect $\cdot\mathrm{H}+\mathrm{H}_2/\cdot\mathrm{D}+\mathrm{D}_2$ with those of Ref. [111], obtained both with the quantum instanton approximation and with an exact quantum method. For each temperature we calculated ΔH and $C_{\mathrm{ff}}/C_{\mathrm{dd}}$ by path integral Monte Carlo simulations with 1.28×10^8 steps at $\lambda = 0$ and $\lambda = 1$. Ratios of Q_r and C_{dd} were evaluated by rewriting them as in Eqs. (2.5) and (4.27) respectively and finding the integral over λ using Simpson's rule with integration step $\Delta\lambda = 0.1$. At $T = 200$ K we also ran calculations with $\Delta\lambda = 0.05$ to verify that the integration error of the final result is lower than the statistical error. Values of $\partial\mathrm{ln}C_{\mathrm{dd}}/\partial\lambda$ within the integration interval were obtained by running simulations with 6.4×10^7 Monte Carlo steps (i.e., fewer steps than for the λ-endpoint simulations because $\partial\mathrm{ln}C_{\mathrm{dd}}/\partial\lambda$ and $d\mathrm{ln}Q_r/d\lambda$ tend to converge faster than $C_{\mathrm{ff}}/C_{\mathrm{dd}}$ and especially than ΔH). These conditions ensured that the total relative error of the final KIE caused by statistical noise was below 1%. We chose P in such a way that the relative error due to P being finite was less than the statistical one. At the lowest temperature $T = 200\,\mathrm{K}$ we chose $P = 64$, while for $T = 2400$ K $P = 12$ turned out to be appropriate; for other temperatures we estimated the necessary P by interpolation assuming that the $1/P$ is a linear function of T. To verify that the chosen values of P were sufficient we ran additional simulations

Table 4.2: Kinetic isotope effect $\cdot\mathrm{H} + \mathrm{H}_2 / \cdot\mathrm{D} + \mathrm{D}_2$ at different temperatures. “QI” stands for “quantum instanton.”

T (K)	optimal $\eta_a^\ddagger = -\eta_b^\ddagger$		QI		QM[1]	% error[2]	QI[1]
	$\lambda = 0$	$\lambda = 1$	no surface optimization	optimized surfaces			
200	1.00	0.41	22.3 ±0.2	22.6 ±0.3	22.53	< 1	23.15
250	0.62	0	10.91±0.08	9.92±0.09	10.40	−5	10.98
300	0.01	0	7.38±0.05	7.35±0.05	6.97	5	7.41
400	0	0	_	4.87±0.03	4.74	3	4.84
600	0	0	_	3.29±0.02	3.42	−4	3.25
1000	0	0	_	2.23±0.01	2.61	−15	2.22
1500	0	0	_	1.81±0.01	2.27	−20	1.83
2400	0	0	_	1.55±0.01	_	_	1.56

[1] Ref. [111]. QM denotes exact quantum-mechanical results from this reference.

[2] The error is defined as $(\mathrm{KIE}_{\mathrm{QI}} - \mathrm{KIE}_{\mathrm{QM}})/\mathrm{KIE}_{\mathrm{QM}} \times 100\%$ for the optimized dividing surfaces’ case.

at temperatures 200 K, 1000 K, and 2400 K with $\lambda = 0$ and $\lambda = 1$ with a doubled value of P. If two kinetic isotope effects calculated with $\Delta\lambda = 1$ at the two different values of P differed by a value that was lower then the sum of their statistical errors, the lower value of P was deemed sufficient for the calculation. The statistical errors, i.e., root mean square errors (RMSE) were estimated with the “block-averaging” method [139] in order to remove the effect of correlation length of the random walk in the Metropolis Monte Carlo simulation.

In Ref. [111], $\eta_\gamma^\ddagger$ were taken to be 0 for all temperatures and all values of λ. Even though this choice of dividing surfaces’ positions leads to C_{dd} being stationary, it is a local minimum rather than a saddle point. We therefore also checked the result for the case when the proper optimal dividing surfaces’ positions are found. Since from symmetry considerations the optimal dividing surfaces’ parameters satisfy $\eta_a^\ddagger = -\eta_b^\ddagger$, simple bisection was sufficient to calculate the values up to 0.01 a.u. The results are presented in Table 4.2. Intermediate results of the calculations are presented separately in Table G.1 in Appendix G. We can see that the values obtained with $\eta_\gamma^\ddagger = 0$ agree well with those of Ref. [111], validating our modifications. It can also be seen that full dividing surfaces’ optimization improves agreement of the quantum instanton results with the exact quantum result, making the method remarkably accurate at low temperatures.

4.4.2 $\mathbf{CH_4 + \cdot H \rightleftharpoons \cdot CH_3 + H_2}$ exchange

As mentioned, the kinetic isotope effects on the $\mathrm{CH}_4 + \cdot\mathrm{H} \rightleftharpoons \cdot\mathrm{CH}_3 + \mathrm{H}_2$ exchange had been studied by various numerical methods, but not by the quantum instanton approximation. We therefore decided to test the accelerated quantum instanton method on this reaction using the potential energy surface published in Ref. [7]. The surface is a global one obtained by fitting *ab initio* potential values. Using invariant polynomial methods [172–174] for the fit ensured that the resulting force field is invariant with respect to hydrogen atom permutations.

Computational details

We first ran a series of trial simulations to roughly determine the value of P and the number of Monte Carlo steps ensuring that at the lowest temperature the relative statistical error of the kinetic isotope effect is below 1% and that the discretization error with respect to P is even smaller. The target statistical error was guaranteed by running 6.4×10^7 step Monte Carlo simulations at $\lambda = 0$ and $\lambda = 1$, and 3.2×10^7 simulations at other values of λ. The target discretization error was achieved with $P = 80$ for the Lie-Trotter and $P = 20$ for the combination of fourth-order splittings at $T = 400\,\mathrm{K}$; at other temperatures P was chosen such that the ratio β/P stayed approximately constant. We chose $\Delta\lambda = 0.1$ as for the case of $\cdot\mathrm{H} + \mathrm{H}_2/\cdot\mathrm{D} + \mathrm{D}_2$; to be completely sure that the thermodynamic integration error was negligible to the statistical one, we also ran calculations with $\Delta\lambda = 0.05$ at $T = 400\mathrm{K}$ for the equilibrium isotope effect $\cdot\mathrm{CH}_3/\cdot\mathrm{CD}_3$ and kinetic isotope effect $\cdot\mathrm{CH}_3 + \mathrm{D}_2/\cdot\mathrm{CD}_3 + \mathrm{D}_2$, as these cases exhibited the most drastic changes of properties during thermodynamic integration.

To determine the stationary positions of the dividing surfaces ($\{\eta^\ddagger_\gamma\}$) we ran several short (8×10^6 steps) simulations to find the sign of $\partial \ln C_{\mathrm{dd}}/\partial\eta^\ddagger_\gamma$ at different positions of the dividing surfaces; the saddle points were found with accuracy of 0.01 a.u. The difference between $\eta^\ddagger_a$ and $\eta^\ddagger_b$ turned out to be negligible at all temperatures considered, in accordance with what is expected at "high" temperatures [151]. The calculated values of $\eta^\ddagger$ are presented in Tab. G.2 in Appendix G; as expected, they are quite close to the position of the classical transition state at $\eta^\ddagger = -0.94$.

Results

Next, we compared results obtained by the accelerated method (employing a combination of fourth-order splittings and virial estimators) and by the standard method (employing a combination of Lie-Trotter splitting and thermodynamic estimators). The corresponding numerical results are labeled as "accel." and "std.," respectively, "QI" stands for "quantum instanton." For further comparison, we calculated the same kinetic isotope effects also with the conventional transition state theory (TST) [175–177] and TST with Wigner tunneling correction [26] (in the tables the corresponding columns are denoted as "TST" and "TST + Wigner" respectively), both methods having been discussed in Sec. 1.2. Since the conventional TST expression captures the changes of zero-point energy as well as of the rotational and translational partition functions due to the isotopic substitution, one may expect that the difference between the quantum instanton and conventional TST should be largely due to the difference between the extent of tunneling present in the two isotopologues. The results are presented in Tables 4.3-4.9.

First of all, it can be seen that for kinetic isotope effects due to mass changes not

Table 4.3: Kinetic isotope effect $\mathrm{CH_4} + \cdot\mathrm{H}/\mathrm{CH_4} + \cdot\mathrm{D}$.

T (K)	TST	TST +Wigner	QI		TST[1]	CVT/ μOMT[1]	RDQD[2]	RPMD[3]	Expt.[4]
			accel.	std.					
400	0.56	0.56	0.60±0.01	0.62±0.07	0.54	0.58	0.64		0.74[5]
500	0.66	0.66	0.70±0.01	0.65±0.08	0.65	0.67	1.03	0.65	0.84[5]
600	0.74	0.74	0.78±0.01	0.7 ±0.1	0.73	0.74	1.23		0.91[5]
700	0.79	0.79	0.84±0.01	0.9 ±0.1	0.78	0.79	1.33	0.80	0.97[5]

[1] Ref. [164]
[2] Ref. [165]
[3] Ref. [166]
[4] Ref. [159]
[5] Values taken from Ref. [164].

Table 4.4: Kinetic isotope effect $\cdot\mathrm{CH_3} + \mathrm{D_2}/\cdot\mathrm{CD_3} + \mathrm{D_2}$.

T (K)	TST	TST+Wigner	QI		TST[1]	CVT/μOMT[1]	Expt.[2]
			accel.	std.			
400	0.73	0.74	0.76±0.01	0.7±0.1	0.75	0.74	0.59[3]
500	0.82	0.82	0.83±0.01	0.9±0.1	0.83	0.82	0.72[3]
600	0.87	0.88	0.88±0.01	0.8±0.2	0.88	0.88	0.82[3]
700	0.91	0.91	0.90±0.01	0.8±0.2	0.92	0.91	0.90[3]

[1] Ref. [164]
[2] Based on data from Refs. [160–162]
[3] Values taken from Ref. [178].

Table 4.5: Kinetic isotope effect $\cdot\mathrm{CH_3} + \mathrm{H_2}/\cdot\mathrm{CD_3} + \mathrm{H_2}$.

T (K)	TST	TST+Wigner	QI		TST[1]	CVT/μOMT[1]	Expt.[2]
			accel.	std.			
400	0.74	0.74	0.80±0.01	0.78±0.08	0.75	0.81	0.85[3]
500	0.82	0.83	0.86±0.01	0.9±0.1	0.83	0.88	0.86[3]
600	0.87	0.88	0.90±0.01	1.0±0.2	0.88	0.92	0.87[3]
700	0.91	0.91	0.92±0.01	1.0±0.2	0.92	0.95	0.88[3]

[1] Ref. [164]
[2] Ref. [160]
[3] Values taken from Ref. [179].

Table 4.6: Kinetic isotope effect $\cdot\mathrm{CH_3} + \mathrm{HD}/\cdot\mathrm{CH_3} + \mathrm{DH}$.

T (K)	TST	TST+Wigner	QI		TST[1]	CVT/μOMT[1]	Expt.[2]
			accel.	std.			
467	1.51	1.86	2.10±0.02	2.5±0.4	1.50	1.83	2.1±0.5[3]
531	1.48	1.76	1.84±0.02	2.0±0.3	1.47	1.71	1.9±0.3[3]
650	1.44	1.64	1.59±0.02	1.4±0.3	1.43	1.56	1.2±0.3[3]

[1] Ref. [164]
[2] Ref. [160]
[3] Values taken from Ref. [179].

Table 4.7: Kinetic isotope effect $\cdot CD_3 + HD / \cdot CD_3 + DH$.

T (K)	TST	TST+Wigner	QI		TST[1]	CVT/μOMT[1]	Expt.[2]
			accel.	std.			
400	1.56	1.99	2.52±0.02	2.3±0.3	1.55	1.91	1.85[3]
500	1.50	1.80	1.95±0.02	1.9±0.3	1.49	1.60	1.61[3]
600	1.46	1.68	1.65±0.02	1.3±0.3	1.45	1.56	1.47[3]
700	1.43	1.60	1.52±0.01	1.6±0.3	1.42	1.49	1.38[3]

[1] Ref. [164]

[2] Ref. [160]

[3] Values taken from Ref. [164].

Table 4.8: Kinetic isotope effect $\cdot CD_3 + H_2 / \cdot CD_3 + D_2$.

T (K)	TST	TST+Wigner	QI		TST[1]	CVT/μOMT[1]	Expt.[2]
			accel.	std.			
400	3.45	4.39	5.60±0.04	5.0±0.8	3.22	4.13	3.33[3]
500	2.98	3.57	3.92±0.03	3.9±0.5	2.83	3.21	2.88[3]
600	2.64	3.04	3.15±0.03	2.6±0.6	2.54	2.73	2.61[3]
700	2.40	2.68	2.75±0.02	2.5±0.4	2.33	2.43	2.43[3]

[1] Ref. [164]

[2] Ref. [160]

[3] Values taken from Ref. [164].

Table 4.9: Kinetic isotope effect $\cdot CH_3 + H_2 / \cdot CH_3 + D_2$.

T (K)	TST	TST+Wigner	QI		TST[1]	CVT/μOMT[1]	Expt.[2]
			accel.	std.			
400	3.45	4.41	5.93±0.05	5.8±0.8	3.22	4.57	4.8±0.4[3]
500	2.97	3.58	4.09±0.04	4.0±0.6	2.83	3.43	3.5±0.2[3]
600	2.64	3.05	3.21±0.03	3.1±0.5	2.54	2.86	2.8±0.2[3]

[1] Ref. [164]

[2] Ref. [160]

[3] Values taken from Ref. [179].

affecting the transferred atom (see Tables 4.3-4.5) the quantum instanton values are close to those obtained by conventional TST. This can be understood qualitatively from the expression (1.10) for Wigner tunneling correction for reaction rates. The main contribution to $\mu^{\ddagger}$ appearing in the expression for $\omega^{\ddagger}$ comes from the transferred atom, therefore if its mass does not change, the Wigner tunneling corrections for different isotopologues will have similar values and largely cancel out in the kinetic isotope effect.

Second, note that, in agreement with the usual difference in magnitudes of secondary and primary isotope effects, replacing $\cdot\mathrm{CH_3}$ with $\cdot\mathrm{CD_3}$ leads to a much smaller rate change than does replacing $\mathrm{H_2}$ with $\mathrm{D_2}$ (compare Tables 4.4-4.5 and 4.8-4.9) This consideration also explains why the kinetic isotope effects corresponding to $\cdot\mathrm{CH_3}+\mathrm{H_2}/\cdot\mathrm{CH_3}+\mathrm{D_2}$ and $\cdot\mathrm{CD_3}+\mathrm{H_2}/\cdot\mathrm{CD_3}+\mathrm{D_2}$ are quite close to each other (see Tables 4.9 and 4.8). For some kinetic isotope effects presented in Tables 4.7-4.9 it appears that results obtained with TST or TST with Wigner tunneling correction are in better agreement with experimental values than those obtained with the quantum instanton, probably indicating that a large cancellation takes place between the errors of the TST and of the potential energy surface (PES).

In order to estimate the influence of the used force field on the final result we also ran calculations with the PES published in Ref. [6] for $\mathrm{CH_4}+\cdot\mathrm{H}/\mathrm{CH_4}+\cdot\mathrm{D}$. As was the case with the force field in Ref. [7], this PES was obtained by fitting *ab initio* data, however in this case the hydrogens inside methane are equivalent to each other, but not to the abstracted hydrogen atom. After finding the optimal dividing surfaces' positions (see Table G.2 in Appendix G), we compared the quantum instanton values of this kinetic isotope effect obtained with the two PES's from Refs. [6] and [7] (see Table 4.10), finding that the choice of the PES affects the kinetic isotope effect value by as much as 10%. In contrast, comparison of the kinetic isotope effects computed with the same PES, but with two different accurate quantum methodologies [ring polymer molecular dynamics (RPMD) and quantum instanton] results in a remarkable agreement, within the statistical error of less than 2%. Finally, note that the quantum instanton kinetic isotope effect is in much better agreement with experiment if computed with the PES of Ref. [7] than with the PES of Ref. [6], suggesting that the former PES, which was used for most of the calculations in this paper, was the appropriate choice.

As for the performance of the fourth-order splittings, since an analytical gradient was not available for the $\mathrm{CH_4}+\cdot\mathrm{H}$ system, the gradient had to be calculated numerically using finite differences. For constrained simulations this made the force twelve times (once per each internal degree of freedom) as expensive as the potential itself, leading to a seven-fold increase in CPU time for a given P and number of Monte Carlo steps when the Suzuki-Chin splitting was used. Since the fourth-order splitting decreased the necessary P by a factor of four, the final increase in CPU time for a given discretization error and number of Monte Carlo steps was 75%. For unconstrained simulations employed to find $\cdot\mathrm{CH_3}/\cdot\mathrm{CD_3}$ equilibrium isotope effect the force was six times as expensive as the potential; since the use of the TI factorization allowed to decrease P four times, the final increase in CPU time

Table 4.10: Influence of the potential energy surface (PES) on the kinetic isotope effect $CH_4 + \cdot H/CH_4 + \cdot D$. Comparison of the quantum instanton (QI) kinetic isotope effects calculated using the PES's of Refs. [6] and [7]. Note also the remarkable agreement between the kinetic isotope effects computed with ring polymer molecular dynamics (RPMD) and QI on the same PES.

T (K)	PES of Ref. [6]				PES of Ref. [7]	Expt.[2]
	TST	TST+Wigner	RPMD[1]	QI	QI	
400	0.52	0.52		0.54±0.01	0.60±0.01	0.74[3]
500	0.63	0.63	0.65	0.64±0.01	0.70±0.01	0.84[3]
600	0.71	0.71		0.73±0.01	0.78±0.01	0.91[3]
700	0.77	0.77	0.80	0.79±0.01	0.84±0.01	0.97[3]

[1] Ref. [166]

[2] Ref. [159]

[3] Values taken from Ref. [164].

was also 75% for a given number of Monte Carlo steps and discretization error.

In summary, the kinetic isotope effects were reproduced in a reasonable agreement with experiment. The differences are probably due to both the error of the potential energy surface used and the large experimental error. Note that our accelerated methodology again drastically reduced both the discretization and statistical errors of the calculations.

4.5 Conclusions

In conclusion, we have accelerated the methodology from Ref. [111] for computing kinetic isotope effects with the quantum instanton approximation. In particular, we have combined virial estimators (several of which have been derived for the first time here) with high-order factorizations of the quantum Boltzmann operator, and shown that this combination significantly accelerates the quantum instanton calculations of the kinetic isotope effects in systems with prominent quantum effects. We have also proposed and demonstrated the utility of a new method for the thermodynamic integration of the delta-delta correlation function C_{dd}, which is a convenient alternative to the approach employed in Ref. [111]. Our accelerated methodology has been tested on the $CH_4 + \cdot H \rightleftharpoons \cdot CH_3 + H_2$ model exchange, obtaining results that agree reasonably well with published experimental values.

We must note that since the publication of the results presented in this chapter [117] we have introduced a more convenient procedure to optimize the necessary dividing surfaces, namely by running an adaptive biasing force [130–132] calculation that reconstructs dependence of C_{dd} on $\{\eta_\gamma^\ddagger\}$ using the virial estimators of derivatives of C_{dd} with respect to $\eta_\gamma^\ddagger$ (4.49). This modification of the method was used in Ref. [180].

In this work we did not discuss integration error of thermodynamic integration with respect to mass, which contrasts our treatment of equilibrium isotope effect calculations in the previous chapters; this is mainly due to our focus on other types of errors at the time this work was performed. The approaches of Chapters 2 and 3 can be trivially extended to the problem of calculating the ratio of delta-delta correlation functions corresponding to different particles' masses, *but* to the same dividing surfaces; the main difference would be that while evaluating the corresponding direct estimators or performing the mass-scaled Monte Carlo moves we would need to rescale $\mathrm{r}_i^{(s)} - \check{\mathrm{r}}_i^{(s)}$ with mass rather than $\mathrm{r}_i^{(s)} - \mathrm{r}_i^{(C)}$. This extension, however, is no longer possible once the positions of the dividing surfaces change with changing masses. A possible way to bypass the problem could be to calculate the ratio $C_{\mathrm{dd}}^{(1)}/C_{\mathrm{dd}}^{(0)}$ with both dividing surfaces placed on top of the reaction barrier, and then run two adaptive biasing force calculations to find dependence of C_{dd} on the dividing surfaces' positions for the two isotopologues. The latter two calculations would combine finding dividing surfaces' positions optimal for the quantum instanton calculation with accounting for not using these dividing surfaces during thermodynamic integration; they can be made relatively cheap as for each isotopologue they would only need to cover a range of dividing surfaces that includes the point corresponding to both dividing surfaces being on top of the reaction barrier and the (estimated position of the) saddle point of C_{dd}. Such a combined approach may introduce additional statistical errors to the calculation, but is still a possibly more convenient alternative to the method used in this work and therefore should be investigated in the future.

5 Limitations of quantum instanton approximation

5.1 Introduction

The results presented in this chapter are currently being prepared for publication.

The original goal of the work presented in this chapter was to propose a way to correct the wrong high-temperature limit of the quantum instanton approximation, and to that end we considered the closely related Hansen-Andersen transition state theory [4, 5], which agrees with classical transition state theory in the high temperature limit, but was found to exhibit large errors at low temperatures for asymmetric barriers. Since Hansen-Andersen transition state theory involves choosing a single dividing surface that minimizes the flux-flux correlation function, and quantum instanton approximation has been shown to be less accurate if a single dividing surface is used [3], using two dividing surfaces instead of one for a Hansen-Andersen calculation is a logical way to improve on the method's performance and obtain a quantum instanton-like method that would have the correct high temperature limit. Unfortunately, we have found that while the resulting new method does improve performance of Hansen-Andersen transition state theory in some cases, it does not solve its problem with asymmetric barriers at low temperatures. In this case, we have found that neither the new approach, nor quantum instanton approximation can give an accuracy comparable to the one of ring polymer molecular dynamics. The implications of these results are summarized in Sec. 5.6.

5.2 An alternative derivation of the quantum instanton approximation

While presenting the quantum instanton formalism of Ref. [111] in Sec. 4.2, we noted that it does not explain why the quantum instanton approximation can be accurate in situations where $C_{\mathrm{ff}}(t)/C_{\mathrm{dd}}(t)$ changes drastically in the neighborhood of $t=0$, a situation we will encounter in Sec. 5.5. We therefore present an alternative derivation that largely follows the philosophy of Ref. [3], but which we find to employ more intuitive approximations than the original one. In the spirit of the quantum instanton derivation of Ref. [3] we will also consider systems where reaction coordinate is separable.

We now introduce reaction coordinates that depend on time as a parameter and have the form

$$\tilde{\xi}_\gamma(\mathbf{r},t)=\xi(\mathbf{r})-\tilde{\eta}_\gamma(t)-\eta^\ddagger_\gamma, \tag{5.1}$$

where $\xi(\mathbf{r})$ is a standard reaction coordinate. For a fixed t, $\tilde{\xi}_\gamma(\mathbf{r},t)=0$ ($\gamma\in\{a,b\}$) defines two dividing surfaces, and we choose $\tilde{\eta}_\gamma(t)$ to be such that at $\eta^\ddagger_\gamma=0$ these two dividing surfaces satisfy

$$\int\left\langle\nabla\xi(\mathbf{r}_{\gamma'}),\frac{\partial}{\partial\mathbf{r}_{\gamma'}}\right\rangle\langle\mathbf{r}_a|e^{-\beta^+\hat{H}/2}|\mathbf{r}_b\rangle\prod_{\gamma=a,b}\Delta_\gamma(\mathbf{r}_\gamma)d\mathbf{r}_\gamma=0 \tag{5.2}$$

for each $\gamma'\in\{a,b\}$. Note that for a separable reaction coordinate, at $t=0$ Eq. (5.2) will be equivalent to $C_{\mathrm{dd}}(0)$ being stationary with respect to dividing surfaces' positions. As will be discussed properly in Appendix H, we can also write

$$C_{\mathrm{ff}}(t)=\frac{\hbar^2}{4m^\ddagger}\frac{\partial^2C_{\mathrm{dd}}(t)}{\partial\eta^\ddagger_a\partial\eta^\ddagger_b}, \tag{5.3}$$

where $m^\ddagger$ is the mass corresponding to motion along the reaction coordinate, as was mentioned in Sec. (1.3). The choice for $\tilde{\eta}_\gamma(t)$ is not unique, but it is possible to define the functions in a way that makes them continuous and differentiable. It is reasonable to assume that $\tilde{\eta}_\gamma(t)$ is bound, a fact that can be easily proven for a separable reaction coordinate case if one assumes that $\langle\nabla\xi(\mathbf{r}),\nabla V(\mathbf{r})\rangle_-=0$ for all $|\xi(\mathbf{r})|$ above some "cutoff" value. Also note that $\tilde{\eta}_\gamma(t)$ is an even function of time, which can be verified by taking the conjugate of Eq. (5.2). Let us now consider the following equation which is equivalent [54] to Miller-Schwartz-Tromp formula (1.16)

$$k=\frac{1}{Q_r}\lim_{t\to\infty}C_{\mathrm{fs}}(t), \tag{5.4}$$

where $C_{\mathrm{fs}}(t)$ is the flux-side correlation function

$$C_{\mathrm{fs}}(t):=\mathrm{Tr}\{\hat{F}_a e^{-(\beta/2-\mathrm{i}t/\hbar)\hat{H}}h[\xi_b(\hat{\mathbf{r}})]e^{-(\beta/2+\mathrm{i}t/\hbar)\hat{H}}\}. \tag{5.5}$$

$C_{\mathrm{fs}}(t)$ is an odd function of t and, since its time derivative $C_{\mathrm{ff}}(t)$ is invariant with respect to permutation of the two dividing surfaces, $C_{\mathrm{fs}}(t)$ is invariant to permutation of the two dividing surfaces as well. We now consider $C_{\mathrm{fs}}[t,\{\tilde{\eta}_\gamma(t)\}]$ which is $C_{\mathrm{fs}}(t)$ corresponding to dividing surfaces set by $\tilde{\xi}_\gamma(\mathbf{r},t)=0$. Since the limit appearing in Eq. (5.4) does not depend on dividing surfaces' positions and we assume that $\tilde{\eta}_\gamma(t)$ is a bound function, then

$C_{\mathrm{fs}}[t,\{\tilde{\eta}_\gamma(t)\}]$ should also exhibit a limiting behavior given by

$$k = \frac{1}{Q_r} \lim_{t\to\infty} C_{\mathrm{fs}}[t,\{\tilde{\eta}_\gamma(t)\}]. \tag{5.6}$$

We now proceed to rewrite Eq. (5.6) in a way analogous to the Miller-Schwartz-Tromp formula (1.16)

$$\begin{aligned} k &= \frac{1}{2Q_r} \int_{-\infty}^{\infty} \frac{dC_{\mathrm{fs}}[t,\{\tilde{\eta}_\gamma(t)\}]}{dt} dt \\ &= \frac{1}{2Q_r} \int_{-\infty}^{\infty} \tilde{C}_{\mathrm{ff}}(t) dt, \end{aligned} \tag{5.7}$$

where we introduced $\tilde{C}_{\mathrm{ff}}(t)$ as

$$\tilde{C}_{\mathrm{ff}}(t) := \frac{dC_{\mathrm{fs}}[t,\{\tilde{\eta}_\gamma(t)\}]}{dt} \tag{5.8}$$

$$= \frac{\partial C_{\mathrm{fs}}[t,\{\tilde{\eta}_\gamma(t)\}]}{\partial t} + \sum_{\gamma=a,b} \frac{\partial \tilde{\eta}_\gamma(t)}{\partial t} \frac{\partial C_{\mathrm{fs}}[t,\{\tilde{\eta}_\gamma(t)\}]}{\partial \tilde{\eta}_\gamma}. \tag{5.9}$$

Let us now consider the behavior of $\partial C_{\mathrm{fs}}[t,\{\tilde{\eta}_\gamma(t)\}]/\partial \eta_\gamma$ as $t \to 0$. Since flux-side function is an odd function of time, while $\{\tilde{\eta}_\gamma(t)\}$ is even, $\partial C_{\mathrm{fs}}[t,\{\tilde{\eta}_\gamma(t)\}]/\partial \eta_\gamma$ should be an odd function of time as well. Its time derivative equals

$$\frac{d}{dt} \frac{\partial C_{\mathrm{fs}}[t,\{\tilde{\eta}_\gamma(t)\}]}{\partial \tilde{\eta}_\gamma} = \frac{\partial^2 C_{\mathrm{fs}}[t,\{\tilde{\eta}_\gamma(t)\}]}{\partial t \partial \tilde{\eta}_\gamma} + \sum_{\gamma'=a,b} \frac{\partial \tilde{\eta}_{\gamma'}(t)}{\partial t} \frac{\partial^2 C_{\mathrm{fs}}[t,\{\tilde{\eta}_\gamma(t)\}]}{\partial \tilde{\eta}_\gamma \partial \tilde{\eta}_{\gamma'}}. \tag{5.10}$$

Since $\tilde{\eta}_\gamma(t)$ is an even function of time $d\tilde{\eta}_{\gamma'}(t)/dt|_{t=0} = 0$, resulting in

$$\frac{\partial C_{\mathrm{fs}}[t,\{\tilde{\eta}_\gamma(t)\}]}{\partial \tilde{\eta}_\gamma} = \frac{\partial^2 C_{\mathrm{fs}}[t,\{\tilde{\eta}_\gamma(t)\}]}{\partial t \partial \tilde{\eta}_\gamma} t + \mathcal{O}(t^3). \tag{5.11}$$

We now combine Eqs. (5.3), (5.9), and (5.11) to obtain

$$\begin{aligned} \tilde{C}_{\mathrm{ff}}(t) :=& \frac{dC_{\mathrm{fs}}[t,\{\tilde{\eta}_\gamma(t)\}]}{dt} \\ =& C_{\mathrm{ff}}[t,\{\tilde{\eta}_\gamma(t)\}] + \sum_{\gamma=a,b} \frac{\partial \tilde{\eta}_\gamma(t)}{\partial t} \frac{\partial C_{\mathrm{ff}}[t,\{\tilde{\eta}_\gamma(t)\}]}{\partial \tilde{\eta}_\gamma} t + \mathcal{O}(t^4) \\ =& \frac{\hbar^2}{4m^\ddagger} \frac{\partial^2}{\partial \eta_a^\ddagger \partial \eta_b^\ddagger} \left\{ C_{\mathrm{dd}}[t,\{\tilde{\eta}_\gamma(t)\}] + \sum_{\gamma=a,b} \frac{\partial \tilde{\eta}_\gamma(t)}{\partial t} \frac{\partial C_{\mathrm{dd}}[t,\{\tilde{\eta}_\gamma(t)\}]}{\partial \tilde{\eta}_\gamma} t \right\} + \mathcal{O}(t^4), \end{aligned} \tag{5.12}$$

where $C_{\mathrm{ff}}[t,\{\tilde{\eta}_\gamma(t)\}]$ and $C_{\mathrm{dd}}[t,\{\tilde{\eta}_\gamma(t)\}]$ are the flux-flux and delta-delta correlation functions corresponding to dividing surfaces set by $\tilde{\xi}_\gamma(\mathbf{r},t) = 0$. For brevity, we rewrite the expression as

$$\tilde{C}_{\mathrm{ff}}(t) = \frac{\hbar^2}{4m^\ddagger} \frac{\partial^2 \tilde{C}_{\mathrm{dd}}(t)}{\partial \eta_a^\ddagger \partial \eta_b^\ddagger}, \tag{5.13}$$

where we introduced

$$\tilde{C}_{\mathrm{dd}}(t)=C_{\mathrm{dd}}[t,\{\tilde{\eta}_\gamma(t)\}]+\sum_{\gamma=a,b}\frac{\partial\tilde{\eta}_\gamma(t)}{\partial t}\frac{\partial C_{\mathrm{dd}}[t,\{\tilde{\eta}_\gamma(t)\}]}{\partial\tilde{\eta}_\gamma}t+\mathcal{O}(t^4). \tag{5.14}$$

The nature of the $\mathcal{O}(t^4)$ term is irrelevant for the following discussion, we just need to note that

$$\begin{aligned}\tilde{C}_{\mathrm{dd}}(t)=&C_{\mathrm{dd}}[t,\{\tilde{\eta}_\gamma(t)\}]+\sum_{\gamma=a,b}\frac{\partial\tilde{\eta}_\gamma(t)}{\partial t}\frac{\partial C_{\mathrm{dd}}[t,\{\tilde{\eta}_\gamma(t)\}]}{\partial\tilde{\eta}_\gamma}t+\mathcal{O}(t^4)\\ =&C_{\mathrm{dd}}[t,\{\tilde{\eta}_\gamma(0)\}]+\sum_{\gamma=a,b}\frac{\partial\tilde{\eta}_\gamma(t)}{\partial t}\\ &\times\left\{\frac{\partial C_{\mathrm{dd}}[t,\{\tilde{\eta}_\gamma(t)\}]}{\partial\tilde{\eta}_\gamma}+\frac{\partial C_{\mathrm{dd}}[t,\{\tilde{\eta}_\gamma(0)\}]}{\partial\tilde{\eta}_\gamma}\right\}t+\mathcal{O}(t^4)\\ =&C_{\mathrm{dd}}[t,\{\tilde{\eta}_\gamma(0)\}]+\mathcal{O}(t^4).\end{aligned} \tag{5.15}$$

In the last equality we used that $\tilde{C}_{\mathrm{dd}}(t)$ is an even function of time, and that all terms besides $C_{\mathrm{dd}}[t,\{\tilde{\eta}_\gamma(0)\}]$ appear to be at least $\mathcal{O}(t^3)$ due to stationarity of $C_{\mathrm{dd}}[0,\{\tilde{\eta}_\gamma(0)\}]$ with respect to dividing surfaces' positions.

Combining Eqs. (5.7) and (5.13) yields

$$\begin{aligned}k&=\frac{1}{2Q_r}\int_{-\infty}^{\infty}\frac{\hbar^2}{4m^\ddagger}\frac{\partial^2\tilde{C}_{\mathrm{dd}}(t)}{\partial\eta_a^\ddagger\partial\eta_b^\ddagger}dt\\ &=\frac{1}{2Q_r}\frac{\hbar^2}{4m^\ddagger}\frac{\partial^2}{\partial\eta_a^\ddagger\partial\eta_b^\ddagger}\int_{-\infty}^{\infty}\tilde{C}_{\mathrm{dd}}(t)dt.\end{aligned} \tag{5.16}$$

Evaluating the integral with steepest descent and keeping in mind Eq. (5.15), which implies that $d^2\tilde{C}_{\mathrm{dd}}(t)/dt^2|_{t=0}=d^2C_{\mathrm{dd}}(t)/dt^2|_{t=0}$, leads to

$$\begin{aligned}k&\approx\frac{\sqrt{\pi}}{2Q_r}\frac{\hbar^2}{4m^\ddagger}\frac{\partial^2}{\partial\eta_a^\ddagger\partial\eta_b^\ddagger}\frac{C_{\mathrm{dd}}(0)}{\sqrt{\ddot{C}_{\mathrm{dd}}(0)/C_{\mathrm{dd}}(0)/2}}\\ &=\frac{\hbar\sqrt{\pi}}{2Q_r}\frac{\hbar^2}{4m^\ddagger}\frac{\partial^2}{\partial\eta_a^\ddagger\partial\eta_b^\ddagger}\frac{C_{\mathrm{dd}}(0)}{\Delta H}\end{aligned} \tag{5.17}$$

The last step is to compare path integral expressions for $C_{\mathrm{dd}}(0)$ [Eq. (1.53)] and ΔH [Eqs. (4.39) and (4.40)]. Since $C_{\mathrm{dd}}(0)$ depends exponentially on the potential it is reasonable to assume that it would change much more drastically with dividing surfaces' positions than ΔH, an assumption that should be especially accurate for low temperatures. Assuming ΔH to be almost stationary and using Eq. (5.3) after differentiating $C_{\mathrm{dd}}(0)$ with respect to the dividing surfaces' positions one obtains the quantum instanton expression for the rate constant (4.2).

Last but not the least, we already mentioned that for Eq. (5.2) to hold at $t=0$ we should choose dividing surfaces that make $C_{\mathrm{dd}}(0)$ stationary with respect to their positions. We also recall that of all factors appearing in Eq. (4.2) $C_{\mathrm{dd}}(0)$ changes most drastically with dividing surfaces; therefore, if we choose $C_{\mathrm{dd}}(0)$ to be a minimum with respect to dividing surfaces' positions then k_{QI} would be a minimum as well, thus minimizing recrossing contributions to the calculated reaction rate. We also note that the Miller-Schwartz-Tromp formula (1.16) suggests that the integral of $C_{\mathrm{ff}}(t)$ does not depend on dividing surfaces' positions; if we assume that $C_{\mathrm{ff}}(t)$ is close to a Gaussian with a maximum at $t = 0$, then the larger $C_{\mathrm{ff}}(0)$ is the sharper is the maximum. Therefore, maximizing $C_{\mathrm{ff}}(0)$ should lead to a greater contribution of the $t = 0$ neighborhood to the integral over time in the Miller-Schwartz-Tromp formula (1.16); recalling the path integral expression for $C_{\mathrm{ff}}(0)/C_{\mathrm{dd}}(0)$ (4.45) we conclude that $C_{\mathrm{ff}}(0)$ will be close to a maximum if $C_{\mathrm{dd}}(0)$ is a maximum as well. As a result the optimal dividing surfaces should make $C_{\mathrm{dd}}(0)$ both a maximum and a minimum with respect to their positions, thus it should be a saddle point.

The weakest point of the derivation presented in this section is that it assumes separability of the reaction coordinate, which is necessary for Eq. (5.3) to hold. The authors of Ref. [3] encountered similar problems with their derivation, and they introduced additional approximations that allow to extend their result to the nonseparable case. We note that in the future it may be interesting to test how nonseparability of the reaction coordinate affects accuracy of the quantum instanton approximation, however in this work we focused on simple one-dimensional systems, and this derivation is for now sufficient without a proper multidimensional generalization.

5.3 Drawbacks of quantum instanton formalism and possible corrections

A major issue with the quantum instanton expression [Eq. (4.2)] is that in the high temperature limit its reaction rate is larger than the classical transition state theory result by a factor of $\sqrt{\pi/2}$ [3]. The reason for this disagreement is the limiting high temperature behavior of delta-delta and flux-flux correlation functions

$$\lim_{\beta\to 0}\frac{C_{\mathrm{ff}}(t)}{C_{\mathrm{ff}}(0)} = \frac{1}{\left[1+\left(\frac{2t}{\beta\hbar}\right)^2\right]^{3/2}}, \tag{5.18}$$

$$\lim_{\beta\to 0}\frac{C_{\mathrm{dd}}(t)}{C_{\mathrm{dd}}(0)} = \frac{1}{\sqrt{1+\left(\frac{2t}{\beta\hbar}\right)^2}} \tag{5.19}$$

(these limits are valid if the two dividing surfaces are merged, which is true for a quantum instanton calculation at high temperatures). Evidently, in this limit the integral of $C_{\mathrm{ff}}(t)$ appearing in the Miller-Schwartz-Tromp formula (1.16) exists, while the integral of $C_{\mathrm{dd}}(t)$ appearing in both quantum instanton derivations described above [Eqs. (4.1) and (5.16)] does not, making the successive algebra invalid.

Probably the only way to bypass the issue while still dealing with an integral over $C_{\mathrm{dd}}(t)$ is to separate dividing surfaces far enough from each other in order to make $C_{\mathrm{dd}}(t)$ decay faster, leading to the steepest descent approximation becoming more accurate [181]. Unfortunately, this approach also leads to the maximum of $C_{\mathrm{dd}}(t)$ being shifted from $t = 0$ to a certain t_{max}; as a result the steepest descent approximation no longer leads to a rate expression in terms of correlation functions at $t = 0$, making a Monte Carlo implementation of the method much more challenging. Alternatively, the following *ad hoc* expression was found to work well enough [3]

$$k_{\mathrm{QI,mod}} = \frac{\hbar\sqrt{\pi}}{2}\frac{C_{\mathrm{dd}}(0)}{Q_r}\frac{C_{\mathrm{ff}}(0)/C_{\mathrm{dd}}(0)}{\Delta H_{\mathrm{mod}}}, \tag{5.20}$$

where ΔH_{mod} is the modified ΔH_{QI}

$$\Delta H_{\mathrm{mod}} = \hbar\sqrt{-\frac{\ddot{C}_{\mathrm{dd}}(0)}{2C_{\mathrm{dd}}(0)}} + \frac{\sqrt{\pi}-\sqrt{2}}{\beta}. \tag{5.21}$$

Another way to avoid the problem is to evaluate Miller-Schwartz-Tromp formula (1.16) directly by estimating dependence of flux-flux correlation function on time. The first possible strategy is to evaluate $C_{\mathrm{ff}}(t)$ dependence for imaginary values of time and construct an analytic continuation into real time axis [182–185]; the second one, which we will focus on, involves reconstructing $C_{\mathrm{ff}}(t)$ from its value and derivatives at $t = 0$, which was shown to be theoretically possible in Ref. [186], provided an infinite number of derivatives is known. In practice, of course, one has to choose an approximate ansatz for $C_{\mathrm{ff}}(t)$, and the expression proposed in Ref. [59] reads

$$\frac{C_{\mathrm{ff}}(t)}{C_{\mathrm{ff}}(0)} \approx \exp\left\{-b_0 \ln\left[1+\left(\frac{2t}{\hbar\beta}\right)^2\right] - \sum_{l=1}^{L} b_l t^{2l}\right\}, \tag{5.22}$$

where b_l are coefficients determined from time derivatives $C_{\mathrm{ff}}^{(2n)}(0)/C_{\mathrm{ff}}(0)$ $(n \in Z; n \geq 1)$, that can be straightforwardly evaluated using path integral Monte Carlo or molecular dynamics [158]. The expression allows to smoothly interpolate between low-temperature behavior of $C_{\mathrm{ff}}(t)$ as a fast-decaying function and the high-temperature behavior given by Eq. (5.18), provided one calculates at least $C_{\mathrm{ff}}^{(2)}(0)/C_{\mathrm{ff}}(0)$ and $C_{\mathrm{ff}}^{(4)}(0)/C_{\mathrm{ff}}(0)$. The authors of Ref. [59] proposed to determine the optimal dividing surfaces by maximizing the highest order coefficient b_L, thus maximizing the contribution from the neighborhood of $t = 0$ to the integral over time in the Miller-Schwartz-Tromp formula (1.16) and making the steepest descent approximation as accurate as possible; the resulting method is often referred to as "extended quantum instanton approach."

5.4 Hansen-Andersen formalism and its modified version

The downside of using extended quantum instanton formalism is the necessity to deal with higher-order time derivatives of $C_{\mathrm{ff}}(t)$, which are quite expensive to calculate. A cheaper alternative that involves calculating just $\ddot{C}_{\mathrm{ff}}(0)$ is the Hansen-Andersen transition state theory [4, 5], which uses the following ansatz for $C_{\mathrm{ff}}(t)$

$$\frac{C_{\mathrm{ff}}(t)}{C_{\mathrm{ff}}(0)} \approx \frac{\exp(-\alpha t^2)}{\left[1+\left(\frac{2t}{\beta\hbar}\right)^2\right]^{3/2}}, \tag{5.23}$$

where α is evaluated as

$$\alpha = -\frac{\ddot{C}_{\mathrm{ff}}(0)}{2C_{\mathrm{ff}}(0)} - \frac{6}{\beta^2}. \tag{5.24}$$

The authors proposed to use a single dividing surface for both a and b, which should corresponds to a minimum of $C_{\mathrm{ff}}(0)$ in order to minimize recrossing contribution to the reaction rate. Several alternatives to Eq. (5.23) have also been proposed [5], but since all of them give similar results, in this work for the sake of simplicity we will only consider Eq. (5.23).

The deeper meaning of the ansatz (5.23) is that it accounts for behavior of $C_{\mathrm{ff}}(t)$ at imaginary time values, namely that, if the two dividing surfaces are merged, then one has [187]

$$\lim_{t\to\pm \mathrm{i}\beta\hbar/2} C_{\mathrm{ff}}(t) = \frac{c}{\left[1+\left(\frac{2t}{\beta\hbar}\right)^2\right]^{3/2}}, \tag{5.25}$$

where c is some constant.

In this work we decided to test whether the accuracy of Hansen-Andersen approximation can be improved by using dividing surfaces' positions that make $C_{\mathrm{ff}}(0)$ a saddle point rather than a minimum. The motivation is analogous to the argument made in Sec. 5.2: increasing $C_{\mathrm{ff}}(0)$ should make its maximum at $t = 0$ sharper, thus making the neighborhood of $t = 0$ contribute more to the time integral in Miller-Schwartz-Tromp formula (1.16). If the dividing surfaces are split, however, $C_{\mathrm{ff}}(t)$ no longer obeys Eq. (5.25), thus making the ansatz (5.23) invalid. However, even if Eq. (5.23) is incorrect, the integral of the resulting approximate $C_{\mathrm{ff}}(t)$ over t still yields a valid approximation to the reaction rate. This can be shown using algebra which is analogous to the one as in Sec. 5.2, but follows $\tilde{\tilde{\eta}}_{\gamma}(t)$ that make $C_{\mathrm{ff}}(t)$ a saddle point with respect to dividing surfaces' positions. The argument is straightforward, but also quite lengthy, and therefore was left for Appendix I.

5.5 Numerical tests

The calculations presented in this section were done with the Eckart barrier [188], which is a model one-dimensional system characterized by the following potential

$$V_{\mathrm{eck}}(x) = \frac{V_1 - V_2}{1+\exp(-2\pi x/\Delta)} + \frac{(V_1^{1/2}+V_2^{1/2})^2}{4\cosh^2(\pi x/\Delta)}, \tag{5.26}$$

where V_1, V_2 and Δ are parameters that specify the barrier and x is the particle's coordinate. The barrier exhibits a maximum at $x_{\mathrm{max}} = \Delta \ln(V_1/V_2)/(4\pi)$ with $V_{\mathrm{eck}}(x_{\mathrm{max}}) = V_1$; if $x \to -\infty$ corresponds to the reactant region then the classical activation energy is V_1, otherwise it is V_2. We will consider the tunneling correction Γ defined as the ratio of classical and quantum reaction rates

$$\Gamma = \frac{k_{\text{quantum}}}{k_{\text{classical}}}, \tag{5.27}$$

which for the Eckart barrier can be shown to depend on just three dimensionless parameters [5]

$$\xi = \frac{\pi\beta\hbar}{\Delta(V_1^{1/2} + V_2^{1/2})}\sqrt{\frac{8V_1V_2}{m}}, \tag{5.28}$$

$$\alpha_1 = \frac{2\pi\beta V_1}{\xi}, \tag{5.29}$$

$$\alpha_2 = \frac{2\pi\beta V_2}{\xi}, \tag{5.30}$$

where m is the mass of the particle. The parameter ξ is often rewritten as $\beta\hbar|\omega^\ddagger|$, where $\omega^\ddagger$ is the imaginary frequency corresponding to movement along the reaction coordinate on top of the reaction barrier. An important property of the system is that the exact quantum reaction rate constant can be obtained with the one-dimensional version of the exact reaction rate expression (1.14)

$$k_{\text{QM}} = \frac{1}{2\pi\hbar Q_r}\int_0^{+\infty} N(E)\exp(-\beta E)\mathrm{d}E, \tag{5.31}$$

where $N(E)$ is the transition probability, which is available analytically from Ref. [188]

$$N(E) = \frac{\cosh[2\pi(a+b)] - \cosh[2\pi(a-b)]}{\cosh[2\pi(a+b)] + \cosh[2\pi c]}, \tag{5.32}$$

$$a = \frac{\Delta}{\pi}\sqrt{\frac{(E - V_1 + V_2)m}{2}}, \tag{5.33}$$

$$b = \frac{\Delta}{\pi}\sqrt{\frac{Em}{2}}, \tag{5.34}$$

$$c = \frac{1}{2}\sqrt{\frac{2m\Delta^2(V_1^{1/2} + V_2^{1/2})^2}{\hbar^2\pi^2} - 1}. \tag{5.35}$$

In this work we ran calculations for two Eckart barriers that have been widely used as benchmark systems for rate calculations: a symmetric Eckart barrier with $\alpha_1 = \alpha_2 = 12$ and an asymmetric one with $\alpha_1 = 12$ and $\alpha_2 = 48$, with temperature being changed via ξ.

5.5.1 Symmetric barrier performance

Relative errors of reaction rates obtained with quantum instanton approximation, as well as Hansen-Andersen transition state theory and its modified version, are plotted in Fig. 5.1. For quantum instanton approximation, one can see the characteristic ~20% error mentioned in Sec. 5.3 appearing in the high temperature limit; at lower temperatures, however, the

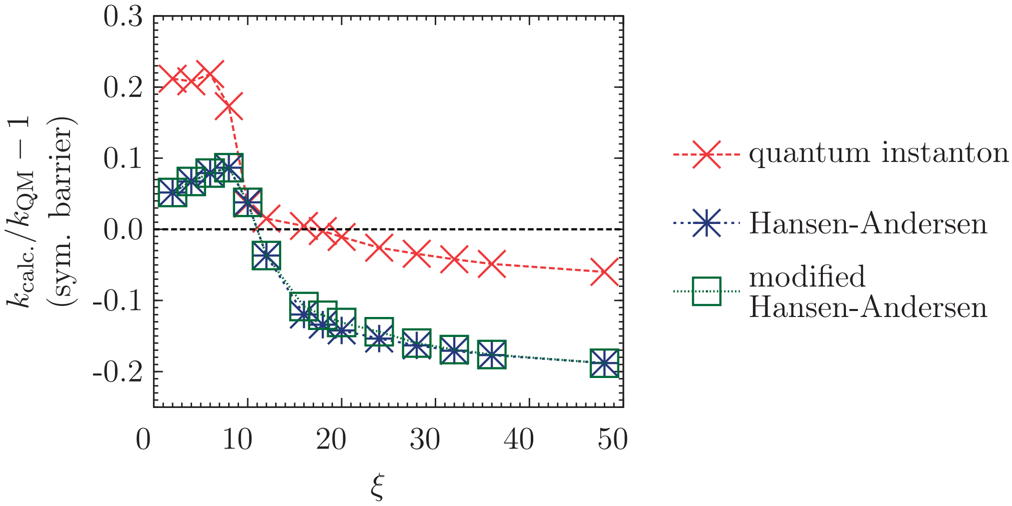

Figure 5.1: Errors of symmetric Eckart barrier ($\alpha_1 = \alpha_2 = 12$) reaction rates, denoted $k_{\mathrm{calc.}}$, calculated with quantum instanton approximation [3], as well as Hansen-Andersen transition state theory [4, 5] and its modified version proposed in this work. The exact rate k_{QM} was obtained from Eq. (5.31).

method demonstrates remarkable accuracy. Interestingly, for $\xi > 18$ we observed $\ddot{C}_{\mathrm{ff}}(t)$ to be positive for the choice of dividing surfaces used in a quantum instanton calculation, indicating that in this case $C_{\mathrm{ff}}(t)$ is no longer a maximum with respect to time. $\ddot{C}_{\mathrm{dd}}(t)$, however, was still negative; as a result one cannot assume $C_{\mathrm{ff}}(t)/C_{\mathrm{dd}}(t)$ to be approximately constant over the neighborhood of $t = 0$ that contributes most to the integral in Miller-Schwartz-Tromp formula (1.16). This observation was our main motivation for introducing quantum instanton derivation in Sec. 5.2 as an alternative to the derivation of Ref. [111] outlined in Sec. 4.2.

For Hansen-Andersen transition state theory and its modified version we observe that both methods give identical results for ξ as large as 12; as expected we can see that both approaches exhibit the correct high temperature limit. For larger ξ the dividing surfaces are split for modified Hansen-Andersen formalism, and the method becomes slightly more accurate than standard Hansen-Andersen transition state theory for a range of ξ values; however in the low temperature limit both methods yield almost identical reaction rates. The latter phenomenon is due to a surprising fact that for low temperatures both $C_{\mathrm{ff}}(0)$ and $\ddot{C}_{\mathrm{ff}}(0)$ did not change much with the choice of dividing surfaces. The differences in $C_{\mathrm{ff}}(0)$ and $\ddot{C}_{\mathrm{ff}}(0)$ also further canceled out, which is quite intuitive considering the invariance of the integral of $C_{\mathrm{ff}}(t)$ and the accuracy of short-time approximation at lower temperatures.

For reference, we present tunneling corrections obtained with the three methods in Tab. 5.1; we also compare them to values reported for ring polymer molecular dynamics and semiclassical instanton theory [75]. Both methods exhibit characteristic errors in the high temperature or low temperature limit; semiclassical instanton is extremely accurate in the low temperature limit, but cannot be used at temperatures above crossover temperature,

Table 5.1: Tunneling correction values [Eq. (5.27)] obtained for the symmetric Eckart barrier ($\alpha_1 = \alpha_2 = 12$). “SCI” stands for “semiclassical instanton.”

ξ	SCI[1]	QI	Hansen-Andersen		RPMD[2]	exact
			standard	modified		
2	_	1.48	1.29	_	1.9	1.22
4	_	2.50	2.21	_	2.7	2.07
6	_	6.33	5.61	_	4.4	5.20
8	$2.20\cdot10^{1}$	$2.55\cdot10^{1}$	$2.36\cdot10^{1}$	_	17	$2.18\cdot10^{1}$
10	$1.36\cdot10^{2}$	$1.68\cdot10^{2}$	$1.68\cdot10^{2}$	_	100	$1.62\cdot10^{2}$
12	$1.61\cdot10^{3}$	$2.00\cdot10^{3}$	$1.90\cdot10^{3}$	_	1100	$1.97\cdot10^{3}$
16	$6.04\cdot10^{5}$	$7.44\cdot10^{5}$	$6.52\cdot10^{5}$	$6.60\cdot10^{5}$	_	$7.40\cdot10^{5}$
18	$1.54\cdot10^{7}$	$1.88\cdot10^{7}$	$1.63\cdot10^{7}$	$1.66\cdot10^{7}$	_	$1.88\cdot10^{7}$
20	$4.37\cdot10^{8}$	$5.29\cdot10^{8}$	$4.58\cdot10^{8}$	$4.64\cdot10^{8}$	_	$5.34\cdot10^{8}$
24	$4.43\cdot10^{11}$	$5.24\cdot10^{11}$	$4.55\cdot10^{11}$	$4.60\cdot10^{11}$	_	$5.37\cdot10^{11}$
28	$5.44\cdot10^{14}$	$6.32\cdot10^{14}$	$5.48\cdot10^{14}$	$5.50\cdot10^{14}$	_	$6.55\cdot10^{14}$
32	$7.55\cdot10^{17}$	$8.63\cdot10^{17}$	$7.47\cdot10^{17}$	$7.48\cdot10^{17}$	_	$9.00\cdot10^{17}$
36	$1.14\cdot10^{21}$	$1.28\cdot10^{21}$	$1.11\cdot10^{21}$	$1.11\cdot10^{21}$	_	$1.34\cdot10^{21}$
48	$5.25\cdot10^{30}$	$5.60\cdot10^{30}$	$4.84\cdot10^{30}$	$4.84\cdot10^{30}$	_	$5.96\cdot10^{30}$

[1] Using the formula presented in Ref. [66].

[2] Ref. [75]

while ring polymer molecular dynamics agrees with classical transition state theory in the high temperature limit, but also exhibits a limiting error at low temperatures [75].

5.5.2 Asymmetric barrier performance

Relative errors of reaction rates obtained with the quantum instanton approximation, as well as Hansen-Andersen transition state theory and its modified version, are plotted in Fig. 5.2. For reference, the plotted values are also presented in Tab. 5.2. Behavior of all three methods in the high temperature limit is analogous to the one observed for the symmetric Eckart barrier; in the low temperature limit, however, we can see that all three methods exhibit large errors, a notion already reported for Hansen-Andersen transition state theory [5]. The apparent reason for this is that for all values of ξ the dividing surfaces used by all three methods ended up being chosen on one side of the reaction barrier, and the lower the temperature was the deeper they moved into the reactant region corresponding to higher potential energy; this must have led to a large recrossing contribution. Splitting of dividing surfaces was not observed for modified Hansen-Andersen transition state theory, consequently the method yielded results identical to the ones of standard Hansen-Andersen approach.

Similar problems for asymmetric barriers have been reported for several other transition state theories [69, 71, 189]; for the Voth-Chandler-Miller transition state theory [69] the issue has been discussed extensively in Ref. [75] and has led the authors to conclude that if a path-integral based transition state theory involves defining a dividing surface that depends on just the centroid, then it would break down for asymmetric barriers in the

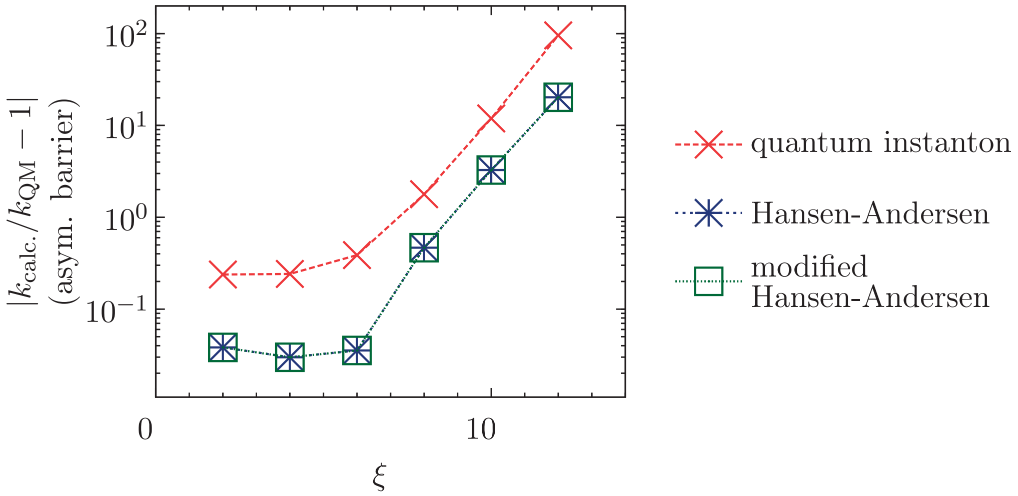

Figure 5.2: Errors of asymmetric Eckart barrier ($\alpha_1 = 12$, $\alpha_2 = 48$) reaction rates, denoted $k_{\mathrm{calc.}}$, calculated with quantum instanton approximation [3], as well as Hansen-Andersen transition state theory [4, 5] and its modified version proposed in this work. The exact rate k_{QM} was obtained from Eq. (5.31).

Table 5.2: Tunneling correction values [Eq. (5.27)] obtained for the asymmetric Eckart barrier ($\alpha_1 = 12$, $\alpha_2 = 48$).

ξ	SCI[1]	QI	Hansen-Andersen		RPMD[2]	exact
			standard	modified		
2	_	1.48	1.24	_	1.2	1.20
4	_	2.50	1.95	_	2.0	2.01
6	_	7.38	5.13	_	5.3	5.32
8	$2.8 \cdot 10^1$	$7.26{\cdot}10^1$	$3.82{\cdot}10^1$	_	28	$2.61{\cdot}10^1$
10	$2.3 \cdot 10^2$	$3.25{\cdot}10^3$	$1.07{\cdot}10^3$	_	310	$2.52{\cdot}10^2$
12	$3.7 \cdot 10^2$	$3.93{\cdot}10^5$	$8.66{\cdot}10^4$	_	5900	$4.07{\cdot}10^3$
24	$2.9 \cdot 10^{12}$	$5.99{\cdot}10^{18}$	$5.73{\cdot}10^{17}$	_	_	$3.20{\cdot}10^{12}$

[1] Ref. [75], the value for $\xi = 24$ is from Ref. [190].
[2] Ref. [74]

low temperature limit, as the optimal dividing surface will migrate away from the barrier. A similar phenomenon appears to be taking place in this case for two dividing surfaces that depend on two ring polymer coordinates; even though choosing stationary points of $C_{\mathrm{ff}}(0)$ rather than $C_{\mathrm{dd}}(0)$ appears to decrease the recrossing contribution, the improvement is not enough to yield an accuracy comparable to ring polymer molecular dynamics or semiclassical instanton methods.

5.6 Conclusions

We have introduced a modification of Hansen-Andersen transition state theory which was motivated by quantum instanton formalism, and we have demonstrated that the resulting method is more accurate than both approaches. However, we have also found that all three methods exhibit large errors for asymmetric barriers in the low temperature limit, making them much less accurate than ring polymer molecular dynamics in this case. A possible solution to the problem is to use a more sophisticated method which would follow the philosophy of extended quantum instanton formalism [59], however it is evident that the resulting method's path integral implementation would be too expensive to be competitive, hence the possibility was not considered in this work.

We plan to further investigate whether it is possible to improve the accuracy of the quantum instanton and modified Hansen-Andersen formalisms by using an *ad hoc* semiclassical criterion for choosing dividing surfaces. However, care should be taken that the *ad hoc* modifications do not decrease the methods' range of validity: An example can be found in Subsec. 5.5.1, where combining the Hansen-Andersen ansatz (5.23) with dividing surfaces that make $C_{\mathrm{dd}}(0)$ a saddle point, which is a reasonable approximation to a saddle point of $C_{\mathrm{ff}}(0)$, was found to yield a diverging rate at low temperatures. Even though modified Hansen-Andersen formalism performed badly for asymmetric barriers at low temperatures, a semiclassical approximation to this transition state theory may lead to a method that would naturally agree with classical transition state theory in the high temperature limit and would demonstrate a semiclassical instanton-like behavior in the low temperature limit. Such a possibility is also worth investigating in the future.

In this chapter we focused on one-dimensional problems and presented a derivation for the quantum instanton approximation for the separable case; however, additional difficulties can appear in non-separable multidimensional problems. Consider the case of a reaction that has two classical transition states separated far enough from each other. In principle, adding reaction rates obtained separately for the two transition states should give the same result as calculating the reaction rate through both transition states at once. This intuitive criterion is satisfied, for example, by the linearized semiclassical initial value representation and by the ring polymer molecular dynamics, but not by the quantum instanton approximation or any methods based on a short-time approximation to the Miller-Schwartz-Tromp formula that were discussed in this chapter. The fact that the quantum instanton approximation and related methods do not treat fluxes through different parts of the transition state in an "additive" way is not entirely negative as it partially accounts for diffraction effects on the reaction rate. However, the case of two separated transition states shows that these effects can be overestimated in some systems and this is another problem that should be addressed in the future.

6 Conclusions and outlook

In this thesis, we have implemented several methods that accelerate path integral calculations of equilibrium and kinetic isotope effects. We have also explored ways to improve accuracy of the quantum instanton approximation, as it was the method of choice for calculating kinetic isotope effects.

For equilibrium isotope effects, we have introduced a novel Monte Carlo procedure that allows to change mass drastically during the calculation, and we have investigated numerical benefits of combining it with either thermodynamic integration or the method of direct estimators. We have demonstrated that combining both methods with the new Monte Carlo procedure improves their statistical convergence; for thermodynamic integration the modification also allows to eliminate integration error provided a piecewise linear mass-dependent biasing potential is used during the simulation. The numerical benefits of the new approach have been demonstrated on equilibrium isotope effects associated with the change of particle mass in a model harmonic system and with the deuteration of methane. It would be interesting to apply the method to more complex systems, as they will be likely to both decrease the efficiency of our procedure for sampling λ values and increase its possible benefits for statistical convergence. Our expression for the special biasing potential that makes integration error exactly zero has also lead us to the algorithm outlined in the end of Sec. 2.4, which may prove viable for calculating free energy differences in cases when neither thermodynamic integration, nor free energy perturbation approaches are applicable. It would be interesting to investigate whether this is indeed the case.

We have also accelerated the quantum instanton evaluation of kinetic isotope effects by combining virial estimators and higher-order Boltzmann operator splittings, which allowed us to significantly decrease statistical errors and Boltzmann operator discretization errors of the calculation. In addition, we have introduced a more convenient procedure for optimizing dividing surfaces during the calculation. The numerical benefits of the new method were demonstrated on the model $\cdot\mathrm{H} + \mathrm{H}_2$ rearrangement; the approach was then applied to several kinetic isotope effects associated with forward and backward reactions in $\mathrm{CH}_4 + \cdot\mathrm{H} \rightleftharpoons \cdot\mathrm{CH}_3 + \mathrm{H}_2$ reaction system. Unlike our treatment of the equilibrium isotope effects, we have not addressed the issue of integration error; however, we have outlined possible strategies to eliminate it in Sec. 4.5, and it would be interesting to explore them in the future.

In Chapter 5 we have investigated ways to go beyond the quantum instanton approximation in calculating both kinetic isotope effects and absolute reaction rates. The end result can be considered as a quantum instanton-inspired modification of Hansen-Andersen transition state theory, and the new method has been shown to be more accurate than both original approaches. Unfortunately, the quantum instanton approximation as well as both standard and modified versions of Hansen-Andersen transition state theory appear to exhibit large errors for asymmetric barriers at low temperatures. Even though the three methods considered in this work seem to be, in general, less reliable than the ring polymer molecular dynamics, a semiclassical approximation to the modified Hansen-Andersen transition state theory may provide an interesting variation of the semiclassical instanton theory that will agree with the classical transition state theory in the high temperature limit. We also plan to investigate whether it is possible to improve the quantum instanton approximation and modified Hansen-Andersen transition state theory with a semiclassically-motivated choice of dividing surfaces.

A Mass-scaled normal modes of the ring polymer

In this appendix we outline how transforming from Cartesian coordinates to mass-scaled normal modes of the ring polymer [140, 191] leads to simple derivations of the centroid virial estimator $[dF(\lambda)/d\lambda]_{\mathrm{cv}}$ [Eq. (2.8) from Subsec. 2.2.1] and the mass-scaled trial move with respect to the mass parameter λ [Eqs. (2.17)-(2.20) from Subsec. 2.2.2].

The mass-scaled normal mode coordinates $\{\mathbf{a}^{(k)}\}$ and $\{\mathbf{b}^{(l)}\}$ can be obtained as

$$\mathrm{a}_i^{(k)} = \frac{\sqrt{m_i}}{P}\sum_{s=1}^{P}\mathrm{r}_i^{(s)}\cos\left(\frac{2\pi sk}{P}\right),\ k\in\{1,2,\dots,P/2\} \tag{A.1}$$

$$\mathrm{b}_i^{(l)} = \frac{\sqrt{m_i}}{P}\sum_{s=1}^{P}\mathrm{r}_i^{(s)}\sin\left(\frac{2\pi sl}{P}\right),\ l\in\{1,2,\dots,P/2-1\}, \tag{A.2}$$

where $\mathrm{a}_i^{(k)}$ and $\mathrm{b}_i^{(l)}$ are components of $\mathbf{a}^{(k)}$ and $\mathbf{b}^{(l)}$ corresponding to particle i. This set of coordinates becomes complete after adding the centroid $\mathbf{r}^{(C)} = P^{-1}\sum_{s=1}^{P}\mathbf{r}^{(s)}$, which can also be thought of as the zero-frequency normal mode, and we will refer to the triple $(\{\mathbf{a}^{(k)}\},\{\mathbf{b}^{(l)}\},\mathbf{r}^{(C)})$ simply as $\{\mathbf{u}^{(s)}\}$. Note that, for convenience, we have not mass-scaled $\mathbf{r}^{(C)}$. For simplicity, we only consider even values of the Trotter number P since the case of odd P differs in minor details but is otherwise completely analogous.

The original coordinates $\{\mathbf{r}^{(s)}\}$ are recovered from the normal mode coordinates $\{\mathbf{u}^{(s)}\}$ via the inverse transformation

$$\mathrm{r}_i^{(s)} = \mathrm{r}_i^{(C)} + \frac{1}{\sqrt{m_i}}\left\{(-1)^s\mathrm{a}_i^{(P/2)} + 2\sum_{k=1}^{P/2-1}\left[\mathrm{a}_i^{(k)}\cos\left(\frac{2\pi sk}{P}\right) + \mathrm{b}_i^{(k)}\sin\left(\frac{2\pi sk}{P}\right)\right]\right\} \tag{A.3}$$

with the Jacobian

$$J = \frac{P^{NDP/2}\cdot 2^{ND(P/2-1)}}{\left(\prod_{i=1}^{N} m_i\right)^{D(P-1)/2}}. \tag{A.4}$$

These two expressions can be obtained easily starting from properties of the real version of the Discrete Fourier Transform [192].

Rewriting the path integral representation of the partition function in terms of the normal-mode coordinates leads to

$$Q_P = \int d\{\mathbf{u}^{(s)}\}\tilde{\rho}(\{\mathbf{u}^{(s)}\}), \tag{A.5}$$

$$\tilde{\rho} = \tilde{C}\exp\left[-\beta\tilde{\Phi}(\{\mathbf{u}^{(s)}\})\right], \tag{A.6}$$

where the new effective potential $\tilde{\Phi}(\{\mathbf{u}^{(s)}\})$ and normalization constant $\tilde{C}$ are given by

$$\begin{aligned}\tilde{\Phi} :=& \frac{2P^2}{\beta^2\hbar^2}\left\{|\mathbf{a}^{(P/2)}|^2 + \sum_{k=1}^{P/2-1}(|\mathbf{a}^{(k)}|^2 + |\mathbf{b}^{(k)}|^2)\left[1-\cos\left(\frac{2\pi k}{P}\right)\right]\right\} \\ &+ \frac{1}{P}\sum_{s=1}^{P} V\left[\mathbf{r}^{(s)}(\{\mathbf{u}^{(s)}\},\{m_i\})\right],\end{aligned} \tag{A.7}$$

$$\tilde{C} := \left(\frac{P^2}{\beta\hbar^2\pi}\right)^{NDP/2}\frac{\left(\prod_{i=1}^{N} m_i\right)^{D/2}}{2^{ND}}. \tag{A.8}$$

Note that the only term of $\tilde{\Phi}(\{\mathbf{u}^{(s)}\})$ depending on mass is the average of $V(\mathbf{r}^{(s)})$ over the P beads.

With this setup, the centroid virial estimator (2.8) can be obtained immediately by differentiating the right-hand side of Eq. (A.6) with respect to λ. To derive the mass-scaled λ-move described by Eqs. (2.17)-(2.20), we consider making a trial move with respect to λ with $\tilde{\rho}^{(\lambda)}(\{\mathbf{u}^{(s)}\})$ as the probability density while keeping $\{\mathbf{u}^{(s)}\}$ constant. Transforming the corresponding ratio of probability densities

$$\begin{aligned}\frac{\tilde{\rho}^{(\lambda'')}(\{\mathbf{u}^{(s)}\})}{\tilde{\rho}^{(\lambda')}(\{\mathbf{u}^{(s)}\})} =& \left[\prod_{i=1}^{N}\frac{m_i^{(\lambda'')}}{m_i^{(\lambda')}}\right]^{D/2} \\ &\times\exp\left(\frac{\beta}{P}\sum_{s=1}^{P}\{V[\mathbf{r}^{(s)}(\{\mathbf{u}^{(s)}\},\{m_i^{(\lambda')}\})] - V[\mathbf{r}^{(s)}(\{\mathbf{u}^{(s)}\},\{m_i^{(\lambda'')}\})]\}\right)\end{aligned} \tag{A.9}$$

back to Cartesian coordinates $\{\mathbf{r}^{(s)}\}$ will immediately yield Eq. (2.20).

Finally, let us remark that the algorithm used in Subsec. 2.3.2 for sampling the harmonic system also uses normal modes of the ring polymer, albeit not scaled by mass.

B Dependence of the error of stochastic thermodynamic integration on the choice of umbrella biasing potential

In this appendix we discuss how one may minimize the numerical errors appearing if the isotope effect is evaluated with STI [via Eq. (2.23)] by an appropriate choice of the umbrella potential. The two errors introduced by the procedure are the statistical error and integration error due to a finite value of J. To estimate the integration error, we note that $U_b(\lambda)$ is independent of $\{\mathbf{r}^{(s)}\}$ and rewrite $\langle [dF(\lambda)/d\lambda]_{\mathrm{cv}}\rangle^{I_j}$ as

$$\begin{aligned}\langle [dF(\lambda)/d\lambda]_{\mathrm{cv}}\rangle^{I_j} &= \frac{\int_{\lambda_{j-1}}^{\lambda_j} d\lambda \int d\{\mathbf{r}^{(s)}\}\rho^{(\lambda)}(\{\mathbf{r}^{(s)}\})[dF(\lambda)/d\lambda]_{\mathrm{cv}} \exp[-\beta U_b(\lambda)]}{\int_{\lambda_{j-1}}^{\lambda_j} d\lambda \int d\{\mathbf{r}^{(s)}\}\rho^{(\lambda)}(\{\mathbf{r}^{(s)}\}) \exp[-\beta U_b(\lambda)]} \\ &= \frac{\int_{\lambda_{j-1}}^{\lambda_j} d\lambda \exp[-\beta U_b(\lambda)] \int d\{\mathbf{r}^{(s)}\}\rho^{(\lambda)}(\{\mathbf{r}^{(s)}\})[dF(\lambda)/d\lambda]_{\mathrm{cv}}}{\int_{\lambda_{j-1}}^{\lambda_j} d\lambda \exp[-\beta U_b(\lambda)] \int d\{\mathbf{r}^{(s)}\}\rho^{(\lambda)}(\{\mathbf{r}^{(s)}\})} \\ &= -\frac{\int_{\lambda_{j-1}}^{\lambda_j} d\lambda \exp[-\beta U_b(\lambda) + \ln Q^{(\lambda)}] d\ln Q^{(\lambda)}/d\lambda}{\beta \int_{\lambda_{j-1}}^{\lambda_j} d\lambda \exp[-\beta U_b(\lambda) + \ln Q^{(\lambda)}]}.\end{aligned} \tag{B.1}$$

Now let us consider several possible choices for the umbrella potential; an impatient reader should skip the section on a piecewise constant umbrella potential since we show that the most useful in practice is the *piecewise linear* umbrella potential.

B.1 Exact umbrella potential

Suppose that one can find the ideal, "exact" umbrella potential

$$U_{b,\mathrm{exact}}(\lambda) := \beta^{-1} \ln Q^{(\lambda)}. \tag{B.2}$$

Using this exact umbrella potential amounts to the substitution $U_b(\lambda) = U_{b,\text{exact}}(\lambda)$ in Eq. (B.1) and gives

$$\langle [dF(\lambda)/d\lambda]_{\text{cv}} \rangle^{I_j} = -\frac{\ln Q^{(\lambda_j)} - \ln Q^{(\lambda_{j-1})}}{\beta(\lambda_j - \lambda_{j-1})}. \tag{B.3}$$

Since $\lambda_j - \lambda_{j-1} = J^{-1}$, in this ideal situation Eq. (2.23) will yield the exact partition function ratio at any value of J.

B.2 Piecewise constant umbrella potential

Unfortunately, in a realistic calculation this ideal potential $U_{b,\text{exact}}(\lambda)$ is not available and one must make do with an approximation. The simplest choice is a piecewise constant potential

$$U_{b,\text{p.const.}}(\lambda) := U_{b,j} \text{ for } \lambda \in (\lambda_j, \lambda_{j-1}). \tag{B.4}$$

To simplify the following algebra we introduce a symbol

$$\Delta(\lambda) := \ln Q^{(\lambda)} - \ln Q^{(\overline{\lambda}_j)} \tag{B.5}$$

and note that after the substitution $U_b(\lambda) = U_{b,\text{p.const.}}(\lambda)$ the constant factor $\exp[-\beta U_{b,j} + \ln Q^{(\overline{\lambda}_j)}]$ will cancel out between the numerator and denominator of Eq. (B.1), leading to a simplified expression

$$\langle [dF(\lambda)/d\lambda]_{\text{cv}} \rangle^{I_j} = -\frac{\int_{\lambda_{j-1}}^{\lambda_j} d\lambda \exp[\Delta(\lambda)] d\ln Q^{(\lambda)}/d\lambda}{\beta \int_{\lambda_{j-1}}^{\lambda_j} d\lambda \exp[\Delta(\lambda)]}. \tag{B.6}$$

Although it was not important for the derivation of the last equation, it is worthwhile to mention that the constants $U_{b,j}$ are determined in the simulation from the equation

$$U_{b,j+1} = U_{b,j} + \frac{\langle [dF(\lambda)/d\lambda]_{\text{cv}} \rangle^{I_j} + \langle [dF(\lambda)/d\lambda]_{\text{cv}} \rangle^{I_{j+1}}}{2J}. \tag{B.7}$$

Upon changing variables from λ to $\Delta(\lambda)$, the numerator of Eq. (B.6) becomes

$$\int_{\Delta(\lambda_{j-1})}^{\Delta(\lambda_j)} e^{\Delta(\lambda)} d\Delta(\lambda) = e^{\Delta(\lambda_j)} - e^{\Delta(\lambda_{j-1})}, \tag{B.8}$$

hence

$$\langle [dF(\lambda)/d\lambda]_{\text{cv}} \rangle^{I_j} = -\frac{f(\lambda_j) - f(\lambda_{j-1})}{\beta \int_{\lambda_{j-1}}^{\lambda_j} [1 + f(\lambda)] d\lambda}, \tag{B.9}$$

where we defined a function

$$f(\lambda) := e^{\Delta(\lambda)} - 1, \tag{B.10}$$

whose Taylor series expansion about $\overline{\lambda}_j$,

$$f(\lambda) = f'(\overline{\lambda}_j)(\lambda - \overline{\lambda}_j) + \frac{f''(\overline{\lambda}_j)}{2}(\lambda - \overline{\lambda}_j)^2 + \frac{f'''(\overline{\lambda}_j)}{6}(\lambda - \overline{\lambda}_j)^3 + \mathcal{O}[(\lambda - \overline{\lambda}_j)^4], \tag{B.11}$$

will be used in the following. To see how good an approximation the piecewise constant potential gives, let us compare the numerators and denominators of Eqs. (B.3) and (B.9). The difference of the denominators is

$$\beta \int_{\lambda_{j-1}}^{\lambda_j} [1 + f(\lambda)] d\lambda - \beta(\lambda_j - \lambda_{j-1}) = \frac{\beta f''(\overline{\lambda}_j)}{24 J^3} + \mathcal{O}(J^{-4}). \tag{B.12}$$

Noting that $f(\lambda) = \mathcal{O}(\lambda - \overline{\lambda}_j)$ and Taylor expanding the logarithm, we find the difference of the numerators to be

$$\begin{aligned} & f(\lambda_j) - f(\lambda_{j-1}) - \ln[1 + f(\lambda_j)] + \ln[1 + f(\lambda_{j-1})] \\ =& \frac{f(\lambda_j)^2 - f(\lambda_{j-1})^2}{2} - \frac{f(\lambda_j)^3 - f(\lambda_{j-1})^3}{3} + \mathcal{O}(J^{-4}) \\ =& \frac{[f(\lambda_j) - f(\lambda_{j-1})][f(\lambda_j) + f(\lambda_{j-1})]}{2} \\ & - \frac{f'(\overline{\lambda}_j)^3 (\lambda_j - \lambda_{j-1})^3}{12} + \mathcal{O}(J^{-4}) \\ =& \frac{f'(\overline{\lambda}_j) f''(\overline{\lambda}_j)}{8 J^3} - \frac{f'(\overline{\lambda}_j)^3}{12 J^3} + \mathcal{O}(J^{-4}). \end{aligned} \tag{B.13}$$

Since both the numerator and denominator of Eq. (B.3) are $\mathcal{O}(J^{-1})$, and since the errors in Eq. (B.9) of both the denominator [Eq. (B.12)] and numerator [Eq. (B.13)] are $\mathcal{O}(J^{-3})$, the overall error is $\mathcal{O}(J^{-2})$, that is, for an umbrella potential constant over each I_j

$$\langle [dF(\lambda)/d\lambda]_{\text{cv}} \rangle^{I_j} = -\frac{\ln Q^{(\lambda_j)} - \ln Q^{(\lambda_{j-1})}}{\beta(\lambda_j - \lambda_{j-1})} + \mathcal{O}(J^{-2}). \tag{B.14}$$

In conclusion, for the piecewise constant biasing potential Eq. (2.23) will have an error $\mathcal{O}(J^{-2})$:

$$\exp\left\{ -\frac{\beta}{J} \sum_{j=1}^{J} \langle [dF(\lambda)/d\lambda]_{\text{cv}} \rangle^{I_j} \right\} = \frac{Q_P^{(B)}}{Q_P^{(A)}} + \mathcal{O}(J^{-2}). \tag{B.15}$$

As discussed in Subsec. (2.2.2), it is easy to use really large values of J during the calculation, therefore an $\mathcal{O}(J^{-2})$ error is not an issue. Yet, it is still worthwhile to try to optimize the procedure in order to go beyond an $\mathcal{O}(J^{-2})$ error.

B.3 Piecewise linear umbrella potential

The obvious "first" improvement is introducing a piecewise linear potential. A remarkable fact about the resulting procedure is that it yields an exactly zero integration error, and this is true to all orders in J. Indeed, if we introduce a $U_b(\lambda) = U_{b,\text{p.lin.}}(\lambda)$, where

$$U_{b,\text{p.lin.}}(\lambda) := U_{b,j} - \langle [dF(\lambda)/d\lambda]_{\text{cv}} \rangle^{I_j} (\lambda - \overline{\lambda}_j), \tag{B.16}$$

then the constant factor $\exp(-\beta\{U_{b,j} - \langle[dF(\lambda)/d\lambda]_{\mathrm{cv}}\rangle^{I_j}\overline{\lambda}_j\})$ will cancel between the numerator and denominator of Eq. (B.1), giving

$$\langle[dF(\lambda)/d\lambda]_{\mathrm{cv}}\rangle^{I_j} = -\frac{\int_{\lambda_{j-1}}^{\lambda_j} d\lambda \exp\{\beta\langle[dF(\lambda)/d\lambda]_{\mathrm{cv}}\rangle^{I_j}\lambda + \ln Q^{(\lambda)}\} d\ln Q^{(\lambda)}/d\lambda}{\beta\int_{\lambda_{j-1}}^{\lambda_j} d\lambda \exp\{\beta\langle[dF(\lambda)/d\lambda]_{\mathrm{cv}}\rangle^{I_j}\lambda + \ln Q^{(\lambda)}\}}. \tag{B.17}$$

Multiplying both sides of the equation by the denominator and rearranging yields an identity

$$0 = \int_{\lambda_{j-1}}^{\lambda_j} \exp\{\beta\langle[dF(\lambda)/d\lambda]_{\mathrm{cv}}\rangle^{I_j}\lambda + \ln Q^{(\lambda)}\}\{\beta\,\langle[dF(\lambda)/d\lambda]_{\mathrm{cv}}\rangle^{I_j}\,d\lambda + d\ln Q^{(\lambda)}\} \tag{B.18}$$

$$= \int_{g(\lambda_{j-1})}^{g(\lambda_j)} dg(\lambda) e^{g(\lambda)} = e^{g(\lambda_j)} - e^{g(\lambda_{j-1})}, \tag{B.19}$$

where we have introduced a function $g(\lambda) := \beta\langle[dF(\lambda)/d\lambda]_{\mathrm{cv}}\rangle^{I_j}\lambda + \ln Q^{(\lambda)}$. The last equality means $g(\lambda_j) = g(\lambda_{j-1})$, leading to

$$\langle[dF(\lambda)/d\lambda]_{\mathrm{cv}}\rangle^{I_j} = -\frac{\ln Q^{(\lambda_j)} - \ln Q^{(\lambda_{j-1})}}{\beta(\lambda_j - \lambda_{j-1})}, \tag{B.20}$$

which is, remarkably, the same as Eq. (B.3) for the *exact* umbrella potential.

Of course, the definition of the piecewise linear umbrella potential in Eq. (B.16) is recursive, and therefore can only be evaluated by an iterative algorithm, but this should not cause a great concern since any biasing potential $U_b(\lambda)$, regardless of its type, cannot be known *a priori* (in particular, even the piecewise constant umbrella potential must be constructed iteratively).

As already mentioned in Subsec. (2.2.2), making $U_b(\lambda)$ not only piecewise linear [by satisfying Eq. (B.16)] but also continuous [by choosing the constants $U_{b,j}$ from Eq. (B.7)] allows to approach an optimal statistical error. An analytical analysis of the statistical error is more involved; instead, in the following section we show numerically that the statistical error is approximately independent of the choice of the umbrella potential and converges to a limit as J is increased—in particular, the piecewise linear umbrella potential permits reducing the integration to zero without increasing the statistical error.

B.4 Numerical tests

As the piecewise linear umbrella potential $U_{b,\mathrm{p.lin.}}(\lambda)$ defined by Eq. (2.24) yields a zero integration error and can be obtained iteratively in any system, it was this potential that was used in the production runs in the rest of the paper. To clearly demonstrate the advantages of $U_{b,\mathrm{p.lin.}}(\lambda)$, in this section we compare the different choices of the umbrella potential on the harmonic system from Subsec. 2.3.2, for which which even the exact umbrella potential (B.2) is available since $Q_P^{(\lambda)}$ is known analytically.

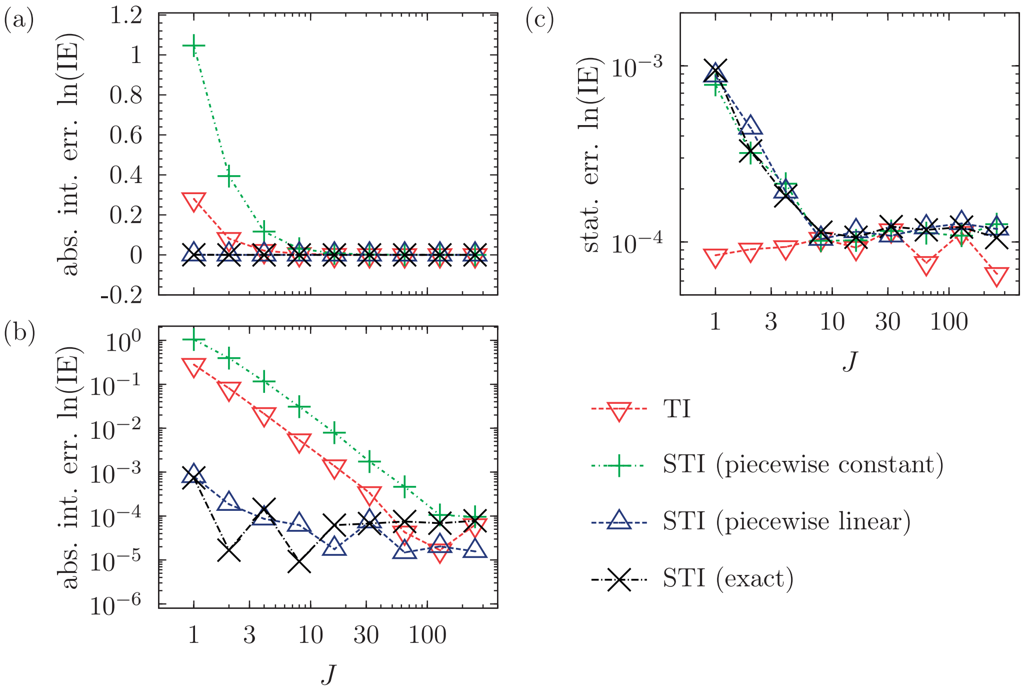

Figure B.1: Impact of the umbrella biasing potential on the numerical errors of a simulation. The figure shows the dependence of integration errors [(a) with linear, (b) with logarithmic scale] and statistical errors [panel (c)] on the number J of λ intervals used in the standard thermodynamic integration (TI) and stochastic thermodynamic integration (STI) employing various types of umbrella potentials mentioned in parentheses: "piecewise constant" uses an umbrella potential (B.4) constant over each of the J intervals, "piecewise linear" potential is given by Eqs. (2.24) or (B.16), and "exact" corresponds to the unrealistic situation when one knows the exact, ideal umbrella potential (B.2).

The results are presented in Fig. B.1, which shows the dependence of integration and statistical errors on J. [Note that all methods employed the linear interpolation of mass given by Eq. (2.3) and that the values obtained with TI and with STI with a piecewise linear potential are the same as those already presented in Subsec. 2.3.2.]

As predicted above, the integration error of STI appears to be zero for both the ideal, exact umbrella potential (B.2) and for the piecewise linear umbrella potential (B.16) [panels (a) and (b)], whereas both TI with the midpoint rule and STI with the piecewise constant umbrella potential (B.4) exhibit an $\mathcal{O}(J^{-2})$ integration error [panel (b)]. Note that for a given J the integration error of STI with the piecewise constant potential is even larger than the error of TI using the midpoint rule; however, this does not imply that STI is less efficient than TI since in realistic calculations STI can be used with much larger values of J than TI, without increasing the statistical error or the computational cost. Finally, note that the different choices of the umbrella potential do not significantly affect the statistical error [see panel (c)].

C Details of combining direct estimators with stochastic change of mass

The procedure for changing mass between discrete values of λ for SDE is mostly the same as the one described in Subsec. 2.2.2 but for two important differences. The first one is that the umbrella potential $U_b(\lambda)$ is now updated in such a way that it satisfies for all $j \in [1, J-1]$

$$\exp\{\beta[U_b(\overline{\lambda}_j) - U_b(\overline{\lambda}_{j+1})]\} = \frac{\langle \mathcal{Z}_{\mathrm{sc}}^{\overline{\lambda}_{j+1},\lambda_j} \rangle^{(\overline{\lambda}_{j+1})}}{\langle \mathcal{Z}_{\mathrm{sc}}^{\overline{\lambda}_j,\lambda_j} \rangle^{(\overline{\lambda}_j)}} \tag{C.1}$$

in order to minimize statistical error of the calculated isotope effect. Secondly, for the simple λ-move [Eqs. (2.12)-(2.16)] we note that since the acceptance ratio appearing in Eq. (2.16) is computationally cheap and we only need to consider a finite (and usually small) number of λ-values. It is therefore possible to numerically include acceptance probability into trial distribution, leading to the following procedure:

Simple λ-move:

1. For each $j \in 1, \ldots, J$ calculate:

$$p_j = \left(\prod_{i=1}^{N} m_i^{(\overline{\lambda}_j)} \right) \exp\left[-\frac{P}{2\beta\hbar^2} \sum_{i=1}^{N} m_i^{(\overline{\lambda}_j)} \sum_{s=1}^{P} |\mathrm{r}_i^{(s)} - \mathrm{r}_i^{(s-1)}|^2 - \beta U_b(\overline{\lambda}_j) \right] \tag{C.2}$$

$$\tilde{p}_j = \frac{\sum_{j'=1}^{j} p_{j'}}{\sum_{j'=1}^{J} p_{j'}} \tag{C.3}$$

2. Choose random number Δ distributed uniformly over $[0, 1]$.

3. Choose j' which is the smallest integer satisfying

$$\Delta < \tilde{p}_{j'}. \tag{C.4}$$

4. Set $j = j'$, $\lambda = \overline{\lambda}_{j'}$.

It was mentioned in Subsec. 2.2.2 that in the case of STI simple λ-moves cannot lead to large changes of λ as the acceptance ratio of Eq. (2.11) exhibits a maximum which becomes sharper with larger values of P. We note that the SDE variant of the procedure outlined above cannot address this issue, as the smallest λ step one can make is limited by J, and therefore should become less effective at lower temperatures, as will be observed in Subsec. 3.3.3. For the mass-scaled λ-move the only difference is that during the trial move (2.17) the trial λ values are picked not from the entire $[0, 1]$ interval, but from among the $\overline{\lambda}_j$ values.

D Estimate of the relative path integral discretization error

To estimate the discretization error of the path integral representation Q_P of the partition function we start from the identity,

$$Q_P = Q + \mathcal{O}\left(\frac{1}{P^n}\right) = Q + \frac{c}{P^n} + o\left(\frac{1}{P^n}\right), \tag{D.1}$$

where c is independent of P and the integer n depends on the splitting used to derive Q_P (in particular, $n = 2$ for the Lie-Trotter and $n = 4$ for Takahashi-Imada [79] and Suzuki-Chin [80, 81] factorizations). As usual, the little-o symbol is defined by the relation $f(x) = o[g(x)]$ if $g(x) \neq 0$ in some neighborhood of $x = 0$ and $\lim_{x\to 0} f(x)/g(x) = 0$. We proceed to rewrite the relative discretization error of Q_P as

$$\begin{aligned} \frac{Q_P - Q}{Q} &= \frac{c/P^n + o(P^{-n})}{Q} = \frac{1}{1-2^{-n}} \frac{Q + c/P^n - Q - c/(2P)^n + o(P^{-n})}{Q_P + \mathcal{O}(P^{-n})} \\ &= \frac{1}{1-2^{-n}} \frac{Q_P - Q_{2P} + o(P^{-n})}{Q_P + \mathcal{O}(P^{-n})} = \frac{1}{1-2^{-n}} \frac{Q_P - Q_{2P}}{Q_P} + o(P^{-n}). \end{aligned} \tag{D.2}$$

It follows that we can estimate the discretization error of Q_P if we can estimate the ratio Q_{2P}/Q_P. We shall therefore derive a direct estimator for Q_{2P}/Q_P; for simplicity, we will do this explicitly only for the special case of Lie-Trotter splitting ($n = 2$). The derivation, which resembles that presented in Ref. [193] for the direct estimator of Q_P/Q_1, starts by expressing Q_{2P} as

$$\begin{aligned} Q_{2P} = &\left(\frac{P}{\pi\beta\hbar^2}\right)^{DNP} \left(\prod_{i=1}^{N} m_i\right)^{DP} \int d\{\mathbf{r}'^{(s)}\} d\{\mathbf{r}^{(s)}\} \\ &\times \exp\left\{-\frac{P}{\beta\hbar^2} \sum_{s=0}^{P-1} \left(||\mathbf{r}'^{(s)} - \mathbf{r}^{(s)}||_+^2 + ||\mathbf{r}'^{(s)} - \mathbf{r}^{(s+1)}||_+^2\right) - \frac{\beta}{2P} \sum_{s=1}^{P} \left[V(\mathbf{r}'^{(s)}) + V(\mathbf{r}^{(s)})\right]\right\}, \end{aligned} \tag{D.3}$$

where both $\{\mathbf{r}^{(s)}\}$ and $\{\mathbf{r}'^{(s)}\}$ are sets of P vector variables in the system's configuration space. Since $||\cdots||_+$ is a norm induced by an inner product, it satisfies the parallelogram law

$$||\mathbf{r}'^{(s)}-\mathbf{r}^{(s)}||_+^2+||\mathbf{r}'^{(s)}-\mathbf{r}^{(s+1)}||_+^2=\frac{1}{2}(||2\mathbf{r}'^{(s)}-\mathbf{r}^{(s+1)}-\mathbf{r}^{(s)}||_+^2+||\mathbf{r}^{(s)}-\mathbf{r}^{(s+1)}||_+^2), \quad (D.4)$$

which allows to rewrite Q_{2P} as

$$Q_{2P}=C\int \mathcal{W}_2 d\{\mathbf{r}^{(s)}\}\rho(\{\mathbf{r}^{(s)}\}), \quad (D.5)$$

where $\mathcal{W}_2$, defined as

$$\begin{aligned}\mathcal{W}_2=\int &\exp\left\{\frac{\beta}{2P}\sum_{s=1}^{P}[V(\mathbf{r}^{(s)})-V(\mathbf{r}'^{(s)})]\right\}\\ &\times\prod_{s=1}^{P}\left[\left(\prod_{i=1}^{N}m_i\right)^{D/2}\left(\frac{2P}{\pi\beta\hbar^2}\right)^{DN/2}\exp\left(-\frac{2P}{\beta\hbar^2}\left|\left|\mathbf{r}'^{(s)}-\frac{\mathbf{r}^{(s)}+\mathbf{r}^{(s+1)}}{2}\right|\right|_+^2\right)d\mathbf{r}'^{(s)}\right],\end{aligned} \quad (D.6)$$

is obviously the direct estimator for Q_{2P}/Q_P. $\mathcal{W}_2$ can be evaluated by generating $\mathbf{r}'$ with the Box-Muller method and averaging the resulting exponential factor; the procedure is in a way reminiscent of the last step of bisection path integral sampling method [194, 195]. Note that for large values of P the Gaussians from which $\{\mathbf{r}'^{(s)}\}$ are sampled are quite narrow, making the sum $\sum_{s=1}^{P}[V(\mathbf{r}^{(s)})-V(\mathbf{r}'^{(s)})]$ approach 0, which should in turn lead to a reasonably fast statistical convergence of the estimator.

Incidentally, one can express the discretization error of Q_P by evaluating a direct estimator for $Q_{P/2}/Q_P$, which we therefore denote $\mathcal{W}_{1/2}$. This estimator can be derived completely analogously, with the result

$$\mathcal{W}_{1/2}=\exp\left\{\frac{\beta}{P}\sum_{s=1}^{P/2}\left[V(\mathbf{r}^{(2s-1)})-V(\mathbf{r}^{(2s)})\right]\right\}. \quad (D.7)$$

Unlike $\mathcal{W}_2$, $\mathcal{W}_{1/2}$ does not require additional evaluations of the potential energy; however, estimating discretization error from $Q_P/Q_{P/2}$ would typically yield less accurate results than estimating it from Q_{2P}/Q_P.

As for the discretization error of the isotope effect itself, one can similarly obtain the estimate

$$\frac{\mathrm{IE}_P}{\mathrm{IE}}-1=\frac{1}{1-2^{-n}}\left(1-\frac{\mathrm{IE}_{2P}}{\mathrm{IE}_P}\right)+o(P^{-n})=\frac{1}{1-2^{-n}}\left(1-\frac{\langle\mathcal{W}_2\rangle^{(1)}}{\langle\mathcal{W}_2\rangle^{(0)}}\right)+o(P^{-n}). \quad (D.8)$$

In this case it is necessary to calculate two averages at $\lambda=0$ and $\lambda=1$ to obtain the discretization error estimate.

To make sure that our estimates are correct we ran test calculations for one-dimensional harmonic oscillator with $\beta\hbar\omega = 8$ ($T = 1$ K) at several P values, with the isotope effect corresponding to the doubling of the mass. The results, presented in Fig. D.1, show that our method for estimating the discretization error becomes very accurate with increasing P, and in fact could, in principle, be used to decrease the discretization error of the calculation from $O(P^{-n})$ to $o(P^{-n})$ (by subtracting the error estimate from the result). Unfortunately, a practical Monte Carlo calculation also has a statistical error, which decreases only as an inverse square root of the total number of Monte Carlo steps, while Eq. (D.1) implies that the discretization error decreases approximately as P^{-n}. Since the total cost of the calculation is approximately proportional to the product of the number of Monte Carlo steps and P, it is clear that in a practical calculation the statistical error will be much harder to decrease than the discretization error. Therefore, in this manuscript, we opted to use the discretization error estimate (D.8) only to make sure that the discretization error of the isotope effect is smaller than statistical error. However, it is also possible to subtract these discretization error estimates from the calculated value of ln(IE) in order to obtain a result that will be closer to the quantum limit, but whose discretization error can no longer be estimated. Thus the data presented in Table 3.1 for the CD_4/CH_4 isotope effect allows two different ways to interpret the results, the choice is left to the reader.

Finally, note that expressions analogous to Eqs. (D.6) and (D.7) can also be derived for the fourth-order Takahashi-Imada (1.21) and Suzuki-Chin (1.24) splittings. One needs to be careful, however, since both fourth-order factorization replace V with an effective potential V_{eff} that, unlike V, depends on P. As for the Suzuki-Chin factorization, the matter is further complicated by the fact that the weight of this effective potential depends on the bead s at which it is evaluated.

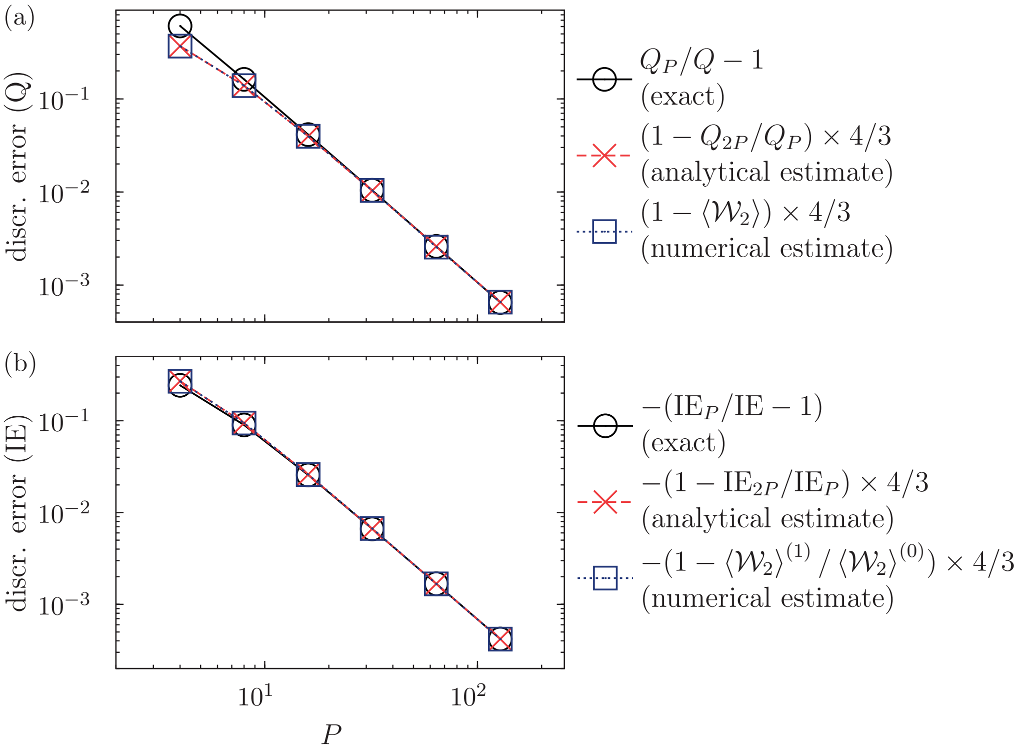

Figure D.1: Comparison of exact analytical values of the path integral discretization error of (a) the partition function Q and (b) isotope effect with their estimates [Eqs. (D.2) and (D.8)], which were evaluated either analytically or numerically using the estimator (D.6). The figure shows the dependence of the discretization error on the Trotter number P in a one-dimensional harmonic oscillator with $\beta\hbar\omega = 8$, and the isotope effect corresponds to the doubling of the mass.

E Derivation of the fourth-order corrections for different estimators

When one of the fourth-order factorizations is used, $V_{\text{eff}}^{(s)}(\mathbf{r}^{(s)})$ has an explicit dependence on mass and β; as a result one needs to add appropriate "corrections" to the estimators arising from the differentiation with respect to these quantities.

For $d\ln Q_r/d\lambda/\beta$ and $\partial\ln C_{\text{dd}}/\partial\lambda/\beta$, it follows from Eqs. (1.40) (when applied to change of mass) and (4.29) that the correction $F_{r,\text{grad}}$ is

$$F_{r,\text{grad}} = -\frac{\beta}{P^3}\sum_{i=1}^{N}\frac{dm_i}{d\lambda}\sum_{s=1}^{P}w_s d_s \frac{\partial V_{\text{grad}}(\mathbf{r}^{(s)})}{\partial m_i} = \frac{\hbar^2\beta}{P^3}\sum_{s=1}^{P}w_s d_s\sum_{i=1}^{N}\frac{1}{m_i^2}\frac{dm_i}{d\lambda}|\nabla_i V(\mathbf{r}^{(s)})|^2. \tag{E.1}$$

Note that when a coordinate rescaling is used to obtain an estimator (e.g., for centroid virial estimators), the correction remains the same due to the following equality:

$$\frac{dV_{\text{eff}}^{(s)}[\mathbf{r}^{(s)}(m_i), m_i]}{dm_i} = \left\langle \frac{\partial \mathbf{r}^{(s)}}{\partial m_i}, \frac{\partial V_{\text{eff}}^{(s)}}{\partial \mathbf{r}^{(s)}} \right\rangle_0 + d_s\left(\frac{\beta}{P}\right)^2\frac{\partial V_{\text{grad}}}{\partial m_i}. \tag{E.2}$$

As for F_{th} and F_{v}, since

$$\frac{\partial V_{\text{eff}}^{(s)}(\mathbf{r}^{(s)})}{\partial\beta} = 2d_s\frac{\beta}{P^2}V_{\text{grad}}(\mathbf{r}^{(s)}), \tag{E.3}$$

the gradient correction to be added is

$$F_{\text{grad}} = \frac{4\beta^2}{P^3}\left(\sum_{s=1}^{P/2-1} - \sum_{s=P/2+1}^{P-1}\right) w_s d_s V_{\text{grad}}(\mathbf{r}^{(s)}). \tag{E.4}$$

Again, this correction is the same for the virial and thermodynamic variants.

Since the G factor involves the second derivatives with respect to β, the corrections will be different for G_{th} and G_{v}. While $G_{\text{th,grad}}$ is obtained easily as

$$G_{\text{th,grad}} = -\frac{24\beta}{P^3}\sum_{s=1}^{P} w_s d_s V_{\text{grad}}(\mathbf{r}^{(s)}), \tag{E.5}$$

to find G_{v}, one needs to take advantage of the following relations:

$$\frac{dV_{\text{eff}}^{(s)}[\mathbf{r}^{(s)}(\beta),\beta]}{d\beta} = \left\langle \frac{\partial \mathbf{r}^{(s)}(\beta)}{\partial\beta}, \frac{\partial V_{\text{eff}}^{(s)}(\mathbf{r}^{(s)})}{\partial \mathbf{r}^{(s)}} \right\rangle_0 + \frac{\partial V_{\text{eff}}^{(s)}(\mathbf{r}^{(s)})}{\partial\beta}, \tag{E.6}$$

$$\begin{aligned}\frac{d^2V_{\text{eff}}^{(s)}[\mathbf{r}^{(s)}(\beta),\beta]}{d\beta^2} =& \left\langle \frac{\partial^2 \mathbf{r}^{(s)}(\beta)}{\partial\beta^2}, \frac{\partial V_{\text{eff}}^{(s)}(\mathbf{r}^{(s)})}{\partial \mathbf{r}^{(s)}} \right\rangle_0 + \left\langle \frac{\partial \mathbf{r}^{(s)}(\beta)}{\partial\beta}, \frac{\partial^2 V_{\text{eff}}^{(s)}(\mathbf{r}^{(s)})}{(\partial \mathbf{r}^{(s)})^2}, \frac{\partial \mathbf{r}^{(s)}(\beta)}{\partial\beta} \right\rangle_{00}\\ &+ 2\left\langle \frac{\partial \mathbf{r}^{(s)}(\beta)}{\partial\beta}, \frac{\partial}{\partial \mathbf{r}^{(s)}}\left[\frac{\partial V_{\text{eff}}^{(s)}(\mathbf{r}^{(s)})}{\partial\beta}\right] \right\rangle_0 + \frac{\partial^2 V_{\text{eff}}^{(s)}(\mathbf{r}^{(s)})}{\partial\beta^2},\end{aligned} \tag{E.7}$$

$$\begin{aligned}\frac{d^2\{\beta V_{\text{eff}}^{(s)}[\mathbf{r}^{(s)}(\beta),\beta]\}}{d\beta^2} =& 2\frac{dV_{\text{eff}}^{(s)}(\mathbf{r}^{(s)})}{d\beta} + \beta\frac{d^2V_{\text{eff}}^{(s)}(\mathbf{r}^{(s)})}{d\beta^2}\\ =& \left\langle \left(2\frac{\partial \mathbf{r}^{(s)}(\beta)}{\partial\beta} + \beta\frac{\partial^2 \mathbf{r}^{(s)}(\beta)}{\partial\beta^2}\right), \frac{\partial V_{\text{eff}}^{(s)}(\mathbf{r}^{(s)})}{\partial \mathbf{r}^{(s)}} \right\rangle_0\\ &+ \beta\left\langle \frac{\partial \mathbf{r}^{(s)}(\beta)}{\partial\beta}, \frac{\partial^2 V_{\text{eff}}^{(s)}(\mathbf{r}^{(s)})}{(\partial \mathbf{r}^{(s)})^2}, \frac{\partial \mathbf{r}^{(s)}(\beta)}{\partial\beta} \right\rangle_{00}\\ &+ 2\beta\left\langle \frac{\partial \mathbf{r}^{(s)}(\beta)}{\partial\beta}, \frac{\partial}{\partial \mathbf{r}^{(s)}(\beta)}\left[\frac{\partial V_{\text{eff}}^{(s)}(\mathbf{r}^{(s)})}{\partial\beta}\right] \right\rangle_0 + \beta\frac{\partial^2 V_{\text{eff}}^{(s)}(\mathbf{r}^{(s)})}{\partial\beta^2} + 2\frac{\partial V_{\text{eff}}^{(s)}(\mathbf{r}^{(s)})}{\partial\beta},\end{aligned} \tag{E.8}$$

The only terms for which the explicit β dependence plays a role are the last three. As a result we get:

$$G_{\text{v,grad}} = -\frac{4}{P}\sum_{s=1}^{P} w_s \left\{ 2\beta\left\langle \frac{\partial \mathbf{r}^{(s)}(\beta)}{\partial\beta}, \frac{\partial}{\partial \mathbf{r}^{(s)}(\beta)}\left[\frac{\partial V_{\text{eff}}^{(s)}(\mathbf{r}^{(s)})}{\partial\beta}\right] \right\rangle_0 + \beta\frac{\partial^2 V_{\text{eff}}^{(s)}(\mathbf{r}^{(s)})}{\partial\beta^2} + 2\frac{\partial V_{\text{eff}}^{(s)}(\mathbf{r}^{(s)})}{\partial\beta} \right\}. \tag{E.9}$$

This expression can be rewritten as

$$G_{\text{v,grad}} = -\frac{8\beta}{P^3}\sum_{s=1}^{P} w_s d_s \left[3V_{\text{grad}} + \left\langle (\mathbf{r}^{(s)} - \check{\mathbf{r}}^{(s)}), \nabla V_{\text{grad}}(\mathbf{r}^{(s)}) \right\rangle_0\right]. \tag{E.10}$$

F Derivation of $\mathbf{B}^{\mathbf{k}(\gamma)}$

The present derivation is just a slight generalization of the estimators generally employed in adaptive biasing force approaches [130, 131]. We start by transforming to mass-scaled coordinates,

$$\begin{aligned} \mathrm{x}_i^{(s)} &:= \sqrt{m_i}\mathrm{r}_i^{(s)}, \\ \mathrm{x}_{\gamma i} &:= \sqrt{m_i}\mathrm{r}_{\gamma i}, \\ \bar{\xi}_\gamma(\mathbf{x}_\gamma) &:= \xi_\gamma(\mathbf{r}_\gamma), \end{aligned} \tag{F.1}$$

which will simplify the subsequent algebra due to the equality

$$||\nabla\xi_\gamma(\mathbf{r}_\gamma)||_- = |\nabla\bar{\xi}_\gamma(\mathbf{x}_\gamma)|. \tag{F.2}$$

In mass-scaled coordinates, the path integral representation (1.53) of the delta-delta correlation function can be rewritten as

$$C_{\mathrm{dd},P} = \int \bar{\rho}(\{\mathbf{x}^{(s)}\})\Delta[\bar{\xi}_\gamma(\mathbf{x}_\gamma)]\,d\{\mathbf{x}^{(s)}\}, \tag{F.3}$$

where the second normalized delta function has been absorbed into $\bar{\rho}$ in order to simplify the following derivation. Differentiation of $C_{\mathrm{dd},P}$ with respect to the dividing surfaces' parameters yields

$$\begin{aligned}\frac{\partial C_{\mathrm{dd},P}}{\partial\eta_k^{(\gamma)}} =&\frac{\partial}{\partial\eta_k^{(\gamma)}}\int\overline{\rho}(\{\mathbf{x}^{(s)}\})\Delta\left[\overline{\xi}_\gamma(\mathbf{x}_\gamma,\eta_k^{(\gamma)})\right]d\{\mathbf{x}^{(s)}\}\\ =&\int\frac{\langle\nabla\overline{\xi}_\gamma(\mathbf{x}_\gamma),\nabla\overline{\xi}_\gamma(\mathbf{x}_\gamma)\rangle}{|\nabla\overline{\xi}_\gamma(\mathbf{x}_\gamma)|}\overline{\rho}(\{\mathbf{x}^{(s)}\})\frac{\partial\overline{\xi}_\gamma(\mathbf{x}_\gamma)}{\partial\eta_k^{(\gamma)}}\frac{d}{d\overline{\xi}_\gamma}\left\{\delta\left[\overline{\xi}_\gamma(\mathbf{x}_\gamma,\eta_k^{(\gamma)})\right]\right\}d\{\mathbf{x}^{(s)}\}\\ &+\int\frac{\partial\ln|\nabla\overline{\xi}_\gamma(\mathbf{x}_\gamma)|}{\partial\eta_k^{(\gamma)}}\overline{\rho}(\{\mathbf{x}^{(s)}\})\Delta\left[\overline{\xi}_\gamma(\mathbf{x}_\gamma,\eta_k^{(\gamma)})\right]d\{\mathbf{x}^{(s)}\}\\ =&\int\nabla\left\{\delta\left[\overline{\xi}_\gamma(\mathbf{x}_\gamma,\eta_k^{(\gamma)})\right]\right\}\frac{\partial\overline{\xi}_\gamma(\mathbf{x}_\gamma)}{\partial\eta_k^{(\gamma)}}\frac{\nabla\overline{\xi}_\gamma(\mathbf{x}_\gamma)}{\left|\nabla\overline{\xi}_\gamma(\mathbf{x}_\gamma)\right|}\overline{\rho}(\{\mathbf{x}^{(s)}\})d\{\mathbf{x}^{(s)}\}\\ &+\int\frac{1}{|\nabla\overline{\xi}_\gamma(\mathbf{x}_\gamma)|^2}\left\langle\nabla\overline{\xi}_\gamma,\nabla\frac{\partial\overline{\xi}_\gamma(\mathbf{x}_\gamma)}{\partial\eta_k^{(\gamma)}}\right\rangle\overline{\rho}(\{\mathbf{x}^{(s)}\})\Delta\left[\overline{\xi}_\gamma(\mathbf{x}_\gamma,\eta_k^{(\gamma)})\right]d\{\mathbf{x}^{(s)}\}.\end{aligned}\tag{F.4}$$

After integrating by parts with respect to $\mathbf{x}_\gamma$ in the first integral, we get

$$\begin{aligned}\frac{\partial}{\partial\eta_k^{(\gamma)}}\int\overline{\rho}(\{\mathbf{x}^{(s)}\})\Delta\left[\overline{\xi}_\gamma(\mathbf{x}_\gamma,\eta_k^{(\gamma)})\right]d\{\mathbf{x}^{(s)}\}=-\int\frac{\partial\overline{\xi}_\gamma(\mathbf{x}_\gamma)}{\partial\eta_k^{(\gamma)}}&\left[\left\langle\nabla\overline{\xi}_\gamma(\mathbf{x}_\gamma),\nabla^{(\gamma)}\ln\overline{\rho}(\{\mathbf{x}^{(s)}\})\right\rangle_0\right.\\ &\left.+|\nabla\overline{\xi}_\gamma(\mathbf{x}_\gamma)|\left\langle\nabla,\frac{\nabla\overline{\xi}_\gamma(\mathbf{x}_\gamma)}{|\nabla\overline{\xi}_\gamma(\mathbf{x}_\gamma)|}\right\rangle_0\right]/|\nabla\overline{\xi}_\gamma(\mathbf{x}_\gamma)|^2\\ &\times\Delta\left[\overline{\xi}_\gamma(\mathbf{x}_\gamma,\eta_k^{(\gamma)})\right]\overline{\rho}(\{\mathbf{x}^{(s)}\})d\{\mathbf{x}^{(s)}\}.\end{aligned}\tag{F.5}$$

Equation (4.32) is obtained by substituting the explicit expression for $\overline{\rho}$ and transforming back to Cartesian coordinates.

G Additional numerical results

In this appendix we present some additional numerical results that were moved from the main text of Chapter 4 for the sake of clarity. Figure G.1 depicts the logarithmic plots of the discretization errors of various ingredients of the quantum instanton approximation as functions of the Trotter number P. The discretization error for a quantity A is defined as $|A_P - A_\infty|$, where A_∞ was estimated by averaging A_P over several highest values of P, for which the discretization error was considered negligible. The averaging was performed in order to reduce the statistical error. The plots in Fig. G.1 demonstrate the faster convergence to the quantum limit achieved with higher-order factorizations: indeed, especially for the logarithmic derivative of Q_r, one can see that the discretization error dependence approaches the asymptotic behavior $\mathcal{O}(P^{-2})$ for the Lie-Trotter and $\mathcal{O}(P^{-4})$ for the Suzuki-Chin and Takahashi-Imada factorizations. In addition, in all panels, it is clear for which value of P the discretization error becomes smaller than the statistical error, since for higher values of P the smooth dependence of the discretization error on P is obscured by statistical noise.

Table G.1 contains values of various factors used to obtain the results in Table 4.2 for the quantum instanton kinetic isotope effect on the reaction $\cdot\mathrm{H}_\alpha + \mathrm{H}_\beta\mathrm{H}_\gamma \rightarrow \mathrm{H}_\alpha\mathrm{H}_\beta + \cdot\mathrm{H}_\gamma$ with optimized dividing surfaces. Finally, Table G.2 contains optimized dividing surfaces' positions that were used for calculating kinetic isotope effects on the $\mathrm{CH}_4 + \cdot\mathrm{H} \rightleftharpoons \cdot\mathrm{CH}_3 + \mathrm{H}_2$.

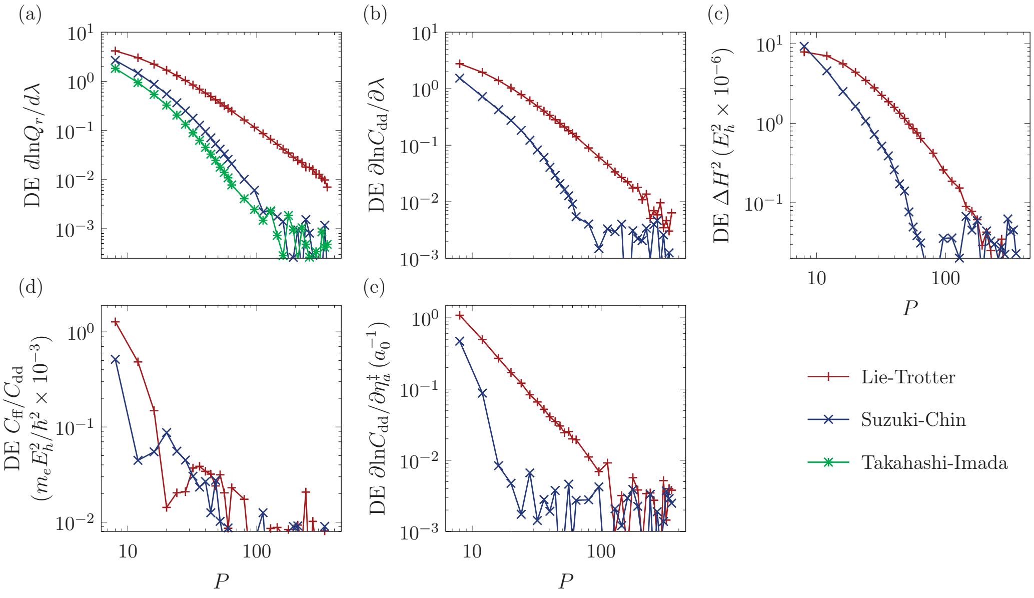

Figure G.1: Absolute discretization error (DE) of different quantities as a function of P: (a) $d\ln Q_r/d\lambda$, (b) $\partial\ln C_{\rm dd}/\partial\lambda$, (c) ΔH^2, (d) $C_{\rm ff}/C_{\rm dd}$, (e) $\partial\ln C_{\rm dd}/\partial\eta_a^\ddagger$. Results shown were obtained with the virial estimators and correspond to the kinetic isotope effect $\cdot\mathrm{H}+\mathrm{H}_2/\cdot\mathrm{D}+\mathrm{D}_2$ at 200 K.

Table G.1: Values of the factors entering the quantum instanton expression (4.26) for the kinetic isotope effect $\cdot\mathrm{H}+\mathrm{H}_2/\cdot\mathrm{D}+\mathrm{D}_2$ with optimized dividing surfaces' positions, displayed in Table 4.2. All quantities as well as their statistical errors are in atomic units.

T (K)	$\Delta H^2\times10^6$		$C_{\rm ff}/C_{\rm dd}\times10^3$		$C_{\rm dd}$ ratio	Q_r ratio
	$\lambda=0$	$\lambda=1$	$\lambda=0$	$\lambda=1$		
200	3.68±0.03	4.27±0.02	1.33±0.01	2.03±0.01	43.8 ±0.3	1404 ±1
250	4.87±0.04	4.95±0.03	2.01±0.01	2.10±0.01	55.8 ±0.3	572.9 ±0.3
300	7.40±0.04	5.10±0.03	2.73±0.01	1.97±0.01	49.5 ±0.1	316.1 ±0.2
400	7.92±0.05	6.27±0.04	2.49±0.01	2.01±0.01	33.96±0.06	149.5 ±0.1
600	12.0 ±0.1	10.7 ±0.1	2.77±0.01	2.44±0.01	23.11±0.04	70.92±0.03
1000	26.8 ±0.1	24.5 ±0.1	3.82±0.03	3.55±0.02	18.15±0.02	39.42±0.01
1500	54.3 ±0.2	50.3 ±0.2	5.29±0.04	5.05±0.02	16.78±0.02	30.11±0.01
2400	124.6 ±0.4	117.1 ±0.4	7.98±0.05	7.80±0.03	16.36±0.01	25.51±0.01

Table G.2: Optimal positions of the dividing surfaces along the reaction coordinate [see Eq. (4.51)] for transition states of several isotopic variants of the $CH_4 + \cdot H \rightleftharpoons \cdot CH_3 + H_2$ exchange at several temperatures.

Potential energy surface of Ref. [7]				
TS	400 K	500 K	600 K	700 K
$H_3C \cdots H \cdots H$	-0.91	-0.90	-0.88	-0.86
$H_3C \cdots H \cdots D$	-0.88	-0.87	-0.85	-0.84
$D_3C \cdots H \cdots D$	-0.89	-0.88	-0.86	-0.85
$D_3C \cdots D \cdots H$	-0.93	-0.91	-0.89	-0.86
$H_3C \cdots D \cdots D$	-0.89	-0.87	-0.86	-0.85
$D_3C \cdots D \cdots D$	-0.90	-0.89	-0.87	-0.85
$D_3C \cdots H \cdots H$	-0.92	-0.90	-0.89	-0.87
	467 K	531 K	650 K	
$H_3C \cdots H \cdots D$	-0.87	-0.86	-0.84	
$H_3C \cdots D \cdots H$	-0.90	-0.89	-0.87	
Potential energy surface of Ref. [6]				
TS	400 K	500 K	600 K	700 K
$H_3C \cdots H \cdots H$	-1.03	-1.00	-0.97	-0.95
$H_3C \cdots H \cdots D$	-1.00	-0.97	-0.94	-0.92

H Connection of flux-flux and delta-delta correlation functions for the separable case

In this appendix we will prove that the relation between $C_{\mathrm{dd}}(t)$ and $C_{\mathrm{ff}}(t)$ (5.3) holds for a separable system if the stationarity condition (5.2) is satisfied. We start by writing $C_{\mathrm{dd}}(t)$ for one-dimensional case as

$$C_{\mathrm{dd}}(t) = \frac{1}{m^{\ddagger}} |\langle x_a | e^{-\beta^{+}\hat{H}/2} | x_b \rangle|^2, \tag{H.1}$$

where x_a and x_b are positions of dividing surfaces a and b. Straightforward differentiation allows us to write

$$\begin{aligned}\frac{\partial^2 C_{\mathrm{dd}}(t)}{\partial x_a \partial x_b} =& \frac{2}{m^{\ddagger}} \mathrm{Re} \left[\frac{\partial^2}{\partial x_a \partial x_b} \left(\langle x_a | e^{-\beta^{+}\hat{H}/2} | x_b \rangle \right) \langle x_a | e^{-\beta^{-}\hat{H}/2} | x_b \rangle \right. \\ & \left. + \frac{\partial}{\partial x_a} \left(\langle x_a | e^{-\beta^{+}\hat{H}/2} | x_b \rangle \right) \frac{\partial}{\partial x_b} \left(\langle x_a | e^{-\beta^{-}\hat{H}/2} | x_b \rangle \right) \right],\end{aligned} \tag{H.2}$$

where Re is the real part of a complex number.

We now recall the expression for the flux operator (4.19) and write $C_{\mathrm{ff}}(t)$ for a one dimensional system as

$$\begin{aligned}C_{\mathrm{ff}}(t) =& \frac{1}{2} \left(\frac{\hbar}{m^{\ddagger}} \right)^2 \mathrm{Re} \left[\frac{\partial^2}{\partial x_a \partial x_b} \left(\langle x_a | e^{-\beta^{+}\hat{H}/2} | x_b \rangle \right) \langle x_a | e^{-\beta^{-}\hat{H}/2} | x_b \rangle \right. \\ & \left. - \frac{\partial}{\partial x_a} \left(\langle x_a | e^{-\beta^{+}\hat{H}/2} | x_b \rangle \right) \frac{\partial}{\partial x_b} \left(\langle x_a | e^{-\beta^{-}\hat{H}/2} | x_b \rangle \right) \right].\end{aligned} \tag{H.3}$$

Comparing Eqs. (H.2) and (H.3) and keeping in mind the stationarity condition (5.2) leads to

$$C_{\mathrm{ff}}(t) = \frac{\hbar^2}{4 m^{\ddagger}} \frac{\partial^2 C_{\mathrm{dd}}(t)}{\partial x_a \partial x_b}. \tag{H.4}$$

This equation leads directly to Eq. (5.3) once we recall our choice for dividing surfaces' positions (5.1). The case of a many-dimensional system with a separable reaction coordinate can be easily reduced to the one-dimensional problem.

I Justification of using Hansen-Andersen ansatz for the flux-flux correlation function with split dividing surfaces

In this appendix, we elaborate two statements made in Sec. 5.4. The first one is that as $t \to \pm \mathrm{i}\beta\hbar/2$ the flux-flux correlation function $C_{\mathrm{ff}}(t)$ will exhibit a singularity of the order 3/2 if the two dividing surfaces are merged or will approach zero if the two dividing surfaces are split (as we mentioned before, the former fact has been know for a long time [187]; however, unlike Ref. [187], we will prove it without assuming separability of the reaction coordinate). The second one is that if the dividing surfaces are split and the resulting $C_{\mathrm{ff}}(0)$ is stationary with respect to their positions, than even though the Hansen-Andersen ansatz (5.23) is no longer applicable to $C_{\mathrm{ff}}(t)$ due to wrong imaginary-time behavior, it is still valid to use its integral to estimate Miller-Schwartz-Tromp formula (1.16).

I.1 Imaginary time behavior of flux-flux correlation function

We will first discuss the difference of imaginary-time behavior of $C_{\mathrm{ff}}(t)$ with merged and split dividing surfaces, and to that end we introduce $\epsilon = t - \mathrm{i}\beta\hbar/2$ and write out the limiting expression for $C_{\mathrm{ff}}(t)$ as $\epsilon \to 0$. In order to simplify the algebra we define

$$\partial_\gamma := \left\langle \nabla\xi_\gamma(\mathbf{r}_\gamma), \frac{\partial}{\partial \mathbf{r}_\gamma} \right\rangle_- \tag{I.1}$$

and proceed to rewrite $C_{\mathrm{ff}}(t)$ as

$$\begin{aligned}C_{\mathrm{ff}}(t) =& \mathrm{Tr}[\hat{F}_a e^{-(\beta-\epsilon)\hat{H}}\hat{F}_b e^{-\epsilon\hat{H}}],\\ =& -\frac{\hbar^2}{4}\int\Big[\partial_a\langle\mathbf{r}_a|e^{-\epsilon\hat{H}}|\mathbf{r}_b\rangle\partial_b\langle\mathbf{r}_a|e^{-(\beta-\epsilon)\hat{H}}|\mathbf{r}_b\rangle\\ &+\partial_b\langle\mathbf{r}_a|e^{-\epsilon\hat{H}}|\mathbf{r}_b\rangle\partial_a\langle\mathbf{r}_a|e^{-(\beta-\epsilon)\hat{H}}|\mathbf{r}_b\rangle\\ &+\partial_a\partial_b\langle\mathbf{r}_a|e^{-\epsilon\hat{H}}|\mathbf{r}_b\rangle\langle\mathbf{r}_a|e^{-(\beta-\epsilon)\hat{H}}|\mathbf{r}_b\rangle\\ &+\langle\mathbf{r}_a|e^{-\epsilon\hat{H}}|\mathbf{r}_b\rangle\partial_a\partial_b\langle\mathbf{r}_a|e^{-(\beta-\epsilon)\hat{H}}|\mathbf{r}_b\rangle\Big]\prod_{\gamma=a,b}\delta[\xi_\gamma(\mathbf{r}_\gamma)]d\mathbf{r}_\gamma.\end{aligned}\tag{I.2}$$

If one recalls Lie-Trotter splitting (1.20) of the Boltzmann operator, then one realizes that in the limit $\epsilon\to 0$ $\langle\mathbf{r}_a|e^{-\epsilon\hat{H}}|\mathbf{r}_b\rangle$ will approach $\delta(||\mathbf{r}_b-\mathbf{r}_a||_+)$ and will lead to $C_{\mathrm{ff}}(t)$ approaching zero if $\mathbf{r}_a$ and $\mathbf{r}_b$ are constrained to different surfaces. If the two dividing surfaces are merged, however, $C_{\mathrm{ff}}(t)$ will go to infinity instead. To show that we start by writing

$$\begin{aligned}\lim_{\epsilon\to 0}\langle\mathbf{r}_a|e^{-\epsilon\hat{H}}|\mathbf{r}_b\rangle\prod_{\gamma=a,b}\delta[\xi_\gamma(\mathbf{r}_\gamma)] &= \lim_{\epsilon\to 0}\frac{\left(\prod_{i=1}^N m_i\right)^{D/2}}{(2\pi\hbar^2\epsilon)^{DN/2}}\exp\left(-\frac{||\mathbf{r}_b-\mathbf{r}_a||_+^2}{2\hbar^2\epsilon}\right)\prod_{\gamma=a,b}\delta[\xi_\gamma(\mathbf{r}_\gamma)]\\ &= \lim_{\epsilon\to 0}\frac{\left(\prod_{i=1}^N m_i\right)^{D/2}}{\sqrt{2\pi\hbar^2\epsilon}}\Delta_a(\mathbf{r}_a)\delta(\mathbf{r}_a-\mathbf{r}_b),\end{aligned}\tag{I.3}$$

proving that the term containing $\langle\mathbf{r}_a|e^{-\epsilon\hat{H}}|\mathbf{r}_b\rangle$ is $\mathcal{O}(\epsilon^{-1/2})$. We also have

$$\begin{aligned}\lim_{\epsilon\to 0}\partial_a\langle\mathbf{r}_a|e^{-\epsilon\hat{H}}|\mathbf{r}_b\rangle\prod_{\gamma=a,b}\delta[\xi_\gamma(\mathbf{r}_\gamma)] =& \lim_{\epsilon\to 0}\frac{\left(\prod_{i=1}^N m_i\right)^{D/2}}{(2\pi\hbar^2\epsilon)^{DN/2}}\frac{\langle\nabla\xi_a(\mathbf{r}_a),\mathbf{r}_a-\mathbf{r}_b\rangle_0}{\hbar^2\epsilon}\\ &\times\exp\left(-\frac{||\mathbf{r}_b-\mathbf{r}_a||_+^2}{2\hbar^2\epsilon}\right)\prod_{\gamma=a,b}\delta[\xi_\gamma(\mathbf{r}_\gamma)].\end{aligned}\tag{I.4}$$

Since both $\mathbf{r}_a$ and $\mathbf{r}_b$ are constrained to $\xi_a(\mathbf{r}_a)=\xi_b(\mathbf{r}_b)=0$, the expression is exactly zero if the dividing surface has no curvature. However, if the dividing surface is curved then it can be easily shown that

$$\langle\nabla\xi_a(\mathbf{r}_a),\mathbf{r}_a-\mathbf{r}_b\rangle_0=\mathcal{O}(||\mathbf{r}_b-\mathbf{r}_a||_+),\tag{I.5}$$

leading to the following estimate

$$\lim_{\epsilon\to 0}\partial_\gamma\langle\mathbf{r}_a|e^{-\epsilon\hat{H}}|\mathbf{r}_b\rangle\prod_{\gamma=a,b}\delta[\xi_\gamma(\mathbf{r}_\gamma)]=\mathcal{O}(\epsilon^{-1})\times\Delta_a(\mathbf{r}_a)\delta(\mathbf{r}_a-\mathbf{r}_b).\tag{I.6}$$

The last expression we need to consider is

$$\begin{aligned}\lim_{\epsilon\to 0}\partial_a\partial_b\langle\mathbf{r}_a|e^{-\epsilon\hat{H}}|\mathbf{r}_b\rangle\prod_{\gamma=a,b}\delta[\xi_\gamma(\mathbf{r}_\gamma)] = \lim_{\epsilon\to 0}\Bigg[&\frac{\langle\nabla\xi_a(\mathbf{r}_a),\nabla\xi_b(\mathbf{r}_b)\rangle_-}{\hbar^2\epsilon}\\ &-\frac{\langle\nabla\xi_a(\mathbf{r}_a),\mathbf{r}_a-\mathbf{r}_b\rangle_0\langle\nabla\xi_b(\mathbf{r}_b),\mathbf{r}_b-\mathbf{r}_a\rangle_0}{\hbar^4\epsilon^2}\Bigg]\\ &\times\frac{\left(\prod_{i=1}^N m_i\right)^{D/2}}{(2\pi\hbar^2\epsilon)^{DN/2}}\exp\left(-\frac{||\mathbf{r}_b-\mathbf{r}_a||_+^2}{2\hbar^2\epsilon}\right)\prod_{\gamma=a,b}\delta[\xi_\gamma(\mathbf{r}_\gamma)],\end{aligned}\tag{I.7}$$

which is $\mathcal{O}(\epsilon^{-3/2})\times\Delta_a(\mathbf{r}_a)\delta(\mathbf{r}_a-\mathbf{r}_b)$, as seen from Eqs. (I.3) and (I.5). These estimates prove that $C_{\mathrm{ff}}(t)$ is $\mathcal{O}(\epsilon^{-3/2})$ as well.

I.2 Hansen-Andersen ansatz and the split dividing surfaces' case

For reasons outlined above it is difficult to account for imaginary time behavior of $C_{\mathrm{ff}}(t)$, as it changes too drastically if dividing surfaces are split or merged, making it natural to instead consider a function resembling $\tilde{C}_{\mathrm{ff}}(t)$ introduced in Sec. 5.2. To that end, we will consider reaction coordinates of the form

$$\tilde{\tilde{\xi}}_\gamma(\mathbf{r},t)=\xi(\mathbf{r})-\tilde{\tilde{\eta}}_\gamma(t),\tag{I.8}$$

where $\xi(\mathbf{r})$ is a reaction coordinate and $\tilde{\tilde{\eta}}_\gamma(t)$ is such that $\tilde{\tilde{\xi}}_\gamma(\mathbf{r},t)=0$ defines dividing surfaces that make $C_{\mathrm{ff}}(t)$ a saddle point with respect to their positions. Arguments analogous to the ones in Sec. 5.2 allow us to write

$$\begin{aligned}k&=\frac{1}{Q_r}\lim_{t\to\infty}\tilde{\tilde{C}}_{\mathrm{fs}}(t)&\text{(I.9)}\\&=\frac{1}{2Q_r}\int_{-\infty}^{\infty}\tilde{\tilde{C}}_{\mathrm{ff}}(t)dt,&\text{(I.10)}\end{aligned}$$

where we introduced $\tilde{\tilde{C}}_{\mathrm{fs}}(t)$ as the flux-side correlation function corresponding to dividing surfaces set by $\tilde{\tilde{\xi}}_\gamma(\mathbf{r},t)=0$ and $\tilde{\tilde{C}}_{\mathrm{ff}}(t)$ is given by

$$\begin{aligned}\tilde{\tilde{C}}_{\mathrm{ff}}(t)&:=\frac{d\tilde{\tilde{C}}_{\mathrm{fs}}(t)}{dt}&\text{(I.11)}\\&=C_{\mathrm{ff}}[t,\{\tilde{\tilde{\eta}}_\gamma(t)\}]+\sum_{\gamma=a,b}\frac{\partial\tilde{\tilde{\eta}}_\gamma(t)}{\partial t}\frac{\partial C_{\mathrm{fs}}[t,\{\tilde{\tilde{\eta}}_\gamma(t)\}]}{\partial\tilde{\tilde{\eta}}_\gamma}&\text{(I.12)}\end{aligned}$$

Again, analogously to the relation between $\tilde{C}_{\mathrm{dd}}(t)$ and $C_{\mathrm{dd}}(t)$ of Eq. (5.15), we can write

$$\tilde{\tilde{C}}_{\mathrm{ff}}(t)=C_{\mathrm{ff}}(t)+\mathcal{O}(t^4).\tag{I.13}$$

Appendix I. Justification of using Hansen-Andersen ansatz for the flux-flux correlation function with split dividing surfaces

We now consider behavior of $\tilde{\tilde{C}}_{\mathrm{ff}}(t)$ for imaginary time values. Since $C_{\mathrm{ff}}(t)$ is an even function of time, $\tilde{\tilde{\eta}}_{\gamma}(t)$ will be even as well, and analytical continuation of $\tilde{\tilde{\eta}}_{\gamma}(t)$ into complex time values will yield real values for imaginary times. Consequently, for imaginary time values $\tilde{\tilde{\eta}}_{\gamma}(t)$ will still yield dividing surfaces' positions that make $C_{\mathrm{ff}}(t)$ a saddle point, and both $C_{\mathrm{ff}}[t, \{\tilde{\tilde{\eta}}_{\gamma}(t)\}]$ and $C_{\mathrm{fs}}[t, \{\tilde{\tilde{\eta}}_{\gamma}(t)\}]$ appearing in Eq. (I.12) will be actual flux-flux and flux-side functions corresponding to dividing surfaces defined by $\tilde{\tilde{\eta}}_{\gamma}(t)$. Next, we note that at least in some neighborhood of $\epsilon = 0$ the two dividing surfaces will be merged. For one-dimensional case this can be shown by taking derivative of Eq. (I.2) with respect to $||\mathbf{r}_b - \mathbf{r}_a||_+$ and observing that the result will go to ∞ or $-\infty$ if $\epsilon \to 0$ unless $||\mathbf{r}_b - \mathbf{r}_a||_+ = 0$; for multidimensional case the procedure is more involved, but yields the same result. It is also obvious that the optimal position of the merged dividing surface will have a $\epsilon \to 0$ limit, which can be seen from differentiating $\epsilon^{3/2} C_{\mathrm{ff}}$ with respect to the dividing surface's position; this implies that $\tilde{\tilde{\eta}}_{\gamma}(t)$ have limits at $\epsilon \to 0$ and are bound in any neighborhood of $\epsilon = 0$. We finally go to Eq. (I.12) and observe that $C_{\mathrm{ff}}[t, \{\tilde{\tilde{\eta}}_{\gamma}(t)\}]$ should be $\mathcal{O}(\epsilon^{-3/2})$ since $C_{\mathrm{ff}}(t)$ is $\mathcal{O}(\epsilon^{-3/2})$ for any choice of dividing surfaces and $\tilde{\tilde{\eta}}_{\gamma}(t)$ are bound in a neighborhood of $\epsilon = 0$. For the second term, we note that since $\tilde{\tilde{\eta}}_{\gamma}(t)$ have a limit in $\epsilon \to \infty$, $d\tilde{\tilde{\eta}}_{\gamma}(t)/dt$ is $o(\epsilon^{-1})$. We also reiterate that derivative of $\epsilon^{3/2} C_{\mathrm{ff}}(t)$ with respect to a merged dividing surface's position has a $\epsilon \to 0$ limit, meaning that in this case we have $\partial C_{\mathrm{ff}}[t, \{\tilde{\tilde{\eta}}_{\gamma}(t)\}]/\partial \tilde{\tilde{\eta}}_{\gamma}(t) = \mathcal{O}(\epsilon^{-3/2})$; this implies that $\partial C_{\mathrm{fs}}[t, \{\tilde{\tilde{\eta}}_{\gamma}(t)\}]/\partial \tilde{\tilde{\eta}}_{\gamma}(t) = \mathcal{O}(\epsilon^{-1/2})$, and as a result the second term in Eq. (I.12) is $o(\epsilon^{-3/2})$, and the expression itself is $\mathcal{O}(\epsilon^{-3/2})$.

Now that we have proven that analytic continuation of $\tilde{\tilde{C}}_{\mathrm{ff}}(t)$ into complex plane leads to 3/2 singularities at $t = \pm \mathrm{i}\beta\hbar/2$, we go back to calculating reaction rate via Eq. (I.10) and note that a suitable ansatz for $\tilde{\tilde{C}}_{\mathrm{ff}}(t)$ should have a form analogous to the Hansen-Andersen ansatz for $C_{\mathrm{ff}}(t)$ (5.23). As Eq. (I.13) implies, this procedure would be numerically equivalent to simply using Hansen-Andersen ansatz for $C_{\mathrm{ff}}(t)$ and then taking the integral of the ansatz to recover the reaction rate. As a final note we would like to emphasize that, unlike the quantum instanton derivation of Sec. 5.2, the algebra presented in this appendix is correct in the general multidimensional case.

Bibliography

[1] B. Cheng and M. Ceriotti, J. Chem. Phys. **141**, 244112 (2015).

[2] K. Karandashev and J. Vaníček, J. Chem. Phys. **146**, 184102 (2017).

[3] W. H. Miller, Y. Zhao, M. Ceotto, and S. Yang, J. Chem. Phys. **119**, 1329 (2003).

[4] N. F. Hansen and H. C. Andersen, J. Chem. Phys. **101**, 6032 (1994).

[5] N. F. Hansen and H. C. Andersen, J. Phys. Chem. **100**, 1137 (1996).

[6] J. C. Corchado, J. L. Bravo, and J. Espinosa-Garcia, J. Chem. Phys. **130**, 184314 (2009).

[7] X. Zhang, B. J. Braams, and J. M. Bowman, J. Chem. Phys. **124**, 021104 (2006).

[8] A. Hermann and C. W. Nash, *The genesis of quantum theory (1899-1913)* (McGraw-Hill, 1971).

[9] M. Wolfsberg, W. A. V. Hook, P. Paneth, and L. P. N. Rebelo, *Isotope Effects in the Chemical, Geological and Bio Sciences* (McGraw-Hill, 2010).

[10] R. P. Feynman and A. R. Hibbs, *Quantum mechanics and path integrals* (McGraw-Hill, 1965).

[11] D. Chandler and P. G. Wolynes, J. Chem. Phys. **74**, 4078 (1981).

[12] T. Yamamoto and W. H. Miller, J. Chem. Phys. **120**, 3086 (2004).

[13] H. C. Urey, J. Chem. Soc. **1947**, 562 (1947).

[14] K. E. Janak and G. Parkin, J. Am. Chem. Soc. **125**, 13219 (2003).

[15] R. H. McKenzie, B. Athokpam, and S. G. Ramesh, J. Chem. Phys. **143**, 044309 (2015).

[16] M. A. Webb and T. F. Miller III, J. Phys. Chem. A **118**, 467 (2014).

[17] O. Redlich, Z. Phys. Chem. **28B**, 371 (1935).

[18] V. I. Pupyshev, Y. N. Panchenko, and N. F. Stepanov, Vib. Spectrosc. **7**, 191 (1994).

[19] P. Richet, Y. Bottinga, and M. Javoy, Ann. Rev. Earth Planet. Sci. **5**, 65 (1977).

[20] V. Barone, J. Chem. Phys. **120**, 3059 (2004).

[21] Q. Liu, J. A. Tossell, and Y. Liu, Geochim. Cosmochim. Acta **74**, 6965 (2010).

[22] D. Chandler, J. Chem. Phys. **68**, 2959 (1978).

[23] B. J. Berne and M. Borkovec, J. Chem. Soc., Faraday Trans. **94**, 2717 (1998).

[24] D. G. Truhlar and B. C. Garrett, Annu. Rev. Phys. Chem. **35**, 159 (1984).

[25] B. C. Garrett and D. G. Truhlar, J. Am. Chem. Soc. **101**, 4534 (1979).

[26] E. Wigner, Z. Phys. Chem. Abt. B **19**, 203 (1932).

[27] B. C. Garrett and D. G. Truhlar, Proc. Natl. Acad. Sci. USA **76**, 4755 (1979).

[28] J. Pu, J. C. Corchado, and D. G. Truhlar, J. Chem. Phys. **115**, 6266 (2001).

[29] S. Ramazani, J. Chem. Phys. **138**, 194305 (2013).

[30] D. A. Singleton and M. J. Szymanski, J. Am. Chem. Soc. **121**, 9455 (1999).

[31] W. Adam, O. Krebs, M. Orfanopoulos, M. Stratakis, and G. C. Vougioukalakis, J. Org. Chem. **68**, 2420 (2003).

[32] H. Liu and A. Warshel, J. Phys. Chem. B **111**, 7852 (2007).

[33] A.-L. Johansson, S. Chakrabarty, C. L. Berthold, M. Högbom, A. Warshel, and P. Brzezinski, Biochim. Biophys. Acta, Bioenerg. **1807**, 1083 (2011).

[34] M. H. Glickman, J. S. Wiseman, and J. P. Klinman, J. Am. Chem. Soc. **116**, 793 (1994).

[35] C. C. Hwang and C. B. Grissom, J. Am. Chem. Soc. **116**, 795 (1994).

[36] S. Hu, S. C. Sharma, A. D. Scouras, A. V. Soudackov, C. A. M. Carr, S. Hammes-Schiffer, T. Alber, and J. P. Klinman, J. Am. Chem. Soc. **136**, 8157 (2014).

[37] A. Sen and A. Kohen, J. Phys. Org. Chem **23**, 613 (2010).

[38] H. Liu and A. Warshel, in *Quantum Tunnelling in Enzyme-Catalysed Reactions* (The Royal Society of Chemistry, 2009) pp. 242–267.

[39] D. G. Fleming, D. J. Arseneau, O. Sukhorukov, J. H. Brewer, S. L. Mielke, D. G. Truhlar, G. C. Schatz, B. C. Garrett, and K. A. Peterson, J. Chem. Phys. **135**, 184310 (2011).

[40] D. G. Fleming, D. J. Arseneau, O. Sukhorukov, J. H. Brewer, S. L. Mielke, G. C. Schatz, B. C. Garrett, K. A. Peterson, and D. G. Truhlar, Science **331**, 448 (2011).

[41] P. G. Jambrina, E. García, V. J. Herrero, V. Sáez-Rábanos, and F. J. Aoiz, J. Chem. Phys. **135**, 034310 (2011).

[42] R. Pérez de Tudela, F. J. Aoiz, Y. V. Suleimanov, and D. E. Manolopoulos, J. Phys. Chem. Lett. **3**, 493 (2012).

[43] A. L. Bucharchenko, J. Phys. Chem. B **117**, 2231 (2013).

[44] W. H. Miller, J. Chem. Phys. **62**, 1899 (1975).

[45] T. Peng, D. H. Zhang, D.-Y. Wang, Y.-M. Li, and J. Z. H. Zhang, Comp. Phys. Commun. **128**, 492 (2000).

[46] D. Skouteris, J. F. Castillo, and D. E. Manolopoulos, Comp. Phys. Commun. **133**, 128 (2000).

[47] S. L. Mielke, G. C. Lynch, D. G. Truhlar, and D. W. Schwenke, Chem. Phys. Lett. **216**, 441 (1993).

[48] S. L. Mielke, G. C. Lynch, D. G. Truhlar, and D. W. Schwenke, J. Phys. Chem. **98**, 8000 (1994).

[49] S. T. Banks and D. C. Clary, Phys. Chem. Chem. Phys. **9**, 933 (2007).

[50] X. Shan and D. C. Clary, Phys. Chem. Chem. Phys. **15**, 18530 (2013).

[51] L. Bañares, F. J. Aoiz, P. Honvault, B. Bussery-Honvault, and J.-M. Launay, J. Chem. Phys. **118**, 565 (2003).

[52] F. J. Aoiz, M. Brouard, C. J. Eyles, J. F. Castillo, and V. Sáez Rábanos, J. Chem. Phys. **125**, 144105 (2006).

[53] W. H. Miller, J. Chem. Phys. **61**, 1823 (1974).

[54] W. H. Miller, S. D. Schwartz, and J. W. Tromp, J. Chem. Phys. **79**, 4889 (1983).

[55] F. Matzkies and U. Manthe, J. Chem. Phys. **108**, 4828 (1998).

[56] S. Andersson, G. Nyman, A. Arnaldsson, U. Manthe, and H. Jónsson, J. Phys. Chem. A **113**, 4468 (2009).

[57] C. Venkataraman and W. H. Miller, J. Chem. Phys. **126**, 094104 (2007).

[58] J. O. Richardson, J. Chem. Phys. **144**, 114106 (2016).

[59] M. Ceotto, S. Yang, and W. H. Miller, J. Chem. Phys. **122**, 044109 (2005).

[60] R. Kubo, M. Yokota, and S. Nakajima, J. Phys. Soc. Japan **12**, 1203 (1957).

[61] T. Yamamoto, J. Chem. Phys. **33**, 281 (1960).

[62] S. Coleman, Phys. Rev. D **15**, 2929 (1977).

[63] C. G. Callan, Jr. and S. Coleman, Phys. Rev. D **16**, 1762 (1977).

[64] S. C. Althorpe, J. Chem. Phys. **134**, 114104 (2011).

[65] M. Kryvohuz, J. Chem. Phys. **134**, 114103 (2011).

[66] J. O. Richardson, Faraday Discuss. **195**, 49 (2016).

[67] S. R. McConnell, A. Löhle, and J. Kästner, J. Chem. Phys. **146**, 074105 (2017).

[68] M. J. Gillan, J. Phys. C **20**, 3621 (1987).

[69] G. A. Voth, D. Chandler, and W. H. Miller, J. Chem. Phys. **91**, 7749 (1989).

[70] J. Cao and G. A. Voth, J. Chem. Phys. **100**, 5106 (1994).

[71] E. Pollak and J.-L. Liao, J. Chem. Phys. **108**, 2733 (1998).

[72] I. R. Craig and D. E. Manolopoulos, J. Chem. Phys. **121**, 3368 (2004).

[73] I. R. Craig and D. E. Manolopoulos, J. Chem. Phys. **122**, 084106 (2005).

[74] I. R. Craig and D. E. Manolopoulos, J. Chem. Phys. **123**, 034102 (2005).

[75] J. O. Richardson and S. C. Althorpe, J. Chem. Phys. **131**, 214106 (2009).

[76] T. J. H. Hele and S. C. Althorpe, J. Chem. Phys. **138**, 084108 (2013).

[77] M. Suzuki, J. Stat. Phys. **43**, 883 (1986).

[78] H. F. Trotter, Proc. Am. Math. Soc. **10**, 545 (1959).

[79] M. Takahashi and M. Imada, J. Phys. Soc. Jpn. **53**, 3765 (1984).

[80] S. A. Chin, Phys. Lett. A **226**, 344 (1997).

[81] M. Suzuki, Phys. Lett. A **201**, 425 (1995).

[82] S. Jang, S. Jang, and G. A. Voth, J. Chem. Phys. **115**, 7832 (2001).

[83] A. Pérez and M. E. Tuckerman, J. Chem. Phys. **135**, 064104 (2011).

[84] V. A. Lynch, S. L. Mielke, and D. G. Truhlar, J. Phys. Chem. A **109**, 10092 (2005).

[85] J. A. Morrone and R. Car, Phys. Rev. Lett. **101**, 017801 (2008).

[86] D. M. Ceperley and E. L. Pollock, Can. J. Phys. **65**, 1416 (1987).

[87] J. A. Barker, J. Chem. Phys. **70**, 2914 (1979).

[88] M. F. Herman, E. J. Bruskin, and B. J. Berne, J. Chem. Phys. **76**, 5150 (1982).

[89] M. Parrinello and A. Rahman, J. Chem. Phys. **80**, 860 (1984).

[90] C. Predescu and J. D. Doll, J. Chem. Phys. **117**, 7448 (2002).

[91] C. Predescu, D. Sabo, J. D. Doll, and D. L. Freeman, J. Chem. Phys. **119**, 12119 (2003).

[92] J. G. Kirkwood, J. Chem. Phys. **3**, 300 (1935).

[93] A. Pérez and O. A. von Lilienfeld, J. Chem. Theory Comput. **7**, 2358 (2011).

[94] R. W. Zwanzig, J. Chem. Phys. **22**, 1420 (1954).

[95] C. Oostenbrink, J. Comput. Chem. **30**, 212 (2009).

[96] M. Ceriotti and T. E. Markland, J. Chem. Phys. **138**, 014112 (2013).

[97] L. Rosso, P. Mináry, Z. Zhu, and M. E. Tuckerman, J. Chem. Phys. **116**, 4389 (2002).

[98] J. B. Abrams, L. Rosso, and M. E. Tuckerman, J. Chem. Phys. **125**, 074115 (2006).

[99] P. Wu, X. Hu, and W. Yang, J. Phys. Chem. Lett. **2**, 2099 (2011).

[100] J. Kästner and W. Thiel, J. Chem. Phys. **123**, 144104 (2005).

[101] V. Kapil, J. Behler, and M. Ceriotti, J. Chem. Phys. **145**, 234103 (2016).

[102] N. Ananth and T. F. Miller III, J. Chem. Phys. **133**, 234103 (2010).

[103] N. Ananth, J. Chem. Phys. **139**, 124102 (2013).

[104] A. R. Menzeleev, F. Bell, and T. F. Miller III, J. Chem. Phys. **140**, 064103 (2014).

[105] J. O. Richardson, P. Meyer, M.-O. Pleinert, and M. Thoss, Chem. Phys. **482**, 124 (2017).

[106] T. E. Markland and D. E. Manolopoulos, J. Chem. Phys. **129**, 024105 (2008).

[107] T. E. Markland and D. E. Manolopoulos, Chem. Phys. Lett. **464**, 256 (2008).

[108] C. John, T. Spura, S. Habershon, and T. D. Kühne, Phys. Rev. E **93**, 043305 (2016).

[109] D. Frenkel and B. Smit, *Understanding Molecular Simulation* (Academic Press, 2002).

[110] M. E. Tuckerman, *Statistical Mechanics: Theory and Molecular Simulation* (Oxford University Press, 2010).

[111] J. Vaníček, W. H. Miller, J. F. Castillo, and F. J. Aoiz, J. Chem. Phys. **123**, 054108 (2005).

[112] J. Vaníček and W. H. Miller, J. Chem. Phys. **127**, 114309 (2007).

[113] T. Zimmermann and J. Vaníček, J. Chem. Phys. **131**, 024111 (2009).

[114] T. Zimmermann and J. Vaníček, J. Mol. Model. **16**, 1779 (2010).

[115] M. Buchowiecki and J. Vaníček, Chem. Phys. Lett. **588**, 11 (2013).

[116] O. Maršálek, P.-Y. Chen, R. Dupuis, M. Benoit, M. Méheut, Z. Bačić, and M. E. Tuckerman, J. Chem. Theory Comput. **10**, 1440 (2014).

[117] K. Karandashev and J. Vaníček, J. Chem. Phys. **143**, 194104 (2015).

[118] Z. Liu and B. J. Berne, J. Chem. Phys. **99**, 6071 (1993).

[119] X. Kong and C. L. Brooks III, J. Chem. Phys. **105**, 2414 (1996).

[120] Z. Guo, C. L. Brooks III, and X. Kong, J. Phys. Chem. B **102**, 2032 (1998).

[121] R. Bitetti-Putzer, W. Yang, and M. Karplus, Chem. Phys. Lett. **377**, 633 (2003).

[122] R. H. Swendsen and J.-S. Wang, Phys. Rev. Lett. **57**, 2607 (1986).

[123] K. Hukushima and K. Nemoto, J. Phys. Soc. Jpn. **65**, 1604 (1996).

[124] C. Predescu, M. Predescu, and C. V. Ciobanu, J. Phys. Chem. B **109**, 4189 (2005).

[125] T. Osawa, T. Futakuchi, T. Imahori, and I.-Y. S. Lee, J. Mol. Catal. A **320**, 68 (2010).

[126] J. S. J. Hargreaves, G. J. Hutchings, R. W. Joyner, and S. H. Taylor, Appl. Catal. A **227**, 191 (2002).

[127] T. Yamamoto, J. Chem. Phys. **123**, 104101 (2005).

[128] J. Kästner, J. Chem. Phys. **131**, 034109 (2009).

[129] J. Kästner, J. Chem. Phys. **136**, 234102 (2012).

[130] E. Darve and A. Pohorille, J. Chem. Phys. **115**, 9169 (2001).

[131] E. Darve, D. Rodrígues-Gómez, and A. Pohorille, J. Chem. Phys. **128**, 144120 (2008).

[132] J. Comer, J. C. Gumbart, J. Hénin, T. Lelièvre, A. Pohorille, and C. Chipot, J. Phys. Chem. B **119**, 1129 (2015).

[133] M. Mezei, J. Comput. Phys. **68**, 237 (1987).

[134] R. W. W. Hooft, B. P. van Eijck, and J. Kroon, J. Chem. Phys. **97**, 6690 (1992).

[135] C. Bartels and M. Karplus, J. Comput. Chem. **18**, 1450 (1997).

[136] C. Micheletti, A. Laio, and M. Parrinello, Phys. Rev. Lett. **92**, 170601 (2004).

[137] A. Laio, A. Rodriguez-Fortea, F. L. Gervasio, M. Ceccarelli, and M. Parrinello, J. Phys. Chem. B **109**, 6714 (2005).

[138] K. S. Schweizer, R. M. Stratt, D. Chandler, and P. G. Wolynes, J. Chem. Phys. **75**, 1347 (1981).

[139] H. Flyvbjerg and H. G. Petersen, J. Chem. Phys. **91**, 461 (1989).

[140] J. Cao and B. J. Berne, J. Chem. Phys. **99**, 2902 (1993).

[141] D. W. Schwenke and H. Partridge, Spectrochim. Acta A **57**, 887 (2001).

[142] R. J. Duchovic, Y. L. Volobuev, G. C. Lynch, A. W. Jasper, D. G. Truhlar, T. C. Allison, A. F. Wagner, B. C. Garrett, J. Espinosa-García, and J. C. Corchado, POTLIB, http://comp.chem.umn.edu/potlib.

[143] F. T. Smith, Phys. Rev. Lett. **45**, 1157 (1980).

[144] M. Sprik, M. L. Klein, and D. Chandler, Phys. Rev. B **31**, 4234 (1985).

[145] M. Sprik, M. L. Klein, and D. Chandler, Phys. Rev. B **32**, 545 (1985).

[146] K. Karandashev and J. Vaníček, submitted.

[147] W. L. Jorgensen and L. L. Thomas, J. Chem. Theory Comput. **4**, 869 (2008).

[148] B. Cheng, J. Behler, and M. Ceriotti, J. Phys. Chem. Lett. **7**, 2210 (2016).

[149] S. Chapman, B. C. Garrett, and W. H. Miller, J. Chem. Phys. **63**, 2710 (1975).

[150] M. Ceotto, Mol. Phys. **110**, 547 (2012).

[151] Y. Zhao, T. Yamamoto, and W. H. Miller, J. Chem. Phys. **120**, 3100 (2004).

[152] M. Ceotto and W. H. Miller, J. Chem. Phys. **120**, 6356 (2004).

[153] W. Wang, S. Feng, and Y. Zhao, J. Chem. Phys. **126**, 114307 (2007).

[154] W. Wang and Y. Zhao, J. Chem. Phys. **130**, 114708 (2009).

[155] W. Wang and Y. Zhao, Phys. Chem. Chem. Phys. **13**, 19362 (2011).

[156] W. Wang and Y. Zhao, J. Chem. Phys. **137**, 214306 (2012).

[157] H. Engel, R. Eitan, A. Azuri, and D. T. Major, Chem. Phys. **450-451**, 95 (2015).

[158] S. Yang, T. Yamamoto, and W. H. Miller, J. Chem. Phys. **124**, 084102 (2006).

[159] M. J. Kurylo, G. A. Hollinden, and R. B. Timmons, J. Chem. Phys. **52**, 1773 (1970).

[160] J. S. Shapiro and R. E. Weston, Jr., J. Phys. Chem. **76**, 1669 (1972).

[161] J. Kerr and J. Parsonage, *Evaluated kinetic data on gas phase hydrogen transfer reactions of methyl radicals* (Butterworths, 1976).

[162] W. Tsang and R. F. Hampson, J. Phys. Chem. Ref. Data **15**, 1087 (1986).

[163] G. C. Schatz, A. F. Wagner, and T. H. Dunning, Jr., J. Phys. Chem. **88**, 221 (1984).

[164] J. Pu and D. G. Truhlar, J. Chem. Phys. **117**, 10675 (2002).

[165] B. Kerkeni and D. C. Clary, J. Phys. Chem. A **108**, 8966 (2004).

[166] Y. Li, Y. V. Suleimanov, J. Li, W. H. Green, and H. Guo, J. Chem. Phys. **138**, 094307 (2013).

[167] M. E. Tuckerman, B. J. Berne, G. J. Martyna, and M. L. Klein, J. Chem. Phys. **99**, 2796 (1993).

[168] A. I. Boothroyd, W. J. Keogh, P. G. Martin, and M. R. Peterson, J. Chem. Phys. **104**, 7139 (1996).

[169] S. A. Chin and C. R. Chen, J. Chem. Phys. **117**, 1409 (2002).

[170] S. A. Chin, Phys. Rev. E **69**, 046118 (2004).

[171] M. Ceriotti, G. A. R. Brain, O. Riordan, and D. E. Manolopoulos, Proc. R. Soc. A **468**, 2 (2012).

[172] X. Huang, B. J. Braams, and J. M. Bowman, J. Chem. Phys. **122**, 044308 (2005).

[173] Z. Xie, B. J. Braams, and J. M. Bowman, J. Chem. Phys. **122**, 224307 (2005).

[174] B. J. Braams and J. M. Bowman, Int. Rev. Phys. Chem. **28**, 577 (2009).

[175] H. Eyring, J. Chem. Phys. **3**, 107 (1935).

[176] M. G. Evans and M. Polanyi, Trans. Faraday Soc. **31**, 875 (1935).

[177] B. H. Mahan, J. Chem. Educ. **51**, 709 (1974).

[178] D. G. Truhlar, D.-H. Lu, S. C. Tucker, X. G. Zhao, A. Gonzalez-Lafont, T. N. Truong, D. Maurice, Y.-P. Liu, and G. C. Lynch, "Variational transition-state theory with multidimensional, semiclassical, ground-state transmission coefficients," in *Isotope Effects in Gas-Phase Chemistry*, Chap. 2, pp. 16–36.

[179] J. Espinosa-García and J. C. Corchado, J. Phys. Chem. **100**, 16561 (1996).

[180] K. Karandashev, Z.-H. Xu, M. Meuwly, J. Vaníček, and J. O. Richardson, Structural Dynamics (2017), accepted.

[181] C. Aieta and M. Ceotto, J. Chem. Phys. **146**, 214115 (2017).

[182] D. Thirumalai and B. J. Berne, J. Chem. Phys. **79**, 5029 (1983).

[183] K. Yamashita and W. H. Miller, J. Chem. Phys. **82**, 5475 (1985).

[184] E. Rabani, G. Krilov, and B. J. Berne, J. Chem. Phys. **112**, 2605 (2000).

[185] E. Sim, G. Krilov, and B. J. Berne, J. Phys. Chem. A **105**, 2824 (2001).

[186] C. Predescu, Phys. Rev. E **70**, 066705 (2004).

[187] J. Costley and P. Pechukas, Chem. Phys. Lett. **83**, 139 (1981).

[188] C. Eckart, Phys. Rev. **35**, 1303 (1930).

[189] S. Jang and G. A. Voth, J. Chem. Phys. **112**, 8747 (2000).

[190] J. Richardson, private communication.

[191] R. D. Coalson, D. L. Freeman, and J. D. Doll, J. Chem. Phys. **85**, 4567 (1986).

[192] O. Ersoy, IEEE Trans. Acoust., Speech, Signal Process. **33**, 880 (1985).

[193] A. Azuri, H. Engel, D. Doron, and D. T. Major, J. Chem. Theory Comput. **7**, 1273 (2011).

[194] D. M. Ceperley, Rev. Mod. Phys. **67**, 279 (1995).

[195] D. T. Major and J. Gao, J. Mol. Graph. Model. **24**, 121 (2005).

Personal Details

Name	M. Konstantin Karandashev
Address	Avenue du Mottey 27 1020 Renens, Switzerland
Telephone	+41 79 371 50 48
E-mail	kvkarandashev@gmail.com
Nationality	Russian
Date of birth	15th of October 1990

Educational Qualifications

Ph.D. student in the Laboratory of Theoretical Physical Chemistry present
EPFL, Switzerland

Specialist degree in physical organic chemistry 2012
Moscow State University, Russia

Publications

Accelerating quantum instanton calculations of the kinetic isotope effects
K. Karandashev and J. Vaníček, J. Chem. Phys. **143**, 194104 (2015).

Accelerating equilibrium isotope effect calculations. I. Stochastic thermodynamic integration with respect to mass
K. Karandashev and J. Vaníček, J. Chem. Phys. **146**, 184102 (2017).

Kinetic isotope effects and how to describe them
K. Karandashev, Z.-H. Xu, M. Meuwly, J. Vaníček, J. O. Richardson
In press

Accelerating equilibrium isotope effect calculations: II. Stochastic implementation of direct estimators
K. Karandashev and J. Vaníček
Submitted

Oral Presentations

Accelerating Quantum Instanton Calculations of Kinetic Isotope Effects 2015
Fall Meeting of the Swiss Chemical Society, EPFL, Switzerland

Skills

Languages	Russian (mother tongue), English (C1), French (B2)
Softwares	LaTeX, Microsoft office
Programming languages	FORTRAN, BASH, C, PYTHON

Interests

SPORTS (aikido, jojutsu)

SPORT DANCING (acrobatic Rock'n'Roll, disco-fox, salsa)

TRAVELLING